

Preparation of Titanate nanosheets with  
High Photocatalytic Activities by Rh-Doping and  
Addition of Visible–Light Sensitivity

Wasusate Soontornchaiyakul

Interdisciplinary Graduate School of Science and Engineering

SHIMANE UNIVERSITY

# Contents

	Page
<b>Chapter 1 Introduction</b>	
1.1 Background of the research and motivation	1
1.2 Scope and Objectives	6
References	8
<b>Chapter 2 Literature reviews</b>	
2.1 Introduction	12
2.2 TiO <sub>2</sub> based material	15
2.2.1 Titanate nanosheets	16
2.2.2 Optical properties of titanate nanosheets	18
2.2.3 Cation exchange capacity of titanate nanosheets	19
2.3 Photocatalytic activity of titanate nanosheet	19
2.3.1 Photocatalytic degradation	21
2.3.2 Photocatalytic water splitting	24
2.4 Improvement of photocatalytic activity of titanate nanosheet	25
2.4.1 band gap theory and semiconductor	25
2.4.1 Metal doping and band-gap narrowing	28
2.5 Titanate nanosheet with photosensitizer dye	30
2.5.1 Dye-sensitized TiO <sub>2</sub>	32
2.5.2 Organic sensitizers	34

2.5.3 Inorganic dye sensitizers	35
2.6 Conclusion	35
References	36

### **Chapter 3 Synthesis of Rh doped Titanate Nanosheet and Investigation of Its Effect on Photocatalytic Activity for Organic Dye Degradation**

3.1 Introduction	52
3.2 Experimental	56
Reagents and materials	56
Synthesis of Rh-doped sodium titanate	57
Preparation of the nanosheet colloidal suspension	57
Adsorption properties of Ti <sub>3</sub> NS:Rh <sub>x</sub>	58
Photodegradation of organic methylene blue and methyl orange dye	59
Characterization and Photocurrent measurement	60
3.3 Results and discussion	62
Characterization of Rh doped titanate nanosheet	62
Optical and electrical properties of Ti <sub>3</sub> NS:Rh <sub>x</sub> and the effect of Rh	68
The energy band structure of Ti <sub>3</sub> NS:Rh <sub>x</sub>	71
Adsorption capacity for cationic methylene blue dye	75
Adsorption capacity for anionic methyl orange dye	78
Photodegradation of MB dye	79

Photodegradation of MO dye	82
Photocatalytic activity of Ti <sub>3</sub> NS:Rh <sub>x</sub>	85
3.4 Conclusions	87
References	88

## **Chapter 4 The photocatalytic Activity of Rh Doped Titanate Nanosheet for Hydrogen Evolution**

4.1 Introduction	94
4.2 Experimental Procedures	96
Materials	96
Preparation of the Rh-doped titanate nanosheets and Rh-load titanate nanosheets	96
H <sub>2</sub> evolution experiment	97
Characterization	97
4.3 Results and discussion	98
Preparation of Rh-loaded titanate nanosheets by photodeposition method and comparison with Rh-doped titanate nanosheets	98
Photocatalytic H <sub>2</sub> evolution by Ti <sub>3</sub> NS:Rh <sub>x</sub> under UV light and effect of Rh-doping and Rh loading	100
Photocatalytic H <sub>2</sub> evolution by Ti <sub>3</sub> NS:Rh <sub>x</sub> under visible light	108
4.4 Conclusion	108
References	110

## **Chapter 5 Dye-sensitized Rh-doped Titanate Nanosheets and its**

### **Photocatalytic H<sub>2</sub> Production under Visible Light**

5.1 Introduction	114
5.2 Experimental	118
Materials	118
Preparation of the dye-sensitized Rh-doped titanate nanosheets	118
H <sub>2</sub> evolution experiment	118
Characterization	119
5.3 Result and Discussion	120
Dye-sensitized Ti <sub>3</sub> NS:Rh <sub>x</sub> , its physical and optical properties	120
H <sub>2</sub> production by dye-sensitized Ti <sub>3</sub> NS:Rh <sub>x</sub> under visible light irradiation	127
5.4 Conclusion	133
References	134

## **Chapter 6 The controlled synthesis of Rh doped titanate nanosheets and the crystalline effect on adsorption activity**

6.1 Introduction	139
6.2 Experimental	141
Materials	141
Preparation of the Rh-doped potassium titanate	141
Preparation of the nanosheet colloidal suspension	142
Adsorption properties of Ti <sub>4</sub> NS:Rh <sub>x</sub>	142

Photodegradation of organic methylene blue dye	143
6.3 Result and Discussion	144
Synthesis of potassium titanate by PC method	144
The adsorption ability of Ti4NS:Rh <sub>x</sub>	151
The photocatalytic activity of Ti4NS:Rh <sub>x</sub> on the photodegradation of MB	153
6.4 Conclusion	156
References	157
<b>Chapter 7 Conclusion</b>	
7.1 Summary	161
7.2 Conclusion	165
References	167
<b>Academic Achievements</b>	169
<b>ACKNOWLEDGMENTS</b>	

# Chapter 1

## Introduction

### 1.1 Background of the research and motivation

Most of the energy resources we use in our daily lives come from fossil fuels such as petroleum, coal, gas and etc.<sup>1,2</sup> However, these fossil fuels are a limited resource which means that eventually it will disappear in the near future.<sup>3</sup> Moreover, fossil fuel can pollute water, atmosphere, and so on.<sup>4</sup> Due to this, new resources have to be found, in addition, it has to be enough to satisfy humans' daily uses and environmental friendly. Sunlight is one of the clean energies and friendly to both human and environment; it also an unlimited resource.<sup>5,6</sup> Accordingly, it caught an attention all over the world in which researchers have begun a research on development of photo-energy exchange system.

In these past decades, photo-energy exchange system has been researched and developed intensively in the form of photo-electric energy exchange such as solar cell or solar battery; photo-energy exchange in the form of chemical energy which is called artificial photosynthesis. Artificial photosynthesis is an interesting method as it imitates the actual photosynthesis which found in the plants.<sup>7-8</sup> Photocatalyst materials are important in order to turn sunlight energy to chemical energy. One of the well-known photocatalyst materials is TiO<sub>2</sub>.<sup>9-12</sup> TiO<sub>2</sub> shows properties of photocatalyst under UV light as reported by Honda and Fujishima in 1972.<sup>13</sup> Generally, TiO<sub>2</sub> is in the form of powder compacting to a big bead; this is called bulk molecule. Therefore, TiO<sub>2</sub> can only adsorb light on the surface, additionally, photocatalytic reaction can occur only at the surface of photocatalyst.<sup>14</sup> Big compacted molecule has low surface area. As a result, TiO<sub>2</sub> does not perform as a photocatalyst materials well. In order to solve this problem, one of the methods is to increase the surface area of TiO<sub>2</sub> by reducing the size of molecule or design the molecules to arrange in a sheet-like with the width of 1 TiO<sub>2</sub> molecule. One of the interesting structure of TiO<sub>2</sub> is nanosheet which is exfoliated from layered titanate compound.<sup>15-19</sup>

Titanate nanosheet is one of TiO<sub>2</sub> structure with the width of 1-2 nm but it has a surface area of μm<sup>2</sup>. Titanate nanosheet is from the exfoliation of layered titanate compound i.e. layered alkaline titanate A<sub>2</sub>Ti<sub>n</sub>O<sub>2n+1</sub> (A:Na, K, n≥3), or lepidocrocate-type titanate, Ti<sub>2-n/4</sub>□<sub>n/4</sub>O<sub>4</sub> (n ~ 0.7; □, vacancy).<sup>21,22</sup> Titanate nanosheets has more specific surface area for photocatalytic reaction compared to bulk molecule due to the width of the sheet is less than the surface area. Theoretically, titanate nanosheets will show higher photocatalyst ability compared to Bulk molecules of TiO<sub>2</sub>. However, titanate nanosheets have one problem which is light response since the structure of

molecule is a sheet-like characteristic and thin causing the energy structure of titanate nanosheets changed from the bulk molecule. The differences are titanate nanosheets have an energy band gap wider than TiO<sub>2</sub> bulk molecule causing it to respond only UV light ( $\lambda \leq 300$ ). Although, sunlight contains UV light but titanate nanosheets cannot exchange energy from the sunlight. Consequently, the energy band gap of titanate nanosheet has to be reduced or modified its energy structure to yield titanate nanosheet that respond to sunlight especially visible light which is contained in sunlight more than 40%.

There are two methods to improve titanate nanosheets' performance which are the adjustment of energy band structure of titanate nanosheets by metal doping, and the use of titanate nanosheets as building blocks of dye-sensitized photocatalyst or hybridization between titanate nanosheets and photosensitizer organic dyes. Metal doping is a method where atom of transition metal replacing atom of Ti in the titanate nanosheet without affecting the structure of titanate nanosheet. With this method, energy band structure will alter as energy band structure is directly corresponded with the atom in the structure yielding new energy level of transition metal which dope to replace Ti. In recent years, there are several researches proving that metal doping causes the photocatalyst material to respond with light in the visible light region. Kudo et. al. reported that Rh doping in SrTiO<sub>3</sub> enhances the ability to absorb light at the long wavelength ( $\lambda \geq 420\text{nm}$ ) and photocatalytic reaction also occurs at  $\lambda \geq 420 \text{ nm}$ .<sup>xx</sup> Meanwhile, Ida et al. also reported about the property of Rh which enhanced the photocatalyst of lepidrocrocite-type titanate. From these researches, we saw an opportunity to improve the photocatalyst property of titanate nanosheet which

exfoliated from layered titanate for example, sodium titanate ( $\text{Na}_2\text{Ti}_3\text{O}_7$ ) and potassium titanate ( $\text{K}_2\text{Ti}_4\text{O}_9$ ).

On the contrary, photosensitizer dye-sensitizer is used to alter titanate nanosheet to respond to visible light. The mechanism is that the photosensitizer dye function is to adsorb light in the visible region and generate electron donating to titanate nanosheets for the chemical reaction. In order for this system to work out, LUMO level of photosensitizer dye has to have higher value of conduction band level of titanate nanosheets so that electron from LUMO can move to the conduction band.<sup>23-25</sup> For example, Sasai *et al.* described the photoactivity of  $\text{TiO}_2$  nanoparticle and copper (II) phthalocyanine in interlayer spacing of clay material.<sup>26</sup> When  $\text{TiO}_2$  nanoparticles were irradiated under visible light and could degrade organic molecules. According to all of these researches, they suggested the ability to give electron between photosensitizer dye and titanate material and photocatalyst ability under visible light. Thus, hybridization between titanate nanosheet and photosensitizer dye is a method with high possibility for increasing the capability of titanate nanosheet for being photocatalyst under visible light.

In our research, we aim to develop and enhance the capability of titanate nanosheets as a photocatalyst which was exfoliated from layered sodium titanate and layered potassium titanate by metal doping. In addition, we used titanate nanosheet as building blocks for dye sensitized photocatalyst with porphyrins dye and/or Ir complex derivative such as Ir (III) 2-pyridyn, 2, 2'-bipyridyn.<sup>27-30</sup> We studied the properties of photocatalyst of titanate nanosheet and dye sensitized titanate nanosheets under visible light via photo-degradation of organic molecule and/or photo-induce hydrogen production from water splitting

## 1.2 Scope and Objectives

The main purpose of this study was to improve the photocatalytic activity of titanate nanosheets for organic molecule decomposition and/or H<sub>2</sub> production under the visible light by using metal doping such as Rhodium doping, and the hybridization with organic photosensitizer dye and/or metal ligand complex.

To achieve these aims, the specific objectives of this thesis were as follow;

- 1 Understand the formation of titanate nanosheets, and metal doping on their crystals structure.
- 2 Optimize the doping amount, investigate the electrical and optical properties of metal doped titanate nanosheets, and realize the effect of metal doping
- 3 Investigate the photocatalytic activity of metal doped titanate for organic dye decomposition and H<sub>2</sub> production under UV light and visible light.
- 4 Understand the hybridization between titanate nanosheets and organic photosyntizer dye and/or metal complex, observe the photoactivity between organic and inorganic part, and investigate the photocatalytic activity under visible light.

The current study presents the synthesis of metal doped titanate nanosheets in various structures and the photocatalytic activity across six chapters. An overview of each chapter is descried as follow;

Chapter 2: This chapter shows the background relating to currently work with including the basic principle of photocatalysis, the related literature on titanate based material and also the formation of titanate nanosheet as well as the recently literature on the effect of metal doping on photocatalytic activity of metal oxide material.

Chapter 3: This chapter includes the synthesis of metal doping titanate nanosheet which based on the structure of layered sodium titanium oxide. The effect of metal doping on the optical properties of titanate nanosheet and the photocatalytic activity on organic dye decomposition.

Chapter 4: This chapter shows the photocatalytic hydrogen production by metal doping titanate nanosheets, and a comparison between metal doping and cocatalyst loading. It also includes the photocatalytic activity of metal doping titanate nanosheets under visible light.

Chapter 5: In this chapter, it shows hybridized between metal doping titanate nanosheet and organic photosensitizer organic dye and/or inorganic metal complex dye aimed to improve the photoabsorption for visible light region.

Chapter 6: This chapter continues the findings of the results in previous chapter. The basic structure of titanate nanosheet was changed to investigate the effect of metal doping on another basic structure which different to it in chapter 3.

Chapter 7: this chapter concludes the present study, and recommends a possible future work.

## References

1. Aleklett, K., Höök, M., Jakobsson, K., Lardelli, M., Snowden, S., & Söderbergh, B. (2010). The Peak of the Oil Age – Analyzing the world oil production Reference Scenario in World Energy Outlook 2008. *Energy Policy*, 38(3), 1398-1414.
2. Bentley, R. (2002). Global oil & gas depletion: an overview. *Energy Policy*, 30(3), 189-205.
3. Ellabban, O., Abu-Rub, H., & Blaabjerg, F. (2014). Renewable energy resources: Current status, future prospects and their enabling technology. *Renewable and Sustainable Energy Rev.*, 39, 748-764.
4. Jacobson, M. Z. (2004). Climate response of fossil fuel and biofuel soot, accounting for soots feedback to snow and sea ice albedo and emissivity. *J. Geophys. Res.: Atmos.*, 109(D21).
5. Mortimer, N. (1993). Energy Analysis of Renewable Energy Sources. *Energy Policy*, 123-134.
6. Kannan, N., & Vakeesan, D. (2016). Solar energy for future world: - A review. *Renewable and Sustainable Energy Rev.*, 62, 1092-1105.
7. Balat, M. (2008). Potential importance of hydrogen as a future solution to environmental and transportation problems. *Int. J. Hydrogen Energy*, 33, 4013-4029.
8. ODaly, A. (2002). Encyclopedia of life sciences. New York: Marshall Cavendish Corp.
9. J Schneider, J., Matsuoka, M., Takeuchi, M., Zhang, J., Horiuchi, Y., Anpo, M., & Bahnemann, D. W. (2014). Understanding TiO<sub>2</sub> Photocatalysis: Mechanisms and Materials. *Chem. Rev.*, 114(19), 9919-9986.
10. Rahimi, N., Pax, R. A., & Gray, E. M. (2016). Review of functional titanium oxides. I: TiO<sub>2</sub> and its modifications. *Prog. Solid State Chem.*, 44(3), 86-105.
11. Yuan, S., Sheng, Q., Zhang, J., Yamashita, H., & He, D. (2008). Synthesis of thermally stable mesoporous TiO<sub>2</sub> and investigation of its photocatalytic

- activity. *Microporous Mesoporous Mater.*, 110(2-3), 501-507.
12. Fujishima, A., Zhang, X. & Tryk, D. A. (2008). TiO<sub>2</sub> photocatalysis and related surface phenomena. *Surf. Sci. Rep.*, 63, 515-582.
  13. Fujishima, A. & Honda, K. (1972). Electrochemical photolysis of water at a semiconductor electrode. *Nature*, 238, 37-38.
  14. Hagfeld, A. & Grätzel, M. (1995). Light-induced redox reactions in nanocrystalline systems. *Chem. Rev.*, 95, 49-68.
  15. Kordás, K., Mohl, M., Kónya, Z., & Kukovecz, Á. (2015). Layered titanate nanostructures: perspectives for industrial exploitation. *Transl. Mater. Res.*, 2(1), 015003.
  16. Huang, Y., Wang, J., Miao, L., Jin, Y., Peng, J., Li, Q., Fang, C., Han, J., Huang, Y. (2017). A new layered titanate Na<sub>2</sub>Li<sub>2</sub>Ti<sub>5</sub>O<sub>12</sub> as a high-performance intercalation anode for sodium-ion batteries. *J. Mater. Chem. A*, 5(42), 22208-22215.
  17. Saito, K., Kozeni, M., Sohmiya, M., Komaguchi, K., Ogawa, M., Sugahara, Y., & Ide, Y. (2016). Unprecedentedly enhanced solar photocatalytic activity of a layered titanate simply integrated with TiO<sub>2</sub>nanoparticles. *Phys. Chem. Chem. Phys.*, 18(45), 30920-30925.
  18. Choy, J., Lee, H., Jung, H., & Hwang, S. (2001). A novel synthetic route to TiO<sub>2</sub>-pillared layered titanate with enhanced photocatalytic activity. *J. Mater. Chem.*, 11(9), 2232-2234.
  19. Milanovic, M., Stijepovic, I., & Nikolic, L. (2010). Preparation and photocatalytic activity of the layered titanates. *Process. Appl. Ceram.*, 4(2), 69-73.
  20. Allen, M. R., Thibert, A., Sabio, E. M., Browning, N. D., Larsen, D. S., & Osterloh, F. E. (2010). Evolution of Physical and Photocatalytic Properties in the Layered Titanates A<sub>2</sub>Ti<sub>4</sub>O<sub>9</sub>(A = K, H) and in Nanosheets Derived by Chemical Exfoliation. *Chem. Mater.*, 22(3), 1220-1228.
  21. Kikkawa, S., Yasuda, F., & Koizumi, M. (1985). Ionic conductivities of Na<sub>2</sub>Ti<sub>3</sub>O<sub>7</sub>, K<sub>2</sub>Ti<sub>4</sub>O<sub>9</sub> and their related materials. *Mater. Res. Bull.*, 20(10), 1221-1227.
  22. Maluangnont, T., Arsa, P., Limsakul, K., Juntarachairot, S., Sangsan, S.,

- Gotoh, K., & Sooknoi, T. (2016). Surface and interlayer base-characters in lepidocrocite titanate: The adsorption and intercalation of fatty acid. *J. Solid State Chem.*, 238, 175-181.
23. Matsuoka, M., Ide, Y., & Ogawa, M. (2014). Temperature-dependent photocatalytic hydrogen evolution activity from water on a dye-sensitized layered titanate. *Phys. Chem. Chem. Phys.*, 16(8), 3520.
24. Chu, L., Qin, Z., Yang, J., & Li, X. (2015). Anatase TiO<sub>2</sub> Nanoparticles with Exposed {001} Facets for Efficient Dye-Sensitized Solar Cells. *Sci. Rep.*, 5(1).
25. Pastore, M., Etienne, T., & Angelis, F. D. (2016). Structural and electronic properties of dye-sensitized TiO<sub>2</sub> for solar cell applications: from single molecules to self-assembled monolayers. *J. Mater. Chem. C.*, 4(20), 4346-4373.
26. Yamada, T., Sasai, R., Itoh, H. (2007). Preparation and Characterization of Cu-Phthalocyanine/Titania/Organoclay Hybrid Adsorbed Materials with Photocatalytic ability. *Proceedings of International symposium on EcoTopia Science 2007*. ISETS07, 767-771.

# Chapter 2

## Literature reviews

### 2.1 Introduction

Photocatalyst is thought to be a promising material after the discovery of Fujishima and Honda in 1972. Photocatalyst is a catalyst which reacts under light irradiation. The basic material of photocatalyst is semiconductor. Photocatalyst is specifically used to treat organic and inorganic pollutants such as methylene blue; and cyanide.<sup>1-3</sup> Moreover, it can be used in the H<sub>2</sub> and O<sub>2</sub> production from water splitting reaction.<sup>4-6</sup> Fujishima and Honda reported that the efficacy of rutile TiO<sub>2</sub> in water splitting reaction in which Pt electrode generates H<sub>2</sub> while rutile TiO<sub>2</sub> acts as oxidize water molecule.<sup>5</sup> Even though, the discovery was found in decades ago, currently, TiO<sub>2</sub> and TiO<sub>6</sub> based material is still a main material for photocatalyst research field because of its low cost, high photocatalytic activity, and good stability against photo-corrosion.

Powdered TiO<sub>2</sub> can photocatalytic generate H<sub>2</sub> from deposited Pt on the surface of TiO<sub>2</sub>, nevertheless, its efficacy as a catalyst is lower than what suggested in the theory.<sup>7-</sup>

<sup>10</sup> This is due to the recombination of photogenerated  $\text{OH}^-$  and  $\text{H}^+$  which make photoexcited life-time of  $\text{TiO}_2$  to be short. Furthermore, water splitting reaction to produce  $\text{H}_2$  and  $\text{O}_2$  requires both  $e^-$  and  $h^+$  at the same time, as a result, the rate of reaction is tremendously low. To increase life time of photogenerated  $e^-$  and  $h^+$ , it is a necessity to improve a material for using as a photocatalyst. In recent years, nano-scale material has been researched extensively and the definition of nano-scale material is a material with the size lower than 100 nm. For example, if the material has length, width, and height in a nanometer, it is called “nanoparticle”. However, if the length is greater than 1 micrometer, it is called “nanotube”. While “nanosheets” has a height about  $<100\text{nm}$ , and its width and length are in micro-scale as shown in figure 2.1.<sup>11-15</sup> Nevertheless, nanoscale exhibits different properties from the bulk molecule besides being smaller in size. Hence, it can be used as a building block for developing new material and devices.

Layered-titrate material was reported that it can be exfoliated and form a nano-scale sheet-liked crystal. Even with the nanosheet crystal, the titrate nanosheet also acts as a photocatalyst. The life time of photogenerated  $e^-$  and  $h^+$  is longer than bulk or powdered material due to nanosheet crystal is thinner than its surface area. Many research showed that the system of titrate nanosheet with cocatalyst deposited has a higher efficiency in the case of powdered  $\text{TiO}_2$  compared to nanosheet. Nonetheless, powdered  $\text{TiO}_2$  or titrate nanosheet are not photocatalytic active under visible light ( $>420\text{ nm}$ ) because of the large energy band gap.<sup>16-20</sup>

Nanoparticle

Nanotube

Nanosheet

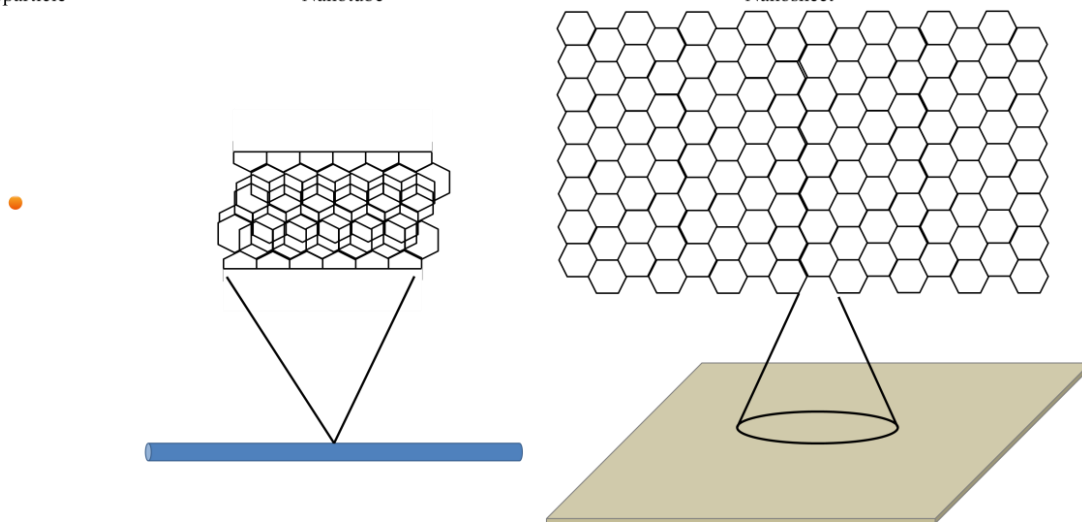


Figure 2.1 The schematic of nanostructure material.

TiO<sub>2</sub> based material needs to be improved in order to work under visible light. Kudo *et. al.* presented the use of metal doping for tuning energy band gap of titanate compound.<sup>21-29</sup> The results showed that it can absorb visible light and generate H<sub>2</sub> from water. Metal doping seems to be one of the ways to promote titanate nanosheet to be able to absorb visible light and acts as a photocatalyst under visible light. Another methods to improve titanate nanosheet or TiO<sub>2</sub> based materials are hybridization with a photosensitizer.<sup>30-32</sup> In past few years, many research reported the hybrid system of metal oxide semiconductor and photosensitizer such as porphyrin dyes or metal ligand complex. The results exhibit the possibility to obtain the photocatalytic H<sub>2</sub> evolution under visible light from these hybrid materials. However, to obtain a good hybrid system for specific photocatalytic activity is still required. Thus, the development of titanate nanosheet including other metal oxide nanosheet has been studied for its use as a photocatalyst under visible light until now.

This chapter reviews about photocatalytic reactions including photo degradation and photo induce water splitting along with the development of photocatalyst especially titanate based material

## **2.2 TiO<sub>2</sub> based material**

TiO<sub>2</sub> has been used in research (i.e. photocatalyst), and industry since it is a low-cost material with chemical stability, and non-toxicity.<sup>33-35</sup> TiO<sub>2</sub> based material has various structures; TiO<sub>2</sub> has three main structures which are anatase, rutile or brookite, and titanate or titanium oxide (similar substance in the same group as TiO<sub>2</sub>). The main structures of TiO<sub>2</sub> based material derives from the arrangement and distortion of TO<sub>6</sub> octahedral which Ti<sup>4+</sup> surrounds by six of O<sup>2-</sup> ions.<sup>36-39</sup>

Titanate can be classified into many structures includes perovskite type, and layered structure such as  $A_2Ti_nO_{2n+1}$ , and  $A_nTi_{2-x/4}[\ ]_{x/4}O_4$  where  $[\ ]$  is a vacancies. Layered titanate has crystal structure made from a layer of  $TiO_6$  octahedral with share edge arranged with infinite two dimensions, and layer of cation alternately (figure 2.2).

Perovskite structure is shown in general formula as  $ABO_3$ . In case of  $TiO_2$  based perovskite, the general formula becomes  $ATiO_3$  which A is occupied by large cation ex. Sr, Ba, Pb, etc. The perovskite structure occurs from the arrangement of  $TiO_6$  octahedral by sharing edge. As for A ion, it is surrounded by twelve of oxygen atoms at the center of eight of  $TiO_6$  octahedrals form cubic lattice (figure 2.3).

$TiO_2$  based material shows a property of being n-type semiconductor with electrons as majority carriers, and holes as minority carriers. Fermi level, an energy band gap where 50% of electrons occupies, inclines to conduction band because numbers of electron is more than the holes resulted in  $TiO_2$  based material show a property of n-type semiconductor

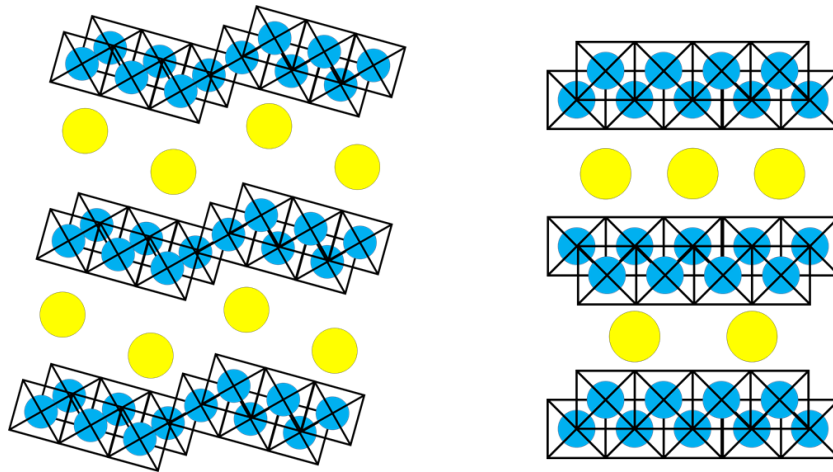


Figure 2.2 The crystal structure of layered titanate compound  $A_2Ti_3O_7$  (left), and  $A_nTi_{2-x/4}[\ ]_{x/4}O_4$  (right)

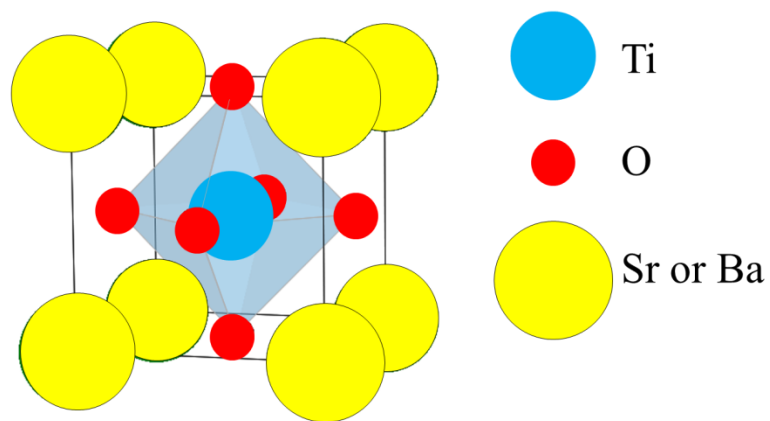


Figure 2.3 The unit cell of Perovskite structured titanate.

### 2.2.1 Titanate nanosheets<sup>40-44</sup>

Titanate nanosheet is a  $\text{TiO}_2$  based material with a sheet-like crystal structure and its width is about 0.7-1.5nm. Titanate nanosheet can be prepared from layered titanate compound. Layered titanate has an ability of cation exchange due to layered titanate has a structure without  $\text{TiO}_6$  octahedral, and layer of cation. The attraction force between cation layer and  $\text{TiO}_6$  octahedral layer is mainly electrostatic force, and the distance between  $\text{TiO}_6$  octahedral layer to layer is fixed by cation and electrostatic interaction between them. With these properties, the structure can be controlled from the alteration of cation by cation exchange reaction. Generally, cation is alkaline metals ex.  $\text{Na}^+$ ,  $\text{K}^+$ ,  $\text{Cs}^+$ . The cation exchange can be done using alkaline metal for  $\text{H}^+$  by reacting with acid such as  $\text{HCl}$  or  $\text{HNO}_3$ . In order to change cation layer to  $\text{H}^+$ , it will cause the distance between  $\text{TiO}_6$  octahedral layer to layer or interlayer distance to be wider. Moreover, the cation layer is more acidic which makes the layered titanate can exchange cation with high basicity compound better i.e. amine, or ammonium ion. The cation exchange of  $\text{H}^+$  (amine or ammonium ion) causes interlayer distance to be longer, and the structure becomes unstable as the electrostatic interaction decreases as the distance increases. As a result, when layered titanate is dispersed in solution such water; amine or ammonium ion will react with water molecule causing interlayer distance to grow wider, and layered titanate will gradually peel off as a sheet (Figure 2.4). The layered titanate turns to titanate nanosheets in colloidal suspension; this method is called liquid exfoliation.

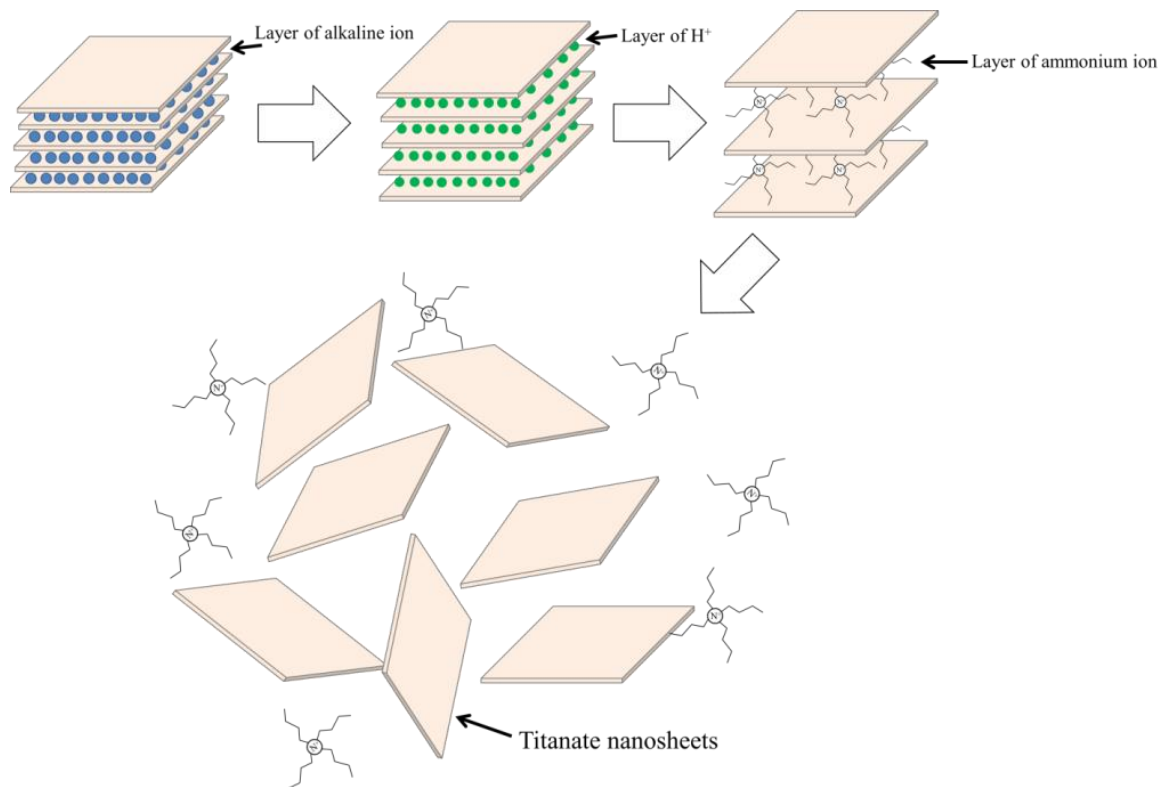


Figure 2.4 The schematic diagram of liquid exfoliation process.

### 2.2.2 Optical properties of titanate nanosheets<sup>45-50</sup>

Photocatalytic property is one of the important variables that specifies a photocatalyst. Titanate nanosheet is a material with a structure of layered titanate and composed of the arrangement of  $\text{TiO}_6$  octahedral similar to  $\text{TiO}_2$ . Hence, titanate nanosheets is also a semiconductor, however, the dimension of titanate nanosheet is different from layered titanate, and  $\text{TiO}_2$  as bulked powder compound resulting in quantum size effect on electronic band structure of titanate nanosheet. According to Pauli's exclusion principle, more than one electron cannot stay in the same energy level. Therefore, when two atoms are in the same energy level, the interaction between two atoms will disperse energy level causing electron to stay in the new energy level. In case of crystalline material, there are many atoms which closely deposits causing the energy level to divide from discrete energy level to continuous manner. This results in energy band which classifies to valence band, and conduction band as previously stated.

Titanate nanosheet is a bulk molecule of layered titanate; it has molecules arranged in three dimensions. After it turns into sheets-liked structure; the molecules only arrange in horizontal plane, consequently, many energy bands from discrete energy level considerably decreases and the energy level of energy band is lessened. This implies that valance band and conduction band becomes wider or energy gap of titanate nanosheets is higher in the form of bulk molecule structure. The energy band gap of titanate nanosheets as a semiconductor can be derived from the adsorption edge ( $\lambda_g$ ). In UV-vis spectra data, the correlation between  $\lambda_g$  and  $E_g$  can be expressed in the following equation:

$$E_g = (hc)/\lambda_g \approx 1240/\lambda_g$$

, where  $h$  is a Planck constant, and  $c$  is a speed of light in vacuum.

### 2.2.3 Cation exchange capacity of titanate nanosheets<sup>51-53</sup>

Former structure of titanate nanosheets is a layer of  $\text{TiO}_6$  octahedral alternated with cation. The electrostatic interaction between these two are attached to each other even after the exfoliation. The surface of titanate nanosheets still retains the anionic charge; hence, the titanate nanosheets can adsorb or exchange cation through electrostatic interaction.

In general, cation exchange capacity (CEC) is defined from the amount of cations being retained on the surface area of soil particles in which CEC is calculated from the amount of positive charge ion exchange to the mass of soil. The unit is represented as meq/100g. CEC can be compared to the moles of cation to mass of soil; for example, CEC is equal to +1 cation = 10meq/100g and the value will be 5 meq/100 when cation is +2

The anionic charge of titanate nanosheets depends on its former structure or layered titanate such as lepidrocite;  $\text{A}_n\text{Ti}_{2-x/4}[\ ]_{x/4}\text{O}_4$  where  $[\ ]$  is a vacancies, has anionic charge as  $x$ , and alkaline titanate  $\text{A}_2\text{Ti}_n\text{O}_{2n+1}$  will have anionic charge equal to  $-2$  and it does not vary depending on  $n$  vale. This indicates that  $\text{TiNO}_{2n+1}$  can exchange cation at maximum when the amount is equal to anionic charge or +1 cation such as  $\text{Na}^+$  or  $\text{K}^+$  an exchange ion at maximum when 2 mol of  $\text{Na}^+$  or  $\text{K}^+$  to 1 mol of  $[\text{Ti}_n\text{O}_{2n+1}]$ .

## 2.3 Photocatalytic activity of titanate nanosheet

The light reflects at the surface of titanate nanosheet and light has more energy or equal to the energy band gap of titanate nanosheets. Electron in the valence band will be excited and moved to conduction band resulted in hole in the valence band.<sup>54-56</sup> To put it

simple, electron is anion and hole is a cation; they stay together at the beginning and no charge. However, when light reflects on electron gets the energy and separates from the cation; this is called charge separation. When electron is at the conduction band which causes by anti-bonding molecular orbits, electron can move a little through the structure. Nevertheless, photo-induced electron can be caught by positive charge or photo-induced  $h^+$  and release energy and their status degrades; this is called a recombination of hole-electron.

If photo-induced electron is not caught by the hole and move to the surface of photocatalyst; electron can be trapped by the molecule or radical at the surface of photocatalyst and redox reaction will occur. Similarly, if the molecule or radical of other compound attaches to the surface of photocatalyst where many photo-induced  $h^+$  deposits; this can cause redox reaction. Electron can reduce the electron acceptor while hole can oxidize the electron donor as shown in figure 2.5. If the recombination does not occur, and the photo-induced  $e^-/h^+$  can move to the surface of photocatalyst, it will result in redox reaction. This is called photocatalytic reaction.<sup>57-68</sup>

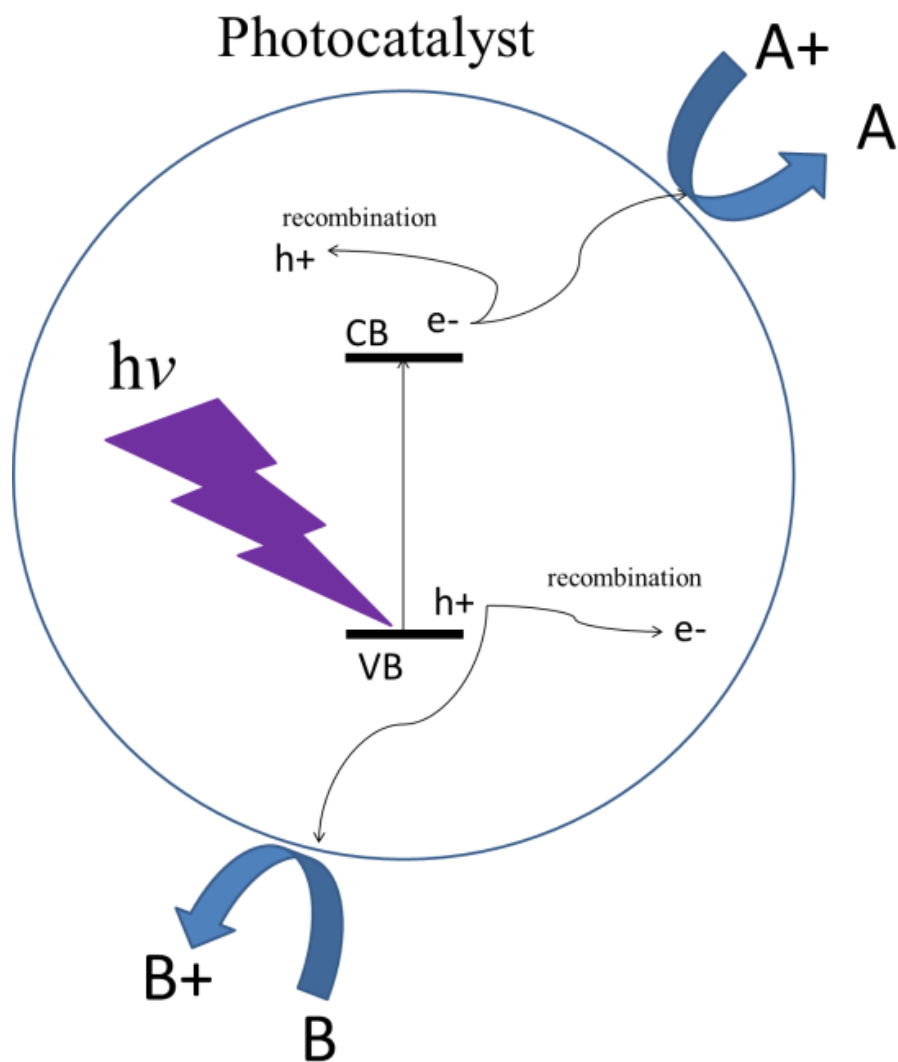


Figure 2.5 Photocatalytic reaction and the charge recombination occurred in the photocatalyst molecule under light irradiation

Photocatalytic reaction can be specified in two categories same as the general chemical reaction such as 'down-hill' reaction or exothermic reaction and 'up-hill' reaction or endothermic reaction. The "down-hill" or exothermic reaction is a case in which the Gibbs free energy has a negative value or releasing out energy related to the photocatalytic degradation (figure 2.6) While 'up-hill' reaction or endothermic reaction has a positive Gibbs free energy which relates to the light energy turning to chemical energy. This denotes that photocatalytic degradation is a favorable reaction due to that the product of reaction will be in more stable state than an initial compound. On the other hand, overall water splitting reaction to generate H<sub>2</sub> and O<sub>2</sub> is a "up-hill" reaction which requires a lot of electrons and light energy.<sup>69-72</sup> Thus, photocatalytic degradation or "down-hill" reaction is a simple process to check the photocatalytic responsibility of material. However, the final goal of photocatalyst is to apply them in the "up-hill" reaction such as overall water splitting, or CO<sub>2</sub> reduction.

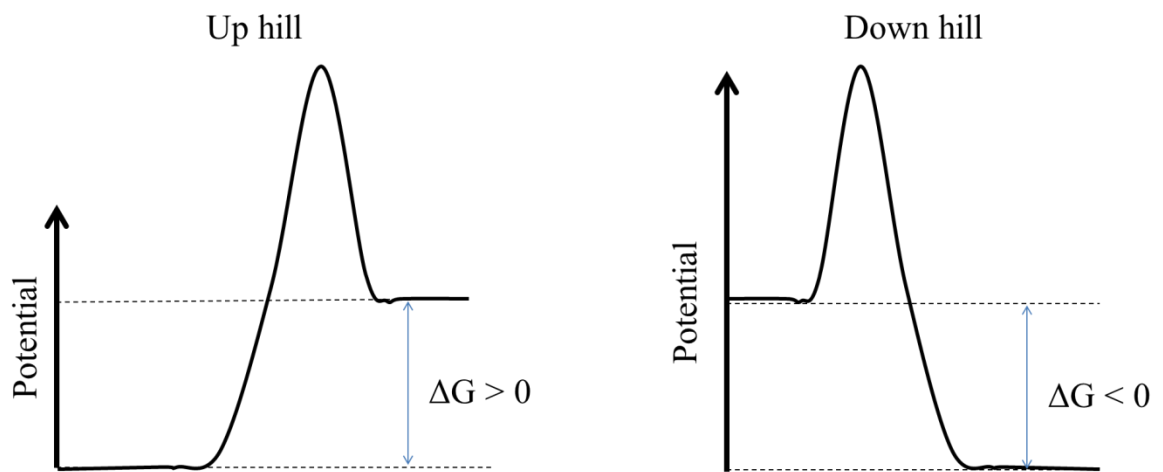


Figure 2.6 Photocatalytic reaction classified in two categories; 'down-hill' reaction or exothermic reaction and 'up-hill' reaction or endothermic reaction.

### 2.3.1 Photocatalytic degradation<sup>73-80</sup>

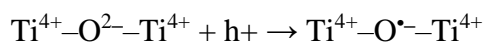
Photodegradation occurs from the organic matter which the light reflects on and cause the organic matter to be excited and lose electrons or catch by the holes. Eventually, the chemical structure will change and lose the former properties or reduces in size. Photodegradation can occur by the degradation of organic matter under light. Another way is from photocatalyst where organic matter adsorbed by surface of photocatalyst material, organic matter can be oxidized by photo generated hole or hole oxidizing hydroxyl group to produce hydroxyl radicals. The hydroxyl radical is highly active and oxidation potential is high enough to oxidize organic matter. Correspondingly, oxygen molecule can be reduced by photo-generated electron at the surface of photocatalyst material causing superoxide radical ( $O_2^-$ ). Hydroxyl radical does not require to be formed from only the hole trapping at the surface of photocatalyst; another way is superoxide radical. The overall mechanism of photocatalytic degradation of organic matter upon photocatalyst is  $TiO_2$  based material can be summarized as described below

Electron – hole generation in  $TiO_6$  octahedral

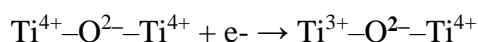


(a)

Charge carrier trapping in  $TiO_6$  octahedral

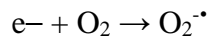


(b)



(c)

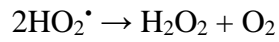
Electron transfer (reduction reaction)



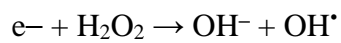
(d)



(e)

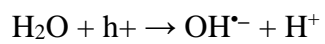


(f)



(g)

Hole trapping by water or organic molecule on surface of TiO<sub>2</sub> based materials



(h)

Rads + h<sup>+</sup> → R<sup>+</sup>ads where Rads is refer to organic molecule adsorbed on surface

(i)

Organic molecule degradation (by holes oxidation reaction)

h<sup>+</sup> + Rads → R<sup>+</sup>ads where Rads is refer to organic molecule adsorbed on surface

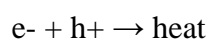
(j)

Organic molecule degradation (by OH radical)

R + OH<sup>•-</sup> → R<sup>+</sup> + H<sub>2</sub>O where R is an organic molecule

(k)

Charge recombination



(l)

Organic pollutants has a structure mainly composed of C, H, and O which can be decomposed to CO<sub>2</sub> and H<sub>2</sub>O. If the molecules compose of N, S, P atoms, it can form a compound of nitrate, sulphate, and phosphate, respectively. As previously described, the degradation of organic pollutants can occur directly from photo-generated hole or hydroxyl radical. The difference is that the photo degradation by holes requires the organic matter to be adsorbed by photocatalyst material. In contrary, hydroxyl radical does not require organic matter to be adsorbed at all.

### *2.3.2 Photocatalytic water splitting<sup>81-90</sup>*

H<sub>2</sub> has become one of the promising energy to replace the usage of fuel oil. In the near future, the production of high purity H<sub>2</sub> can be produced by electrochemical cell in the process of water splitting to yield H<sub>2</sub> and O<sub>2</sub>. Currently, many research shows that light can be used as the energy to initiate the electrochemical cell. Photocatalyst is an important factor in producing H<sub>2</sub> from water splitting reaction using light energy. Photocatalyst is used in water splitting reaction by the photo-induced e<sup>-</sup>/h<sup>+</sup> pairs. The light is being adsorbed by the photocatalyst yielding photo-generated e<sup>-</sup> in conduction band and h<sup>+</sup> in valence band; when water molecules adsorbed by the surface of photocatalyst, the water molecule will be oxidized by h<sup>+</sup> producing O<sub>2</sub>. Meanwhile, H<sup>+</sup> is reduced by e<sup>-</sup> to generate H<sub>2</sub>. Nevertheless, water splitting reaction requires a photocatalyst, conduction band level higher than reduction potential of H<sup>+</sup>/H<sub>2</sub>, and valence band lower than oxidation potential of O<sub>2</sub>/H<sub>2</sub>O for the reaction.

Theoretically, water splitting can occur at the surface of photocatalyst and yield H<sub>2</sub> and O<sub>2</sub>. In reality, this phenomenon is rarely occurred due to various reasons i.e. e<sup>-</sup>/h<sup>+</sup> recombination or the combination of H<sub>2</sub> and O<sub>2</sub> reverses back to water. Practically,

electron donors or electron acceptors is used as a sacrificial reagents in photocatalytic water splitting reaction to aid in the reaction. The role of sacrificial reagent will yield a product from water splitting as either H<sub>2</sub> or O<sub>2</sub>. As a result, reverse reaction of H<sub>2</sub> and O<sub>2</sub> to H<sub>2</sub>O is inhibited. The use of sacrificial reagent as electron donor (ex. Alcohol, tetraethylenimine) will gain H<sub>2</sub> production and electron donor being oxidized by hole replacing water molecules. In contrast, the sacrificial reagent is an electron acceptor then the only O<sub>2</sub> production will occur and the electron in conduction band will be consumed by electron acceptor instead.

In order to maximize photocatalytic water splitting under sunlight, this issue has been researched extensively until present. Photocatalyst is a semiconductor which is suitable for photocatalytic water splitting. Energy band gap is excessively wider than the visible light can excite photo-induced e<sup>-</sup>/h<sup>+</sup>. Moreover, visible light is mostly found in the sunlight, hence, most photocatalyst semiconductor cannot be used under sunlight including TiO<sub>2</sub> and titanate. The development of TiO<sub>2</sub> especially titanate nanosheet with wide band gap can be used as a photocatalyst for water splitting under sunlight is fascinating. Therefore, it has been continuously researched by the researchers.

## **2.4 Improvement of photocatalytic activity of titanate nanosheet**

### *2.4.1 band gap theory and semiconductor<sup>91-95</sup>*

In this topic, energy band gap will be discussed in detail for better understanding and development of titanate nanosheet to has optimum energy band gap as visible light energy. In single atom or isolated atom, electron in atomic orbits will have a separated energy level. However, when isolated atoms have more than 2 electrons near each other; it will form a molecule causing energy level to overlap. According to Puali exclusion

principle, two electrons cannot be in the same energy level but it has the same quantum number. Hence, two atoms will combine as diatomic molecule and overlapped energy level will separate to two energy levels (Figure 2.8). The more number of atoms bond the more overlapped energy level will almost disperse into a continuous band.

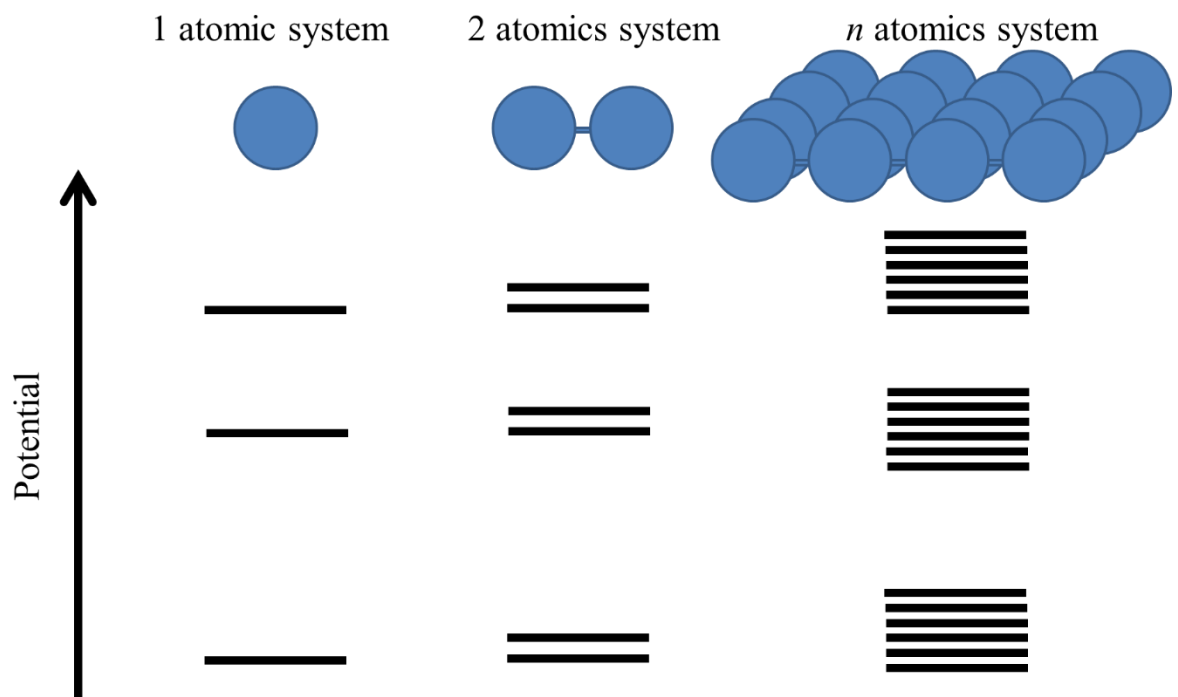


Figure 2.8 The energy level in various atomic system, and the formation of energy band.

From the molecular orbit theory, it explains the level of electrons; when two atoms bonds by the molecular orbit, it will separate to bonding, anti-bonding, and non-bonding orbit. Bonding orbit is an orbit where electrons from two atoms orbits between each other, and anti-bonding is an orbit of electron outside of nuclei of two atoms. Non-bonding orbit is an orbit where electron will not pass through or electron will not be fund in that orbit as in quantum mechanics. The bonding orbit has a low energy. On the contrary, the anti-bonding orbit will be in high energy level because electron will escape the excited state from the interaction of nuclei of the two atoms. In solid crystal, if the number of atoms is infinite resulting in overlap energy-discrete turn to large continuum band by electron filling half of the continuum band isolate to half occupied and half unoccupied band (empty). This is due to the electrons chose to be in the lower energy level which relates to molecular orbit theory.

At the lowest energy level, electrons will form a strong bond. While at the highest energy level, the node will form between pair of electron and the characteristic is similar to anti-bonding in molecular orbit theory. The anti-bonding on highest energy band is called conduction band (CB) or called lowest unoccupied molecular orbital (LUMO), meanwhile, bonding or lowest energy band is called valence band (VB) or called highest occupied molecular orbital (HOMO) in molecular orbit theory. In the case of metal or conductor, conduction band and valence band do not separate or a zero-energy gap. For semiconductor and insulator, conduction band and valence band will distinctively separate and has a gap between conduction band and valence band called band gap (figure 2.9).

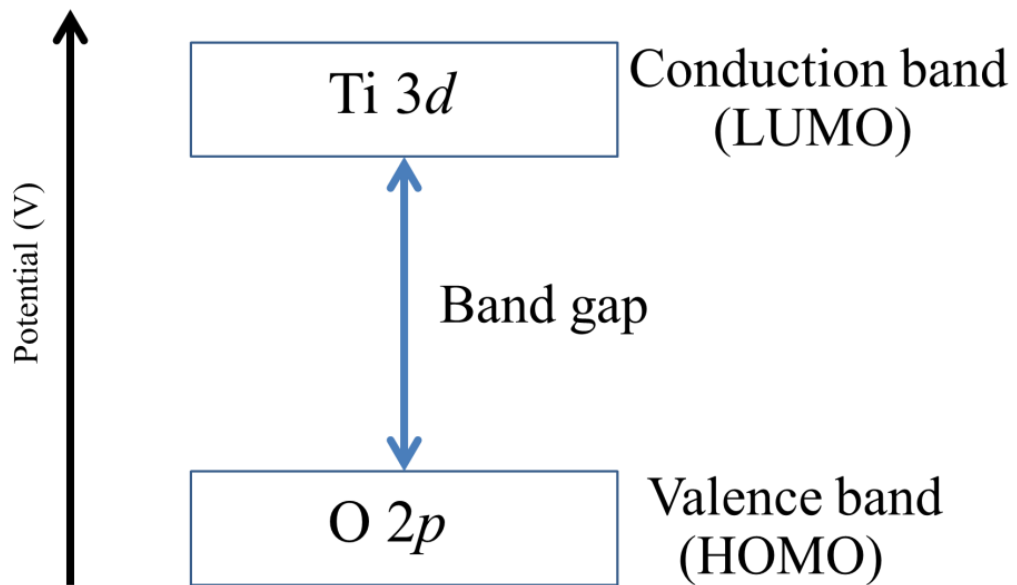


Figure 2.9 The energy band structure of TiO<sub>2</sub> based material.

TiO<sub>2</sub> based material is composed of Ti and O; Ti has electron configuration of [Ar] 4s<sup>2</sup> 3d<sup>2</sup>, and O has electron configuration of 1s<sup>2</sup> 2s<sup>2</sup> 2p<sup>4</sup>. The energy level of both Ti and O are combined resulting in a discrete energy level which O 2p is a valence band occupying unexcited electron, while Ti 3d is a conduction band. Although, anatase TiO<sub>2</sub>, rutile TiO<sub>2</sub>, perovskite titanate or titanate are TiO<sub>2</sub> based materials; they have minor differences in their conduction band, valence band, and band gap.

#### *2.4.1 Metal doping and band-gap narrowing<sup>96-105</sup>*

Generally, pure semiconductor has an electronically neutral property and no electron at conduction band. Due to an electronically neutral property, pure semiconductor is not good at conducting electric current. In order to improve its capacity, adding foreign atoms to semiconductor enhances its ability, and this adding has to be inside the structure of pure semiconductor. This method is called doping. The charge carrier or number of electrons will change when doping foreign atoms. If the doping atom has more electrons, it will make the free electron in the structure increase resulting in negative-type (*n*-type) semiconductor. While doping atom with less electron causes the hole or electron to be insufficient and this is called positive-type (*p*-type) semiconductor. In addition, doping can induce band position or alter band gap. In the past few years, many researches showed that doping titanate compound or TiO<sub>2</sub> by transition metals narrowing the energy band gap of titanate compound or TiO<sub>2</sub> and can work as a photocatalyst for water splitting reaction.

SrTiO<sub>3</sub> is one of the chemical from the TiO<sub>2</sub> based material and has a perovskite structure. SrTiO<sub>3</sub> has a band gap about 3.25 eV and photocatalytic property for water splitting to produce H<sub>2</sub> when loaded with cocatalyst such as Rh or Ru under UV light. By doping of Ti site with Mn, Rh, Cr, and Ru, doping can cause mid-gap state in the

band gap and allow visible light adsorption. Congruently, metal doping TiO<sub>2</sub> by replacing Ti<sup>4+</sup> in TiO<sub>2</sub> lattice with metallic ion form an intra-band in the band gap, moreover, it will be able to absorb visible light and enhance the photocatalytic activity.

Doping with small amount of transition metal ion replacing Ti<sup>4+</sup> in TiO<sub>2</sub> lattice cause charge carrier trapping and extend the life-time of charge carriers. When light irradiated metal doped TiO<sub>2</sub> is shown as the following equation.

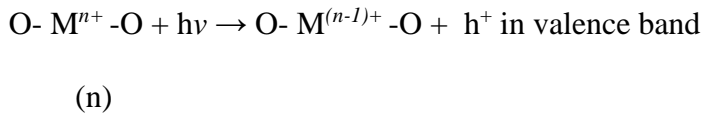
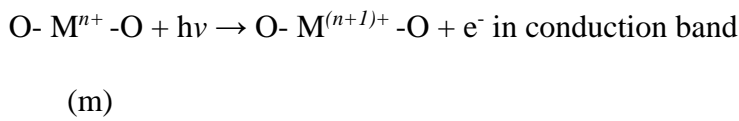
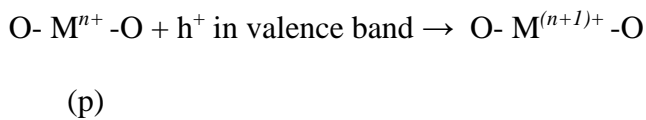
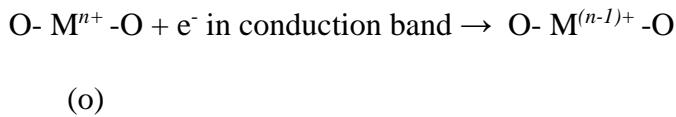


Photo generated electrons or holes can be caught by the metal ions yielding charge carrier trapping as shown below



Its effect is that photo induce charge separation of e<sup>-</sup><sub>cb</sub> and h<sup>+</sup><sub>vb</sub> yield charge carrier in the state of ionic state of metal ion doping TiO<sub>2</sub> lattice. Nonetheless, the equation (N) and (O) can be proceed only when energy level of M<sup>n+</sup>/M<sup>(n-1)+</sup> less than conduction band of TiO<sub>2</sub> and higher than valence band of TiO<sub>2</sub>. The research of metal doping by various metal ions ex. Rh<sup>3+</sup>, Fe<sup>3+</sup>, Mo<sup>5+</sup>, V<sup>4+</sup>, etc. can improve photocatalytic activity and cause TiO<sub>2</sub> to absorb in the range of visible light.

In 2004, Kudo *et. al.* reported the high photocatalytic H<sub>2</sub> production by Rh-doped SrTiO<sub>3</sub> under visible light (λ>420 nm). After doped Rh replacing Ti<sup>4+</sup> in SrTiO<sub>3</sub> lattice

cause the energy band gap of SrTiO<sub>3</sub> to decrease from 3.25 eV to 2.3 eV. As a result, SrTiO<sub>3</sub> can be excited by >420 nm wavelength or the visible light region. Additionally, the capability to produce H<sub>2</sub> is better than non-doped SrTiO<sub>3</sub>. As mentioned above, metal ion doping affects the enhancement of photocatalyst, however, not all transition metal ion i.e. Cr, Ni, etc. cannot enhance the photocatalyst efficiently even if it produces intra-band in the band gap for absorbing visible light. In some cases, photocatalytic activity increases but the light absorption ability remains the same. Therefore, Rh is an interesting transition metal to be used in doping for improving energy band gap and enhance capability of TiO<sub>2</sub> based material and another metal oxide semiconductor photocatalyst.

Nonetheless, the chance of yielding e<sup>-</sup>/h<sup>+</sup> recombination is high in bulk or powdered structure of TiO<sub>2</sub> or SrTiO<sub>3</sub>. Rh doping cause charge separation longer when compared between lifetime of charge separation and reaction time for photocatalytic H<sub>2</sub> production and this phenomenon may happen thus the use of cocatalyst is required. However, using cocatalyst loading at the surface photocatalyst only aid s in photogenerated e<sup>-</sup> or h<sup>+</sup> to combine as electron pool or hole pool. It is not much different from metal doping but at TiO<sub>2</sub> or SrTiO<sub>3</sub>, moreover, the chance where doped metal is near the surface is less than cocatalyst loading. Hence, even doping can decrease band gap and enhance photocatalyst ability, theoretically, lattice structure of metal doping is not efficient in practical. On the other hand, crystal lattice of photocatalyst is thin which causes every atom to arrange at the surface as the case of titanate nanosheet.

## **2.5 Titanate nanosheet with photosensitizer dye**

In the previous topic, the development and enhancement of photocatalyst of TiO<sub>2</sub> based material by metal doping was discussed. The effect of metal doping can make

TiO<sub>2</sub> or SrTiO<sub>3</sub> perovskite to absorb visible light ( $\lambda > 420$  nm). Metal doping mechanism uses metal ion (Rh, Mn, etc.) replacing Ti<sup>4+</sup> in the structure of TiO<sub>2</sub> or SrTiO<sub>3</sub>. Unfortunately, there is a limitation for doping; for example, the ionic radius of metal ion should be similar to Ti<sup>4+</sup> and the doping amount needs to be studied on its effect as the doping may affect the stability of crystal lattice. Hence, it may change the property of TiO<sub>2</sub> based material. Despite its advantages, metal doping is in the process of developing for visible light absorption as it still has a problem with crystal structure. There is another interesting method to enhance the adsorption capacity in the visible light. This is called a dye sensitized system between TiO<sub>2</sub> based material and visible absorbable photosensitizing dye molecules.<sup>106-115</sup> The basic concepts of photocatalytic H<sub>2</sub> production from water by using dye-sensitized photocatalyst semiconductor and photosensitizer dyes are shown in figure 2.10.

Photosensitizer dye are excited by light which makes electron excites from HOMO to LUMO by the same concept as semiconductor which electrons excites from valence band to conduction band by light. Therefore, photogenerated electron will transfer to conduction band of semiconductor. When electron is at conduction band, semiconductor will be excited in the excitation state and make semiconductor active as a catalyst for H<sub>2</sub> production. These electrons are consumed to reduce water and produce H<sub>2</sub> gas. Meanwhile, semiconductor acts as reduction site to produced H<sub>2</sub>. Hence, photosensitizer dye can be oxidized by accepting electron from donor molecules. This phenomenon can occur when photosensitizer dye is adsorbed onto semiconductor and the injection of electron from dye to semiconductor can occur meaning conduction band of semiconductor has lower LUMO level of photosensitizer dye.



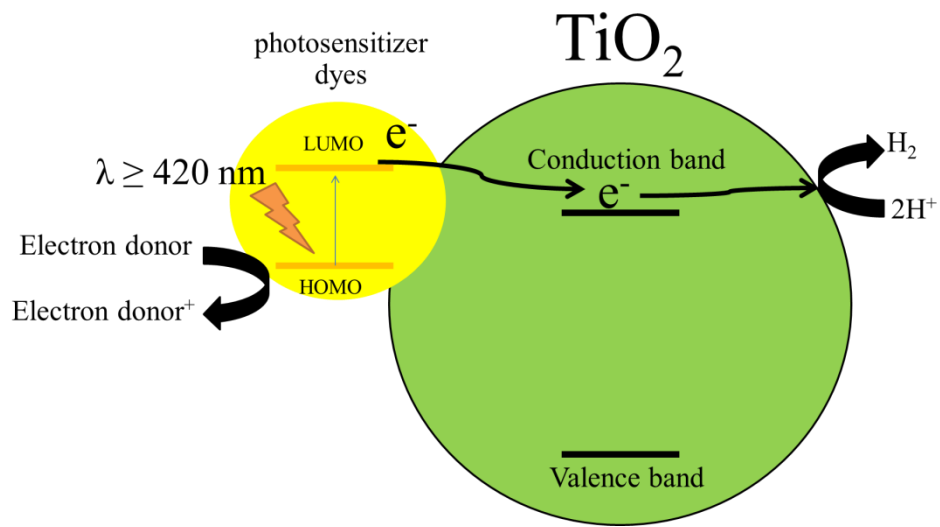


Figure 2.10 The schematic photocatalytic reaction from dye-sensitized TiO<sub>2</sub>

### 2.5.1 Dye-sensitized TiO<sub>2</sub> <sup>115-120</sup>

Since 1980s, after Gratzel et al. successfully produced hybridization of tris (2,2'-bipyridine) ruthenium (II) [Ru(bpy)<sub>3</sub>]<sup>2+</sup> ion on Pt/RuO<sub>2</sub>-loaded TiO<sub>2</sub> particle. Additionally, dye-sensitized material can undergo water splitting reaction under visible light to generate H<sub>2</sub>. From this point on, the development of photocatalytic H<sub>2</sub> production system by metal oxide and photosensitizer dye becomes main researcher until today.

The important variable for enhancing dye-sensitized metal oxide is electron injection from LUMO of dye to conduction band of metal oxide. Moreover, the difference between LUMO level and conduction band level is not the only one that limits the ability of electron injection from dye to metal oxide; this also includes interaction and adsorption of dye molecule on metal oxide particle. Many research showed that the development of molecular structure affecting electron injection. Hirano et al. found that using tris(bipyrimidine)ruthenium(II) [Ru(bpym)<sub>3</sub>]<sup>2+</sup> displaying higher H<sub>2</sub> production efficiency than Ru(bpy)<sub>3</sub><sup>2+</sup> in dye-sensitized TiO<sub>2</sub>. Even though, the LUMO level is not that different. Similarly, adding phosphonate groups of carbonylate group to anchored of Ru(bpy)<sub>3</sub><sup>2+</sup> enhance the H<sub>2</sub> production due to the phosphate group acts as branch attaching to TiO<sub>2</sub> particle resulted in better electron injection.

The structure of metal oxide semiconductor is also important for enhancing the efficacy of electron injection. Many reports showed that hybrid system with metal oxide semiconductor as bulk molecule. Dye will be absorbed at the surface or particle. While photocatalytic H<sub>2</sub> production by hybrid system of (Ru(bpy)<sub>3</sub><sup>2+</sup>) intercalated into layered Niobium oxide were also investigated. The bleaching of Ru(bpy)<sub>3</sub><sup>2+</sup> readily occurs because fast and high efficient electron transfer between Ru(bpy)<sub>3</sub><sup>2+</sup> and layered

niobium oxide. Moreover, many layered oxide semiconductors were also studied as a building block in hybrid system. Nonetheless, nanostructured niobite and  $\text{Ru}(\text{bpy})_3^{2+}$  hybridized were found to be a high photocatalytic  $\text{H}_2$  production. It was higher than intercalated in layered niobium oxide and  $\text{TiO}_2$  particle. This could be explained by their large specific area which able to adsorb more amount of  $\text{Ru}(\text{bpy})_3^{2+}$ , and good binding between  $\text{Ru}(\text{bpy})_3^{2+}$  dye.

Another important factor of dye-sensitized  $\text{TiO}_2$  based material system is a photosensitizer dye. Dyes can be mainly divided to organic dye, and inorganic dye due to their atomic component in their structure. Inorganic dye includes metal complex such as ruthenium or iridium complex, metal porphyrin, phthalocyanine; while organic dye includes only an organic component such as metal-free porphyrin dye (figure 2.11).

### 2.5.2 Organic sensitizers<sup>121-125</sup>

Organic dye has a structure composed of donor and acceptor connecting by  $\pi$ -bridge (figure 2.12). Electron will be passed from donor part via  $\pi$ -bridge to acceptor part under light irradiation. The result of electron donating and accepting under light irradiation causes organic dye to have adsorption response in the visible light region and high adsorption extinction coefficient which is suitable for light harvesting system.

The organic dyes are considered as one of the most promising sensitizers for dye-sensitized semiconductor photocatalyst. Due to organic dye has  $\pi$ -bridge as a key part, it acts as electron donor and acceptor. The expansion of the structure of  $\pi$ -bridge can induce a shift of both the HOMO and LUMO level. Subsequently, we can adjust photo-physical properties of organic dye. In recent years, xanthene dye, coumarin, merocyanine dye, and porphyrin dye have been reported for using as organic sensitizers in the dye-sensitized  $\text{TiO}_2$  system. R. Abe et. al. reported merocyanine-dye-sensitized  $\text{TiO}_2$  photocatalyst with Pt as cocatalyst and I<sup>-</sup> as electron donor in acetonitrile water mix solution. The results demonstrated an improvement of  $\text{H}_2$  production under visible

light not only as photocatalyst but organic dye sensitized semiconductor system. Moreover, they have been used widely as dye-sensitized solar cells.

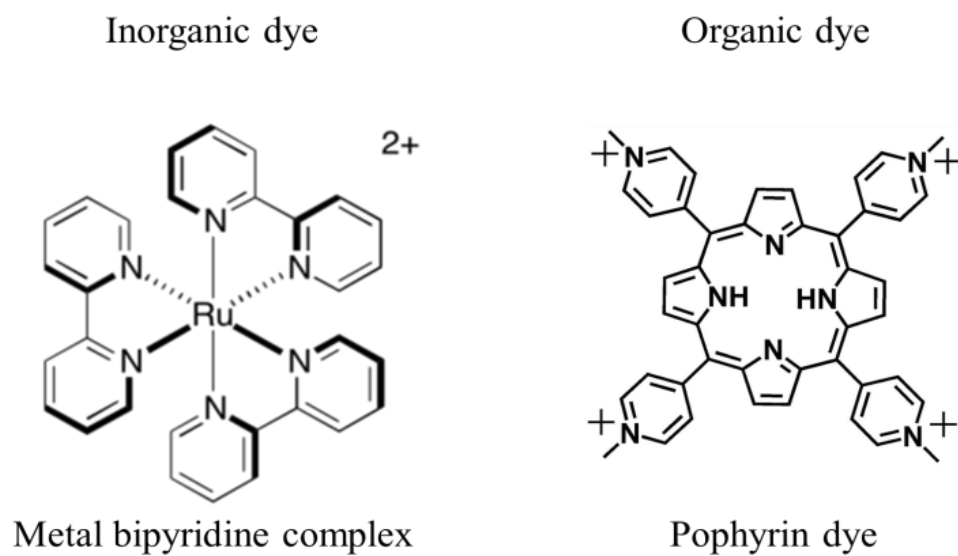


Figure 2.11 Chemical structure of inorganic metal bipyridine complex and organic porphyrin dye.

### 2.5.3 Inorganic dye sensitizers<sup>126-130</sup>

The structure of inorganic dyes composes of cation metal, and non-metalic anion. Inorganic dye has high thermal stability and chemical stability because of ionic bond compared to organic dyes. As mentioned previously, inorganic dye mostly uses as dye sensitized photocatalyst are polypyridyl ruthenium complex due to high stability, well-known redox properties and energy structure, and good respond for visible light. Polypyridyl ruthenium complex can be divided into many groups which are carboxylate polypyridyl ruthenium complex, phosphonate polypyridyl ruthenium complex, and polynuclear bipyridyl ruthenium complex. Each group differs in their adsorption gap or number of metal center. These differences affect dye-sensitized photocatalyst. The adsorption group is also affected electron injection in the dye-sensitized TiO<sub>2</sub> system.

Besides the type of dye sensitizers, there are other factors affecting the ability of dye-sensitized photocatalyst such as linkage or connection between photosensitizer dye and semiconductor photocatalyst. These are important variables for electron injection from dye to semiconductor. In addition, photocatalytic activity of semiconductor plays a crucial role despite the electron injection. If the photocatalytic activity is low, it is difficult for the photocatalyst reaction to progress.

## 2.6 Conclusion

TiO<sub>2</sub> is the first reported semiconductor exhibiting photocatalyst properties for H<sub>2</sub> evolution from water under UV light irradiation. TiO<sub>2</sub> is being used widely as photocatalyst for H<sub>2</sub> evolution due to chemical stability, non-toxic, and inexpensive material. This also includes other TiO<sub>2</sub> based materials i.e. perovskite titanate or layered titanate. However, TiO<sub>2</sub> based material has one flaw in which it's only photocatalytically active under UV light. Therefore, using TiO<sub>2</sub> based material under sunlight is impossible because sunlight contains only a little amount of UV.

The improvement of TiO<sub>2</sub> based material responding to visible light is critical as sunlight contains mostly visible light. In order to improve TiO<sub>2</sub> based materials, there are two main methods which are metal ion doping, and hybrid dye sensitizers. The adjustment of electronic band structure of TiO<sub>2</sub> based material is done by doping metal ion to replace Ti sites of TiO<sub>2</sub> based material; it does not disturb the structure of TiO<sub>2</sub> based materials. A. Kudo et. al., R. Abe et. al., and other research groups denote that

metal doping such as Rh doping enhances the light response ability in the visible light region, hence, it boosts the photocatalyst ability for H<sub>2</sub> production reaction.

While hybrid system of dye sensitizer is also an interesting method to increase the photocatalyst ability under visible light of TiO<sub>2</sub> based material. It is processed by combining TiO<sub>2</sub> based material with dye sensitizers. Dye-sensitized TiO<sub>2</sub> based material has simple principles which dye sensitizer acts as a light receptor generating excited electrons. Then, excited electron will pass through TiO<sub>2</sub> based material for further reaction.

Most of the reported research papers used TiO<sub>2</sub> based materials in the form of powder or bulk molecule; they have low specific surface area to volume of material. Accordingly, electron-hole recombination can occur easily, however, the efficiency of material is lower than expected theoretically. In order to improve this, altering bulk molecule to nano-structured molecule (ex. nanotube or nanosheet) will enhance the capability of TiO<sub>2</sub> based material as photocatalyst especially nanosheet structure. This is due to its characteristic similar to a paper sheet meaning the reaction site increases. Nonetheless, the width of its structure is in nanoscale resulting in energy band gap value in electronic band structure higher indicating nanosheet structured TiO<sub>2</sub> based material is only active under UV or shorter wavelength.

The energy band gap of nanosheets structured TiO<sub>2</sub> based material or titanate nanosheet can be improved by two methods similar as bulk molecule or powder. These methods are metal doping and combining with dye-sensitizer. In this chapter, we explained the system of metal doping, and dye-sensitized in both principles, and usage.

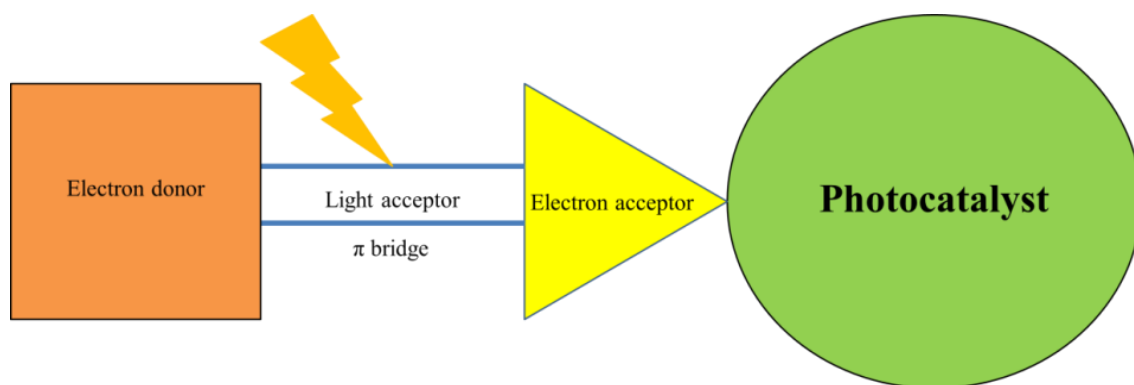


Figure 2.12 Schematic drawing of organic dye-sensitized photocatalyst, the electron donor- $\pi$  bridge-acceptor structure of organic photosensitizer dye.

## References

1. Alberici, R. M. & Jardim, W. F. (1997). Photocatalytic destruction of VOCS in the gas-phase using titanium dioxide. *Applied Catalysis B: Environmental*, 14, 55-68.
2. Al-Hamdi, A. M., Rinner, U., & Sillanpää, M. (2017). Tin dioxide as a photocatalyst for water treatment: A review. *Process Saf. Environ. Prot.*, 107, 190-205.
3. Tasbihi, M., Bendyna, J. K., Notten, P. H., & Hintzen, H. T. (2015). A Short Review on Photocatalytic Degradation of Formaldehyde. *J Nanosci Nanotechnol.* , 15(9), 6386-6396.
4. Akita, T., Okumura, M., Tanaka, K., Ohkuma, K., Kohyama, M., Koyanagi, T., Date, M., Tsubota, S. & Haruta, M. (2005). Transmission electron microscopy observation of the structure of TiO<sub>2</sub> nanotube and Au/TiO<sub>2</sub> nanotube catalyst. *Surface and Interface Analysis*, 37, 265-269.
5. Fujishima, A. & Honda, K. (1972). Electrochemical photolysis of water at a semiconductor electrode. *Nature*, 238, 37-38.
6. Acar, C., Dincer, I., & Naterer, G. F. (2016). Review of photocatalytic water-splitting methods for sustainable hydrogen production. *Int. J. Energy Res.*, 40(11), 1449-1473.
7. Ahmad, H., Kamarudin, S., Minggu, L., & Kassim, M. (2015). Hydrogen from photocatalytic water splitting process: A review. *Renewable Sustainable Energy Rev.*, 43, 599-610.
8. Rahimi, N., Pax, R. A., & Gray, E. M. (2016). Review of functional titanium oxides. I: TiO<sub>2</sub> and its modifications. *Prog. Solid State Chem.*, 44(3), 86-105.
9. Yuan, S., Sheng, Q., Zhang, J., Yamashita, H., & He, D. (2008). Synthesis of thermally stable mesoporous TiO<sub>2</sub> and investigation of its photocatalytic activity. *Microporous*

*Mesoporous Mater.*, 110(2-3), 501-507.

10. Pan, H. (2016). Principles on design and fabrication of nanomaterials as photocatalysts for water-splitting. *RRenewable Sustainable Energy Rev.*, 57, 584-601.
11. Sorescu, A., Ion, R., Nuță, A., & Bunghez-Șuică, I. (2016). A review on the synthesis of silver nanoparticles. *Proceedings of The 4th Global Virtual Conference*.
12. Saifuddin, N., Raziah, A. Z., & Junizah, A. R. (2013). Carbon Nanotubes: A Review on Structure and Their Interaction with Proteins. *J. Chem.*, 2013, 1-18.
13. Gleiter, H. (2004). Nanostructured Materials: Basic Concepts, Microstructure and Properties. *Acta Mater.*, 35(40).
14. Bergmann, C. P., & Andrade, M. J. (2014). *Nanostructured Materials for Engineering Applications*. Berlin: Springer Berlin.
15. Lund, P. (2013). Nanostructured materials for energy applications. *Microelectron. Eng.*, 108, 84-85.
16. Yan, H., Wang, X., Yao, M., & Yao, X. (2013). Band structure design of semiconductors for enhanced photocatalytic activity: The case of TiO<sub>2</sub>. *Prog. Nat. Sci.: Mater. Int.*, 23(4), 402-407.
17. Ola, O., & Maroto-Valer, M. (2015). Review of material design and reactor engineering on TiO<sub>2</sub> photocatalysis for CO<sub>2</sub> reduction. *J. Photochem. Photobiol., C*, 24, 16-42.
18. Khairy, M., & Zakaria, W. (2014). Effect of metal-doping of TiO<sub>2</sub> nanoparticles on their photocatalytic activities toward removal of organic dyes. *Egypt. J. Pet.*, 23(4), 419-426.
19. Harikishore, M., Sandhyarani, M., Venkateswarlu, K., Nellaippan, T., & Rameshbabu, N. (2014). Effect of Ag Doping on Antibacterial and Photocatalytic Activity of Nanocrystalline TiO<sub>2</sub>. *Procedia Mater. Sci.*, 6, 557-566.

20. Albiter, E., Valenzuela, M., Alfaro, S., Valverde-Aguilar, G., & Martínez-Pallares, F. (2015). Photocatalytic deposition of Ag nanoparticles on TiO<sub>2</sub>: Metal precursor effect on the structural and photoactivity properties. *Journal of Saudi Chemical Society*, 19(5), 563-573.
21. Zaleska, A. (2008). Doped-TiO<sub>2</sub>: A Review. *Recent Patents on Engineering*, 2(3), 157-164.
22. Zhang, K., Xu, W., Li, X., Zheng, S., & Xu, G. (2006). Effect of dopant concentration on photocatalytic activity of TiO<sub>2</sub> film doped by Mn non-uniformly. *Open Chemistry*, 4(2).
23. Yuan, R., Zhou, B., Hua, D., & Shi, C. (2014). Effect of metal ion-doping on characteristics and photocatalytic activity of TiO<sub>2</sub> nanotubes for removal of humic acid from water. *Frontiers of Environmental Science & Engineering*, 9(5), 850-860.
24. Li, D., Haneda, H., Hishita, S., & Ohashi, N. (2005). Visible-light-active nitrogen-containing TiO<sub>2</sub> photocatalysts prepared by spray pyrolysis. *Research on Chemical Intermediates*, 31(4-6), 331-341.
25. Nguyen, N. T., Song, M. G., & Bark, C. W. (2017). Narrowing the Band Gap of Nanosized Fe-Doped Bismuth Titanate via Mechanically Induced Oxygen Vacancies. *Journal of Nanoscience and Nanotechnology*, 17(10), 7312-7318.
26. Tan, K. H., Lee, H. W., Chen, J., Dee, C. F., Majlis, B. Y., Soh, A. K., Wu, C., Chai, S., Chang, W. S. (2017). Self-Assembled Heteroepitaxial AuNPs/SrTiO<sub>3</sub>: Influence of AuNPs Size on SrTiO<sub>3</sub> Band Gap Tuning for Visible Light-Driven Photocatalyst. *The Journal of Physical Chemistry C*, 121(25), 13487-13495.
27. Kudo, A., & Miseki, Y. (2009). Heterogeneous photocatalyst materials for water splitting. *Chem. Soc. Rev.*, 38(1), 253-278.

28. Zang, Y., Xie, D., Chen, Y., Wu, X., Li, G., & Plant, D. (2012). Tuning the Structural and Optical Properties of Bismuth Titanate by Different Nd Substitution Content. *Integrated Ferroelectrics*, 133(1), 73-80.
29. Furuhashi, K., Jia, Q., Kudo, A., & Onishi, H. (2013). Time-Resolved Infrared Absorption Study of SrTiO<sub>3</sub> Photocatalysts Codoped with Rhodium and Antimony. *The Journal of Physical Chemistry C*, 117(37), 19101-19106.
30. Gong, J., Liang, J., & Sumathy, K. (2012). Review on dye-sensitized solar cells (DSSCs): Fundamental concepts and novel materials. *Renewable Sustainable Energy Rev.*, 16(8), 5848-5860.
31. Gong, J., Sumathy, K., Qiao, Q., & Zhou, Z. (2017). Review on dye-sensitized solar cells (DSSCs): Advanced techniques and research trends. *Renewable Sustainable Energy Rev.*, 68, 234-246.
32. Weickert, J., & Schmidt-Mende, L. (2014). Solid-State Dye-Sensitized Solar Cells. *Org. Photovoltaics*, 465-494.
33. Bavykin, D. V., Friedrich, J. M. & Walsh, F. C. (2006b). Protonated titanates and TiO<sub>2</sub> nanostructured materials: Synthesis, properties, and applications. *Advanced Materials*, 18, 2807-2824.
34. Bickley, R. I., Gonzalez-carreno, T., Lees, J. S., Palmisano, L. & Tilley, R. J. D. (1991). A structural investigation of titanium dioxide photocatalysts. *Journal of Solid State Chemistry*, 92, 178-190.
35. Smijs, T., & P. (2011). Titanium dioxide and zinc oxide nanoparticles in sunscreens: focus on their safety and effectiveness. *Nanotechnology, Science and Applications*, 95.
36. Mashimo, T., Bagum, R., Ogata, Y., Tokuda, M., Okube, M., Sugiyama, K., Kinemuchi,

- Y., Isobe, H., Yoshiasa, A. (2017). Structure of Single-Crystal Rutile (TiO<sub>2</sub>) Prepared by High-Temperature Ultracentrifugation. *Crystal Growth & Design*, 17(4), 1460-1464.
37. Linsebigler, A. L., Lu, G., & Yates, J. T. (1995). Photocatalysis on TiO<sub>2</sub> Surfaces: Principles, Mechanisms, and Selected Results. *Chemical Reviews*, 95(3), 735-758.
38. Isaak, D. G., Carnes, J. D., Anderson, O. L., Cynn, H., & Hake, E. (1998). Elasticity of TiO<sub>2</sub> rutile to 1800 K. *Physics and Chemistry of Minerals*, 26(1), 31-43.
39. Labat, F., Baranek, P., Domain, C., Minot, C., & Adamo, C. (2007). Density functional theory analysis of the structural and electronic properties of TiO<sub>2</sub> rutile and anatase polytypes: Performances of different exchange-correlation functionals. *Journal of Chemical Physics*, 126(15), 154703.
40. Jeffery, A. A., Pradeep, A., & Rajamathi, M. (2016). Preparation of titanate nanosheets and nanoribbons by exfoliation of amine intercalated titanates. *Phys. Chem. Chem. Phys.*, 18(18), 12604-12609.
41. Nakagawa, K., Yamaguchi, K., Yamada, K., Sotowa, K., Sugiyama, S., & Adachi, M. (2012). Synthesis and Characterization of Surface-Functionalized Layered Titanate Nanosheets Using Lamellar Self-Assembly as a Template. *European Journal of Inorganic Chemistry*, 2012(16), 2741-2748.
42. Ban, T., Nakagawa, T., & Ohya, Y. (2015). Bottom-Up Synthesis of Titanate Nanosheets in Aqueous Sols and Their Morphology Change by the Addition of Organic Ligands and Dialysis. *Crystal Growth & Design*, 15(4), 1801-1807.
43. Hayashi, H., Nakamura, T., & Ebina, T. (2016). Hydrothermal synthesis of sodium titanate nanosheets using a supercritical flow reaction system. *Journal of the Ceramic Society of Japan*, 124(1), 74-78.

44. Nakato, T., Kawamata, J., & Takagi, S. (2017). *Inorganic nanosheets and nanosheet-based materials: fundamentals and applications of two-dimensional systems*. Tokyo: Springer.
45. Sasaki, T., & Watanabe, M. (1997). Semiconductor Nanosheet Crystallites of Quasi-TiO<sub>2</sub> and Their Optical Properties. *The Journal of Physical Chemistry B*, 101(49), 10159-10161.
46. A., & Lockwood David, J. (2006). *Self-organized nanoscale materials*. New York: Springer.
47. hrysicopoulou, P., Davazoglou, D., Trapalis, C., & Kordas, G. (1998). Optical properties of very thin (<100 nm) sol-gel TiO<sub>2</sub> films. *Thin Solid Films*, 323(1-2), 188-193.
48. Mo, S. D. & Ching, W. Y. (1995). Electronic and optical properties of three phases of titanium dioxide: Rutile, anatase, and brookite. *Physical Review B*, 51, 13023-13032.
49. Gang, G., Lee, Y., Gwak, J., Lee, D., Jeong, B., Park, S., & Choe, B. (2002). Structural and Optical Properties of TiO<sub>2</sub> Thin Films Prepared by RF Reactive Magnetron Sputtering. *Korean Journal of Materials Research*, 12(6), 452-457.
50. Shevlin, S. A., & Woodley, S. M. (2010). Electronic and Optical Properties of Doped and Undoped (TiO<sub>2</sub>)<sub>n</sub> Nanoparticles. *The Journal of Physical Chemistry C*, 114(41), 17333-17343.
51. Burrafato, G. (1993). Determination of the Cation Exchange Capacity of Clays by Surface Tension Measurements. *Clay Minerals*, 28(3), 475-481.
52. Ogawa, M., & Takizawa, Y. (1999). Intercalation of Alkylammonium Cations into a Layered Titanate in the Presence of Macrocyclic Compounds. *Chem. Mater.*, 11(1), 30-32.

53. Kikkawa, S., Yasuda, F., & Koizumi, M. (1985). Ionic conductivities of Na<sub>2</sub>Ti<sub>3</sub>O<sub>7</sub>, K<sub>2</sub>Ti<sub>4</sub>O<sub>9</sub> and their related materials. *Mater. Res. Bull.*, 20(10), 1221-1227.
54. Kaneko, M., Tokuno, K., Yamagishi, K., Wada, T., & Hasegawa, T. (2017). Photocatalytic Activity of Titanium Dioxide Powder Fabricated from an Anodized Titanium Sheet under Ultra-Violet and Visible Light Irradiation. *Journal of Surface Engineered Materials and Advanced Technology*, 07(01), 13-23.
55. Kisch, H. (2015). *Semiconductor photocatalysis: principles and applications*. Weinheim, Germany: Wiley-VCH.
56. Hoffmann, M. R., Martin, S. T., Choi, W., & Bahnemann, D. W. (1995). Environmental Applications of Semiconductor Photocatalysis. *Chemical Reviews*, 95(1), 69-96.
57. Sato, H., Ono, K., Sasaki, T., Yamagishi, A. (2003). First-Principles Study of Two-Dimensional Titanium Dioxides. *J. Phys. Chem. B*, 107(36), 9824-9828.
58. Jafari, T., Moharreri, E., Amin, A., Miao, R., Song, W., & Suib, S. (2016). Photocatalytic Water Splitting—The Untamed Dream: A Review of Recent Advances. *Molecules*, 21(7), 900.
59. Zhang, X., Du, Y., Zhou, Z., & Guo, L. (2010). A simplified method for synthesis of band-structure-controlled (CuIn)<sub>x</sub>Zn<sub>2(1-x)</sub>S<sub>2</sub> solid solution photocatalysts with high activity of photocatalytic H<sub>2</sub> evolution under visible-light irradiation. *Int. J. Hydrogen Energy*, 35(8), 3313-3321.
60. Xiong, X., Zhang, X., & Xu, Y. (2016). Concentration dependent effect of CuCl<sub>2</sub> on the photocatalytic degradation of phenol over anatase, rutile and brookite TiO<sub>2</sub>. *RSC Adv.*, 6(44), 38169-38175.
61. Fujishima, A., Zhang, X., & Tryk, D. (2008). TiO<sub>2</sub> photocatalysis and related surface

phenomena. *Surf. Sci. Rep.*, 63(12), 515-582.

62. Castellote, M., & Bengtsson, N. (2011). Principles of TiO<sub>2</sub> Photocatalysis. *Applications of Titanium Dioxide Photocatalysis to Construction Materials*, 5-10.
63. Fujishima, A., Rao, N. T., & Tryk, D. (2000). Titanium dioxide photocatalysis. *Journal of Photochemistry and Photobiology C: Photochemistry Reviews*, 1(1), 1-21.
64. Nakata, K., & Fujishima, A. (2012). TiO<sub>2</sub> photocatalysis: Design and applications. *Journal of Photochemistry and Photobiology C: Photochemistry Reviews*, 13(3), 169-189.
65. Arabatzis, I. (2003). Characterization and photocatalytic activity of Au/TiO<sub>2</sub> thin films for azo-dye degradation. *Journal of Catalysis*, 220(1), 127-135.
66. Maeda, K., & Domen, K. (2010). Photocatalytic Water Splitting: Recent Progress and Future Challenges. *The Journal of Physical Chemistry Letters*, 1(18), 2655-2661.
67. Maeda, K. (2013). Z-Scheme Water Splitting Using Two Different Semiconductor Photocatalysts. *ACS Catalysis*, 3(7), 1486-1503.
68. Oxide Semiconductors (ZnO, TiO<sub>2</sub>, Fe<sub>2</sub>O<sub>3</sub>, WO<sub>3</sub>, etc.) as Photocatalysts for Water Splitting. (2017). *Electrochemical Energy Storage and Conversion Photochemical Water Splitting*, 161-222.
69. Kudo, A. (2011). Z-scheme photocatalyst systems for water splitting under visible light irradiation. *MRS Bulletin*, 36(1), 32-38.
70. Hashimoto, K., Irie, H., Fujishima, A. (2005). TiO<sub>2</sub> Photocatalysis: A Historical Overview and Future Prospects. *Japanese Journal of Applied Physics*, 44(1).
71. Kim, K., & Barteau, M. (1989). Reactions of methanol on TiO<sub>2</sub>(001) single crystal surfaces. *Surface Science*, 223(1-2), 13-32.

72. Kanai, N., Nuida, T., Ueta, K., Hashimoto, K., Watanabe, T., & Ohsaki, H. (2004). Photocatalytic efficiency of TiO<sub>2</sub>/SnO<sub>2</sub> thin film stacks prepared by DC magnetron sputtering. *Vacuum*, 74(3-4), 723-727.
73. Gaya, U.I. and Abdullah, A.H. (2008) Heterogeneous Photocatalytic Degradation of Organic Contaminants over Titanium Dioxide: A Review of Fundamentals, Progress and Problems. *Journal of Photochemistry and Photobiology C: Photochemistry Reviews*, 9, 1-12.
74. Yousif, E., & Haddad, R. (2013). Photodegradation and photostabilization of polymers, especially polystyrene: review. *SpringerPlus*, 2(1), 398.
75. Irawaty, W., Friedmann, D., Scott, J. & Amal, R. (2011). Relationship between mineralization kinetics and mechanistic pathway during malic acid photodegradation. *Journal of Molecular Catalysis A: Chemical*, 335, 151-157.
76. Galindo, F., Gómez, R., & Aguilar, M. (2008). Photodegradation of the herbicide 2,4-dichlorophenoxyacetic acid on nanocrystalline TiO<sub>2</sub>-CeO<sub>2</sub> sol-gel catalysts. *Journal of Molecular Catalysis A: Chemical*, 281(1-2), 119-125.
77. urki, A., Guillard, C., Dappozze, F., Berhault, G., Ksibi, Z., & Kochkar, H. (2014). Design of TiO<sub>2</sub> nanomaterials for the photodegradation of formic acid – Adsorption isotherms and kinetics study. *Journal of Photochemistry and Photobiology A: Chemistry*, 279, 8-16.
78. Matthews, R. (1991). Photooxidative degradation of coloured organics in water using supported catalysts. TiO<sub>2</sub> on sand. *Water Res.*, 25(10), 1169-1176.
79. Houas, A. (2001). Photocatalytic degradation pathway of methylene blue in water. *Appl. Catal., B*, 31(2), 145-157.

80. Wetchakun, K., Wetchakun, N., & Phanichphant, S. (2015). Optimization of horizontal photocatalytic reactor for decolorization of methylene blue in water. *Desalin. Water Treat.*, 57(22), 10286-10294.
81. Patsoura, A., Kondarides, D. I. & Verykios, X. E. (2006). Enhancement of photoinduced hydrogen production from irradiated Pt/TiO<sub>2</sub> suspensions with simultaneous degradation of azo-dyes. *Applied Catalysis B: Environmental*, 64, 171-179.
82. Li, R., & Li, C. (2017). Photocatalytic Water Splitting on Semiconductor-Based Photocatalysts. *Advances in Catalysis*, 1-57.
83. Ahsan, S. S., Gumus, A., & Erickson, D. (2013). Redox mediated photocatalytic water-splitting in optofluidic microreactors. *Lab Chip*, 13(3), 409-414.
84. Esch, T. R., & Bredow, T. (2017). Band positions of Rutile surfaces and the possibility of water splitting. *Surface Science*, 665, 20-27.
85. Li, Y. H., Wang, Y., Zheng, L. R., Zhao, H. J., Yang, H. G., & Li, C. (2017). Water-soluble inorganic photocatalyst for overall water splitting. *Applied Catalysis B: Environmental*, 209, 247-252.
86. Filice, S., Compagnini, G., Fiorenza, R., Scirè, S., D'Urso, L., Fragalà, M. E., Russo, P., Fazio, E., Scalese, S. (2017). Laser processing of TiO<sub>2</sub> colloids for an enhanced photocatalytic water splitting activity. *Journal of Colloid and Interface Science*, 489, 131-137.
87. Zhu, Z., Kao, C., Tang, B., Chang, W., & Wu, R. (2016). Efficient hydrogen production by photocatalytic water-splitting using Pt-doped TiO<sub>2</sub> hollow spheres under visible light. *Ceramics International*, 42(6), 6749-6754.
89. Sreethawong, T., Junbua, C., & Chavadej, S. (2009). Photocatalytic H<sub>2</sub> production from

- water splitting under visible light irradiation using Eosin Y-sensitized mesoporous-assembled Pt/TiO<sub>2</sub> nanocrystal photocatalyst. *Journal of Power Sources*, 190(2), 513-524.
90. Preethi, V., & Kanmani, S. (2014). Photocatalytic hydrogen production using Fe<sub>2</sub>O<sub>3</sub>-based core shell nano particles with ZnS and CdS. *International Journal of Hydrogen Energy*, 39(4), 1613-1622.
  91. Neamen, D. A. (2008). *An introduction to semiconductor devices*. Boston, Mass.: McGraw-Hill Higher Education.
  92. Housecroft, C. E. (2013). *Inorganic chemistry*. Moore Park: Content Technologies, Inc.
  93. Razak, N. A., Zabidi, N. A., & Rosli, A. N. (2017). A first principle study of band structure of tetragonal barium titanate.
  94. Sannigrahi, A. B., & Kar, T. (1988). Molecular orbital theory of bond order and valency. *Journal of Chemical Education*, 65(8), 674.
  95. Rauk, A. (2001). *Orbital interaction theory of organic chemistry*. New York: Wiley-Interscience.
  96. Liu, B., Chen, H. M., Liu, C., Andrews, S. C., Hahn, C., & Yang, P. (2013). Large-Scale Synthesis of Transition-Metal-Doped TiO<sub>2</sub> Nanowires with Controllable Overpotential. *Journal of the American Chemical Society*, 135(27), 9995-9998.
  97. Tseng, L., Luo, X., Bao, N., Ding, J., Li, S., & Yi, J. (2016). Structures and properties of transition-metal-doped TiO<sub>2</sub> nanorods. *Materials Letters*, 170, 142-146.
  98. Wang, Y., Zhang, R., Li, J., Li, L., & Lin, S. (2014). First-principles study on transition metal-doped anatase TiO<sub>2</sub>. *Nanoscale Research Letters*, 9(1), 46.
  99. Gu, D., Yang, B., & Hu, Y. (2008). V and N co-doped nanocrystal anatase TiO<sub>2</sub>

photocatalysts with enhanced photocatalytic activity under visible light irradiation. *Catalysis Communications*, 9(6), 1472-1476.

100. Sanni, S. O., & Idemudia, O. G. (2014). Synthesis and Characterization of Rhodium Doped on TiO<sub>2</sub>/HCP for Enhanced Photocatalytic Performance on Pentachlorophenol. *Journal of Nanomaterials*, 2014, 1-8.
101. Bae, D., Han, K., & Choi, S. (1997). Fabrication and characterization of Ru-doped TiO<sub>2</sub> composite membranes by the sol-gel process. *Materials Letters*, 33(1-2), 101-105.
102. Kuncewicz, J., & Ohtani, B. (2016). Rhodium-doped titania photocatalysts with two-step bandgap excitation by visible light—influence of the dopant concentration on photosensitization efficiency. *RSC Adv.*, 6(94), 91658-91658.
103. Kudo, A., Kato, H., & Tsuji, I. (2005). Strategies for the Development of Visible-Light-Driven Photocatalysts for Water Splitting. *Chem.Lett.*, 36(13).
104. Takayama, T., Tsuji, I., Aono, N., Harada, M., Okuda, T., Iwase, A., . . . Kudo, A. (2017). Development of Various Metal Sulfide Photocatalysts Consisting of d0, d5, and d10 Metal Ions for Sacrificial H<sub>2</sub> Evolution under Visible Light Irradiation. *Chemistry Letters*, 46(4), 616-619.
105. Maeda, K., & Domen, K. (2016). Development of Novel Photocatalyst and Cocatalyst Materials for Water Splitting under Visible Light. *Bulletin of the Chemistry Society of Japan*, 47(36).
106. Gong, J., Liang, J., & Sumathy, K. (2012). Review on dye-sensitized solar cells (DSSCs): Fundamental concepts and novel materials. *Renewable Sustainable Energy Rev.*, 16(8), 5848-5860.
107. Gong, J., Sumathy, K., Qiao, Q., & Zhou, Z. (2017). Review on dye-sensitized solar cells

- (DSSCs): Advanced techniques and research trends. *Renewable Sustainable Energy Rev.*, 68, 234-246.
108. Weickert, J., & Schmidt-Mende, L. (2014). Solid-State Dye-Sensitized Solar Cells. *Org. Photovoltaics*, 465-494.
  109. Sahara, G., Abe, R., Higashi, M., Morikawa, T., Maeda, K., Ueda, Y., & Ishitani, O. (2015). Photoelectrochemical CO<sub>2</sub> reduction using a Ru(ii)–Re(i) multinuclear metal complex on a p-type semiconducting NiO electrode. *Chem. Commun.*, 51(53), 10722-10725.
  110. Abe, R., Shinmei, K., Hara, K., & Ohtani, B. (2009). Robust dye-sensitized overall water splitting system with two-step photoexcitation of coumarin dyes and metal oxide semiconductors. *Chem. Commun.*, (24), 3577.
  111. Kumagai, H., Sahara, G., Maeda, K., Higashi, M., Abe, R., & Ishitani, O. (2017). Hybrid photocathode consisting of a CuGaO<sub>2</sub> p-type semiconductor and a Ru(ii)–Re(i) supramolecular photocatalyst: non-biased visible-light-driven CO<sub>2</sub> reduction with water oxidation. *Chem. Sci.*, 8(6), 4242-4249.
  112. Mathew, S., Yella, A., Gao, P., Humphry-Baker, R., Curchod, B. F., Ashari-Astani, N., Grätzel, M. (2014). Dye-sensitized solar cells with 13% efficiency achieved through the molecular engineering of porphyrin sensitizers. *Nat. Chem.*, 6(3), 242-247.
  113. Ferber, J., Stangl, R., Luther, J. (1998). An electrical model of the dye-sensitized solar cell. *Sol. Energy Mater. Sol. Cells.*, 53(1-2), 29-54.
  114. Anandan, S. (2007). Recent improvements and arising challenges in dye-sensitized solar cells. *Sol. Energy Mater. Sol. Cells*, 91(9), 843-846.
  115. Korfiatis, D. P., Potamianou, S. F., & Thoma, K. T. (2008). Modeling of dye-sensitized

titanium dioxide solar cells. *Ionics*, 14, 545-548.

116. Deb, S. K. (2005). Dye-sensitized TiO<sub>2</sub> thin-film solar cell research at the National Renewable Energy Laboratory (NREL). *Solar Energy Materials and Solar Cells*, 88(1), 1-10.
117. Daut, I., Fitra, M., Irwanto, M., Gomesh, N., & Irwan, Y. M. (2013). TiO<sub>2</sub> Dye Sensitized Solar Cells Cathode Using Recycle Battery. *Journal of Physics: Conference Series*, 423, 012055.
118. to, S., Zakeeruddin, S., Humphry-Baker, R., Liska, P., Charvet, R., Comte, P., Miura, H., Takata, M., Uchida, S. Grätzel, M. (2006). High-Efficiency Organic-Dye- Sensitized Solar Cells Controlled by Nanocrystalline-TiO<sub>2</sub> Electrode Thickness. *Advanced Materials*, 18(9), 1202-1205.
119. GRÄTZEL, M. (2000). Perspectives for dye-sensitized nanocrystalline solar cells. *Photovoltaics*, 9(21), 2630.
120. Kalyanasundaram, K. (2010). *Dye-sensitized solar cells*. Lausanne: EPEL Press.
121. Anselmi, C., Mosconi, E., Pastore, M., Ronca, E., & Angelis, F. D. (2012). Adsorption of organic dyes on TiO<sub>2</sub> surfaces in dye-sensitized solar cells: interplay of theory and experiment. *Physical Chemistry Chemical Physics*, 14(46), 15963.
122. Hara, K., Wang, Z., Koumura, N., & Saito, K. (2006). Efficient Organic-Dye-Sensitized Nanocrystalline TiO<sub>2</sub> Solar Cells. *2006 IEEE 4th World Conference on Photovoltaic Energy Conference*.
123. Li, Q., & Li, Z. (2013). Theoretical study on aggregation of organic dyes on TiO<sub>2</sub> surface in dye-sensitized solar cells. *International Photonics and Optoelectronics Meetings (POEM)*.

124. Horiuchi, T., Miura, H., & Uchida, S. (2004). Highly-Efficient Metal-Free Organic Dyes for Dye-Sensitized Solar Cells. *Journal of Photochemistry and Photobiology A: Chemistry*, 35(15).
125. Higashino, T., & Imahori, H. (2015). Porphyrins as excellent dyes for dye-sensitized solar cells: recent developments and insights. *Dalton Transactions*, 44(2), 448-463.
126. Funaki, T., Yanagida, M., Onozawa-Komatsuzaki, N., Kawanishi, Y., Kasuga, K., & Sugihara, H. (2009). Ruthenium (II) complexes with  $\pi$  expanded ligand having phenylene-ethynylene moiety as sensitizers for dye-sensitized solar cells. *Solar Energy Materials and Solar Cells*, 93(6-7), 729-732.
127. Aghazada, S., Ren, Y., Wang, P., & Nazeeruddin, M. K. (2017). Effect of Donor Groups on the Performance of Cyclometalated Ruthenium Sensitizers in Dye-Sensitized Solar Cells. *Inorganic Chemistry*, 56(21), 13437-13445.
128. Maeda, K., Sahara, G., Eguchi, M., & Ishitani, O. (2015). Hybrids of a Ruthenium(II) Polypyridyl Complex and a Metal Oxide Nanosheet for Dye-Sensitized Hydrogen Evolution with Visible Light: Effects of the Energy Structure on Photocatalytic Activity. *ACS Catal.*, 5(3), 1700-1707.
129. Ozawa, H., Kawaguchi, H., Okuyama, Y., & Arakawa, H. (2013). Ruthenium Sensitizers with 2,2'-Bipyrimidine or a 5,5'-Disubstituted 2,2'-Bipyrimidine Ligand: Synthesis, Photo- and Electrochemical Properties, and Application to Dye-Sensitized Solar Cells. *Eur. J. Inorg. Chem.*, 2013(29), 5187-5195.
130. Youngblood, W. J., Lee, S. A., Maeda, K., & Mallouk, T. E. (2010). Visible Light Water Splitting Using Dye-Sensitized Oxide Semiconductors. *Acc. Chem. Res.*, 41(16).

# Chapter 3

## Synthesis of Rh doped Titanate Nanosheet and Investigation of Its Effect on Photocatalytic Activity for Organic Dye Degradation

### 3.1 Introduction

Two-dimensional titanate nanosheets (TiNSs) prepared from layered titanate [ $\text{H}_2\text{Ti}_n\text{O}_{2n+1}$  ( $n \geq 3$ ), or lepidrocrocite-type titanate,  $\text{H}_n\text{Ti}_{2-n/4}\square_{n/4}\text{O}_4$  ( $n \sim 0.7$ ;  $\square$ , vacancy)] have attracted attention due to exhibition of unique structural features such as high aspect ratios (thickness: 1 nm, surface area:  $\sim$  several  $\mu\text{m}^2$ ). Furthermore, they have useful physicochemical properties i.e. high cation-exchangeability, wide-bandgap semiconducting properties, high dielectric constant, and photocatalytic ability. Thus, TiNSs have been studied by many researchers as gas barrier, water purification, functional coating reagent, self-cleaning material, and etc.<sup>1-5</sup> In addition, titanate nanosheets (TiNSs) can be prepared from alkaline titanate such as  $\text{A}_2\text{Ti}_n\text{O}_{2n+1}$  (A: alkaline metal,  $n = 3, 4, \dots$ ). Generally, the typical alkaline compounds for studying the photocatalytic abilities are  $\text{Na}_2\text{Ti}_3\text{O}_7$  and/or  $\text{K}_2\text{Ti}_4\text{O}_9$  which have been studied intensively over the past decades.<sup>6-8</sup> These TiNSs can work as a photocatalyst. However, the photocatalytic activity of these nanosheets is not sufficient for their application as a self-cleaning material. Thus, the improvement in their photocatalytic activity is desired.

Metal doping is one of the methods for refining and improving their photocatalytic activity.<sup>9-10</sup> The metal doping method is a process in which other metal atoms are incorporated into the Ti sites of titanate and is known to improve photocatalytic activity. The improvement originates from the formation of a new energy band by orbital mixing and change in the carrier concentration. The photoredox activity of titanate is affected by the adjustment of the photocatalytic properties. Recently, there have been many investigations of the metal doping of TiNSs.

Ida *et al.* reported the photocatalytic activity of Rh-doped lepidrocrocite-type TiNSs, prepared by the exfoliation of Rh-doped  $\text{H}_n\text{Ti}_{2-n/4}\square_{n/4}\text{O}_4$  ( $n \sim 0.7$ ;  $\square$ , vacancy), which

was synthesized by solid-state reaction.<sup>11</sup> In this work, they found that Rh atoms incorporated into the Ti sites of the TiNSs acted as H<sub>2</sub> production reaction sites for photo-induced water splitting. Milanović *et al.* also reported the synthesis of Nb-doped lepidrocrocite-type TiNSs and the effect of Nb doping on the photodegradation of methylene blue (MB) in water. Furthermore, Sasaki *et al.* reported the synthesis of lepidrocrocite-type Ti<sub>0.6</sub>Fe<sub>0.4</sub>O<sub>2</sub> and Ti<sub>0.8</sub>Co<sub>0.2</sub>O<sub>2</sub> nanosheets.<sup>13-14</sup> The doping 3d metals into the Ti sites affected the crystal and electronic structures of the lepidrocrocite-type TiNSs. The metal doping and effect of doping on the photocatalytic properties of TiNSs prepared by exfoliation of an H<sub>2</sub>Ti<sub>n</sub>O<sub>2n+1</sub> crystal have not been reported until now.

H<sub>2</sub>Ti<sub>3</sub>O<sub>7</sub> crystal can be prepared from layered Na<sub>2</sub>Ti<sub>3</sub>O<sub>7</sub> by the Na<sup>+</sup>/H<sup>+</sup> ion-exchange. The basic layer architecture of H<sub>2</sub>Ti<sub>3</sub>O<sub>7</sub> was maintained with nearly unchanged structure from that in Na<sub>2</sub>Ti<sub>3</sub>O<sub>7</sub> which the structure was determined by Andersson and Wadsley.<sup>15</sup> Na<sub>2</sub>Ti<sub>3</sub>O<sub>7</sub> consists of edge-shared and corner-shared TiO<sub>6</sub> octahedral, which the sheet layers are separated by the Na<sup>+</sup> ion. Unlike the lepidrocrocite-type titanate, H<sub>n</sub>Ti<sub>2- $\frac{n}{4}$</sub> □ <sub>$\frac{n}{4}$</sub> O<sub>4</sub> (n ~ 0.7; □, vacancy), the H<sub>2</sub>Ti<sub>3</sub>O<sub>7</sub> crystals have no vacancies in their basic layer architecture. The metal doping can be done only by replacing Ti atom to another metal such as Mn, Fe, and so on.<sup>12-14</sup> Thus, the effect of doping will occur due to the replacement of Ti sites which are in the skeleton structure of TiNSs.

To investigate the photocatalytic activity of TiNSs, the degradation of organic compound is one of well-known techniques.<sup>16</sup> The degradation of organic compound can be occurred by photogenerated holes from TiNSs or via the hydroxyl radical which came from the oxidation water molecules adsorbed on TiNSs surface. The organic compound must be adsorbed on the surface of TiNSs, while the hydroxyl radical can attack the organic compound at the interface or beyond the particle surface. In this study, we selected methylene blue and methyl orange as a model of photocatalytic degradation base on the cationic and anionic which results in good or poor adsorption by TiNSs because the TiNSs have only the cationic exchange properties.<sup>17</sup>

Methylene blue (MB) or methylthioninium chloride is a dye with the color of dark green and gives blue color when solute in water. MB is a formal derivative of phenothiazine (figure 3.1.a). The degradation pathway of MB by TiO<sub>2</sub> has been reported by Houas *et al.* (2001).<sup>18</sup> The reaction starts from the adsorption and the product comes out as a non-color solution at the end of reaction. The final products are CO<sub>2</sub>, SO<sub>4</sub><sup>2-</sup>, NH<sub>4</sub><sup>+</sup>, and NO<sub>3</sub><sup>-</sup>. MB is a cation when solute in water, then it can be adsorbed by TiNS due to the electrostatic interaction between cationic MB and anionic TiNS. Methyl orange (MO) is one of the azo dyes with azo band (-N=N-) connected to aromatic structure (figure 3.1.b). MO is usually used in the photodegradation model of azo dye.<sup>19-21</sup> MO will be anionic when it solutes in a solution such as water. Therefore, MO cannot be electrostatically adsorbed on TiNS surface because of the electrostatic repulsion among MO and TiNS. MO is used as a poor adsorption capacity dye for TiNS. For MB, it shows an extensive adsorption theoretically. Nevertheless, there are no reports on the ability of MB dye or MO dye absorption by TiNS especially in the colloidal suspension solution state.

In this study, Rh-doped TiNSs (Ti<sub>3</sub>NS:Rh<sub>x</sub>, x is the molar amount of Rh per 1 mol of nanosheets) were synthesized as a Na<sub>2</sub>Ti<sub>3-x</sub>Rh<sub>x</sub>O<sub>7</sub> crystal by solid-state reaction. The

electronic band structure of the synthesized Ti<sub>3</sub>NS:Rh<sub>x</sub> was characterized by photocurrent and photoabsorption measurements. The adsorption activity and photodegradation of organic dye; methylene blue (MB) and methyl orange(MO), in the presence of Ti<sub>3</sub>NS:Rh<sub>x</sub> was investigated to evaluate its cation exchange activity, photocatalytic activity, and the effect of Rh doping on this kind of titanate nanosheet.

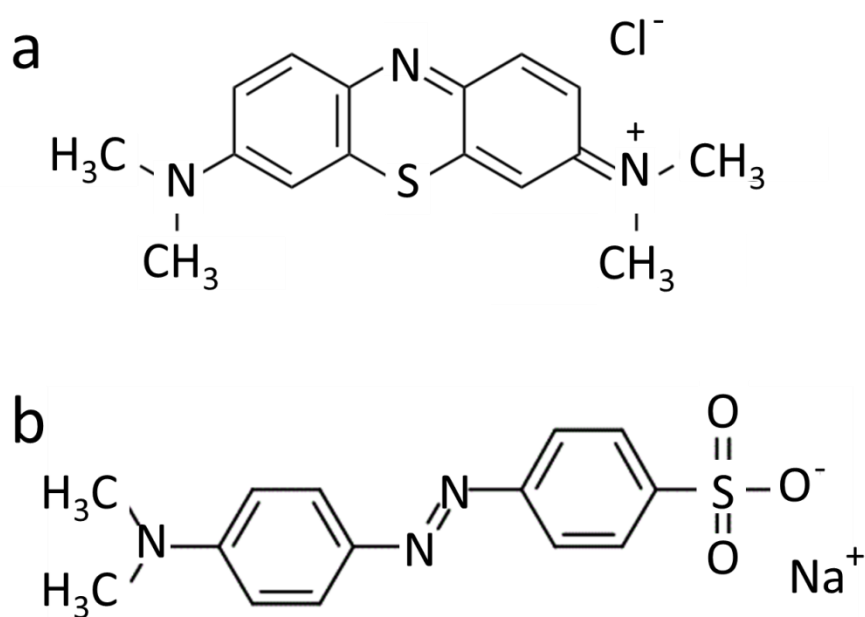


Figure 3.1 The chemical structure of methylene blue (a) and methyl orange (b).

## 3.2 Experimental

### *Reagents and materials*

Sodium carbonate  $\text{Na}_2\text{CO}_3$  (99.9%) from Wako Pure Chemical Industries Co., anatase-type  $\text{TiO}_2$  (99.7%) from High Purity Chemicals Co.,  $\text{Rh}_2\text{O}_3$  (99.9%) from Wako Pure Chemical Industries Co., methylamine ( $\text{CH}_3\text{NH}_2$ , 40wt.% solution) and tetramethylammonium hydroxide (TMAOH, 26wt.% solution) from Tokyo Chemical Industry Co., MO ( $\text{C}_{14}\text{H}_{14}\text{N}_3\text{NaO}_3\text{S}$ , Sodium 4-[[4-(dimethylamino)phenyl]diazanyl]benzene-1-sulfonate) from Wako Pure Chemical Industries Co. and MB ( $\text{C}_{16}\text{H}_{18}\text{N}_3\text{SCl}\cdot 3\text{H}_2\text{O}$ , 3,7-bis(dimethylamino)-phenothiazin-5-ium chloride) from Kanto chemical Co. were used as received.

### *Synthesis of Rh-doped sodium titanate*

$\text{Na}_2\text{Ti}_{3-x}\text{Rh}_x\text{O}_7$  was synthesized using a modified form of the solid-state reaction method reported by Izawa *et al.*<sup>22</sup> The material was synthesized by the following procedure;  $\text{Na}_2\text{CO}_3$ , anatase-type  $\text{TiO}_2$  and  $\text{Rh}_2\text{O}_3$  were mixed and grinded in a mortar. The mixture was calcined at 1173 K for 24 h in air. This operation was repeated again after grinding. The amount of Rh (z) added to the Ti sites was set from 0 to 10%.

### *Preparation of the nanosheet colloidal suspension*

The colloidal suspension of  $\text{Ti}_3\text{NS}:\text{Rh}_x$  was prepared according to a modified form of the method described by Miyamoto *et al.*<sup>23</sup> 0.3 g of  $\text{Na}_2\text{Ti}_{3-x}\text{Rh}_x\text{O}_7$  powder was dispersed in 30  $\text{cm}^3$  of hydrochloric acid (1  $\text{mol}/\text{dm}^3$ ) for exchanging the counter cation from  $\text{Na}^+$  to  $\text{H}^+$ . Subsequently, it was shaken for 3 days at room temperature. The hydrochloric acid was replaced every day to allow the protonation reaction to proceed efficiently. The filtrated  $\text{H}_2\text{Ti}_{3-x}\text{Rh}_x\text{O}_7$  was washed with high purity water to remove any remaining hydrochloric acid, and was dried under a reduced pressure condition at room temperature overnight. The collected  $\text{H}_2\text{Ti}_{3-x}\text{Rh}_x\text{O}_7$  was neutralized by methylamine aqueous solution at 333 K for 6 days to yield  $(\text{CH}_3\text{NH}_3)_2\text{Ti}_{3-x}\text{Rh}_x\text{O}_7$  powder. Subsequently,  $(\text{CH}_3\text{NH}_3)_2\text{Ti}_{3-x}\text{Rh}_x\text{O}_7$  was dispersed in TMAOH solution ( $[\text{Ti}_{3-x}\text{Rh}_x\text{O}_7^{2-}]/[\text{TMAOH}] = 5$ ) by sonication for 5 days. Non-exfoliated  $\text{Ti}_3\text{NS}:\text{Rh}_x$  was removed by centrifugation (at 4000 rpm or 1150 G for 15 min, IEC61010-2-020, KUBOTA). The  $\text{Ti}_3\text{NS}:\text{Rh}_x$  colloidal suspension was obtained as the supernatant. The synthesis diagram and reaction pathway is shown in Figure 3.2.

### *Adsorption properties of $\text{Ti}_3\text{NS}:\text{Rh}_x$* <sup>24-26</sup>

To investigate the adsorption property of  $\text{Ti}_3\text{NS}:\text{Rh}_x$ , the adsorption experiment of MB and MO by  $\text{Ti}_3\text{NS}:\text{Rh}_x$  was carried out by the following procedure (Figure 3.3): (1) 0.01  $\text{cm}^3$  of the  $\text{Ti}_3\text{NS}:\text{Rh}_x$  ( $9.53 \times 10^{-2}$   $\text{mol}/\text{dm}^3$ , pH 11) was added to 10  $\text{cm}^3$  of the MB or MO aqueous solution ( $9.53 \times 10^{-8}$  -  $9.53 \times 10^{-5}$   $\text{mol}/\text{dm}^3$ , pH 11), and this mixture was stirred at room temperature for 24 h, away from light. The molar ratio of the MB or MO and  $\text{Ti}_3\text{NS}:\text{Rh}_x$  was varied from 0.001 to 1.0. (2) After stirring, the mixture was filtrated through a hydrophilic polyfluororesin membrane filter (pore size: 0.1  $\mu\text{m}$ ) to remove  $\text{Ti}_3\text{NS}:\text{Rh}_x$  from the suspension. (3) The amount of adsorbed MB or

MO by TiNS:Rh<sub>z</sub> was calculated from the absorbance of remained MB or MO in the filtrate at the peak wavelength of 663 nm. The extinction coefficient ( $\epsilon$ ) of the MB solution (pH 11) was  $5.2 \times 10^4 \text{ dm}^3/\text{mol}\cdot\text{cm}$  and MO solution was  $2.6 \times 10^4 \text{ dm}^3/\text{mol}\cdot\text{cm}$ .

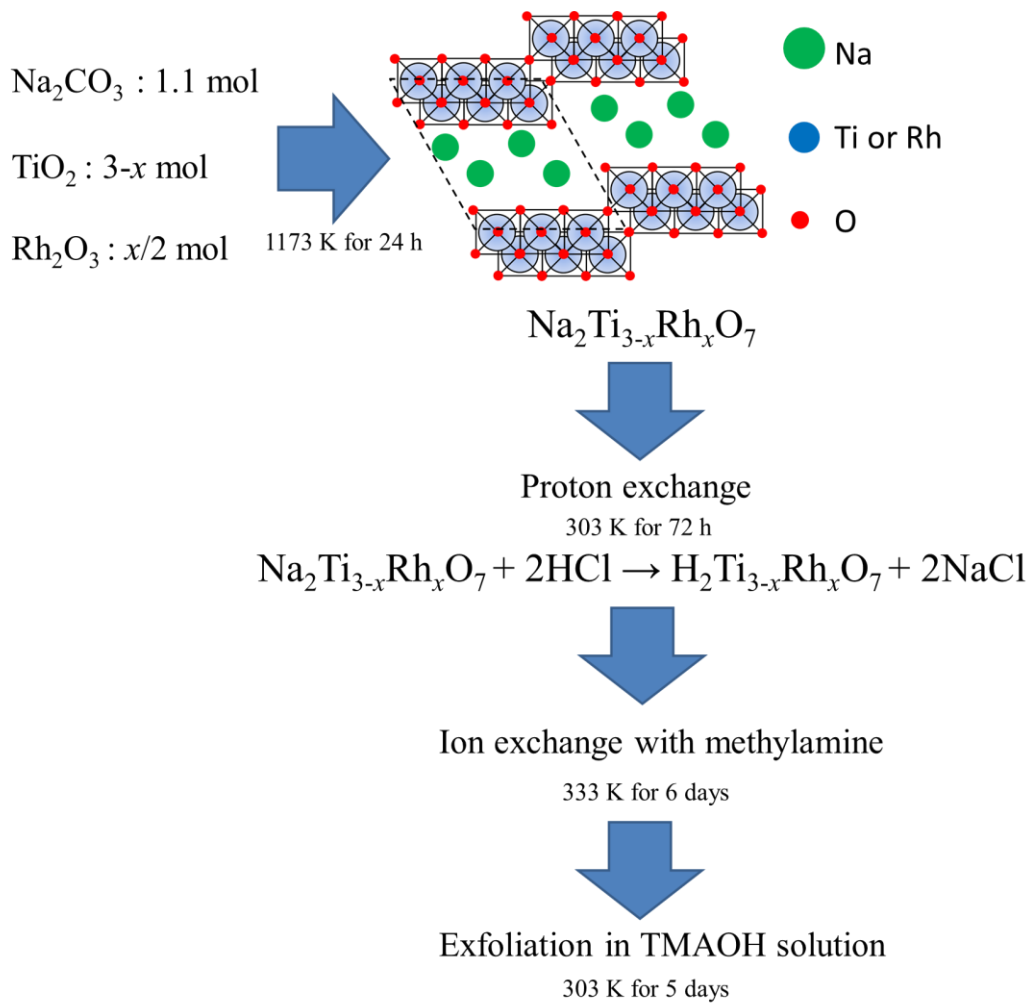


Figure 3.2 The flow chart of synthesis and preparation method for  $\text{Ti}_3\text{NS}:\text{Rh}_x$ <sup>4,5,22</sup>

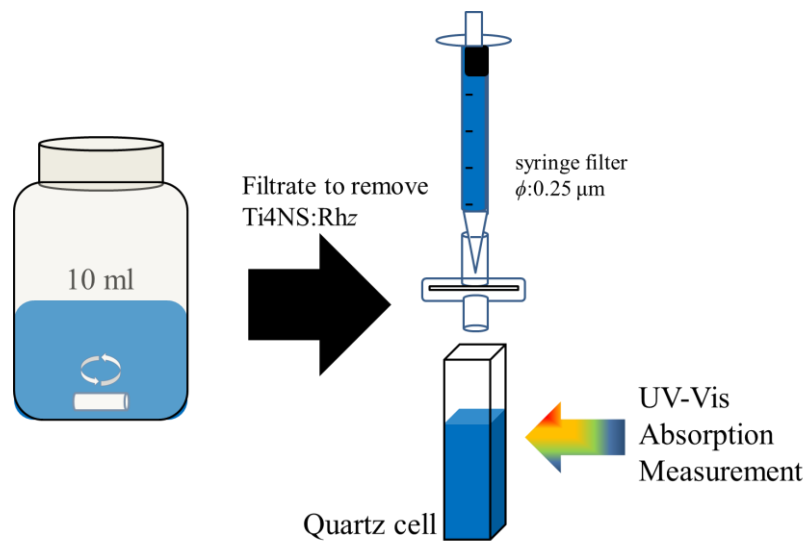


Figure 3.3 Schematic diagram of adsorption experiment.

### *Photodegradation of organic methylene blue and methyl orange dye<sup>37-31</sup>*

To characterize the photocatalytic activity of Ti3NS:Rh<sub>x</sub> in aqueous media, the solution of Ti3NS:Rh<sub>x</sub> and MB or MO was irradiated with UV light according to the following procedure: (1) the MB or MO solution ( $4.7 \times 10^{-6}$  mol) was mixed with Ti3NS:Rh<sub>x</sub> ( $4.7 \times 10^{-6}$  mol) to reach a total volume of 10 cm<sup>3</sup> (pH 11), and stirred in the dark until the adsorption was at equilibrium. (2) UV light of 254 nm (0.88 mW/cm<sup>2</sup>) from a Xe lamp (MAX-301, Asahi Spectra Co.) was directed towards the mixture through a band pass filter, for a given time at room temperature. The irradiation area was confined to a square of 25 cm<sup>2</sup>. (3) After the UV irradiation, the mixture was filtrated by the hydrophilic polyfluororesin membrane filter (pore size: 0.1 μm) to remove Ti3NS:Rh<sub>x</sub> from the suspension. (4) The amount of remained MB by Ti3NS:Rh<sub>x</sub> was calculated from the absorbance of MB in the filtrate at the peak wavelength of 663 nm, and MO at peak wavelength of 464 nm.

### *Characterization*

To analyze crystal structure of all materials, the powder X-ray diffraction (XRD) analysis was carried out by X-ray diffractometer (RIGAKU, MiniFlex II). Absorption spectra of various samples was measured by UV-Vis spectrophotometer (V-670 UV-VIS-NIR spectrophotometer, JASCO). Absorption spectra of liquid samples was measured by transmission mode. Diffuse reflectance (DR) spectra of solid sample was measured by UV-Vis spectrophotometer attached to an integrating sphere system (ISN-723, JASCO). Doped amount of Rh in Ti3NS:Rh<sub>x</sub> was estimated by ICP-AES apparatus (Optima2000DV, Perkinelmer). Scanning electron microscopy imaging was performed using JEOL-7001FA (JEOL Ltd.) operated at 12 kV.

### *Photocurrent measurement<sup>32-33</sup>*

According to the measurement setup reported by Usami *et al.* (Figure 3.4), photocurrent was measured by a three-electrode electrochemical analyzing system (Hokuto Denko, HSV-110) at a sweep rate of 10 mV·s<sup>-1</sup>. The Ti3NS:Rh<sub>x</sub> was cast on FTO glass and dried at 333 K overnight. The Ti3NS:Rh<sub>x</sub> film deposited on FTO glass acted as the working electrode, which was placed on a circle (9 mm in diameter) in a PTFE cell to adjust the electrode area to 0.636 cm<sup>2</sup>. An Ag/AgNO<sub>3</sub> reference electrode and Pt wire counter electrode were immersed in an acetonitrile solution of 0.1 mol/dm<sup>3</sup> tetraethylammonium perchlorate. A parallel beam of excitation light from a 150 W Xe lamp (Hamamatsu Photonics, L2195) was focused on the semiconductor layer of the FTO electrode through a light chopper (NF Electric Instruments, 5584A). The modulated photocurrent at the applied potential was amplified using a digital lock-in-amplifier (NF Electric Instruments, LI5640) and transferred to a PC to be plotted against the applied potential.

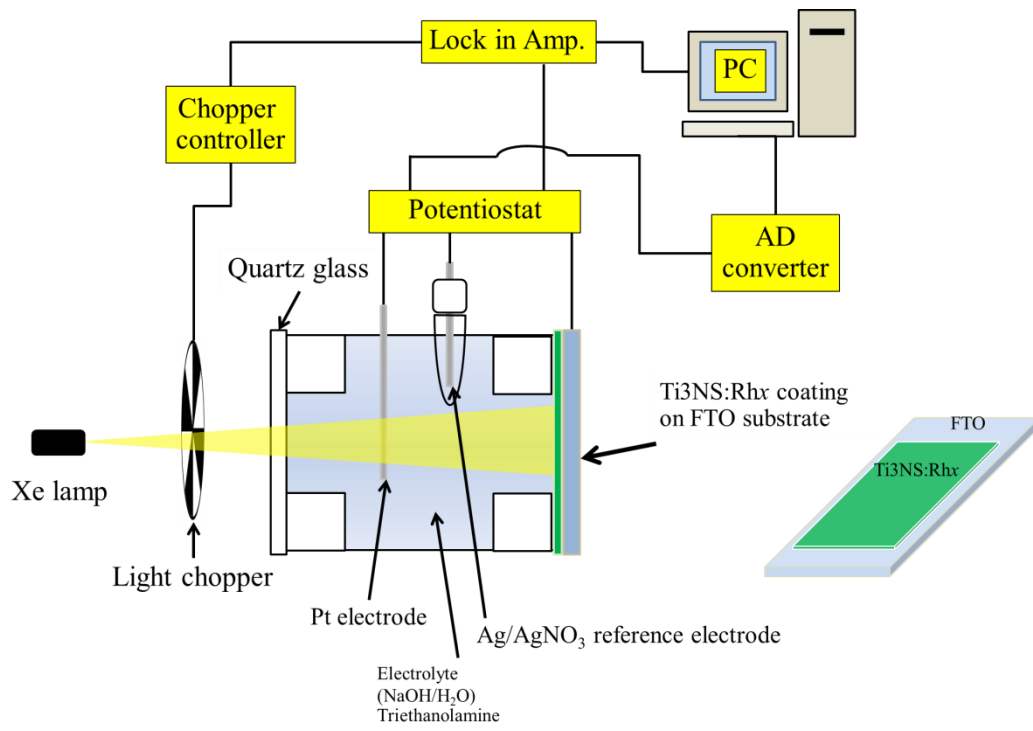


Figure 3.4 Schematic diagram shows the Photocurrent measurement setting reported by Usami *et al.*<sup>32-33</sup>

### 3.3 Results and discussion

#### *Characterization of Rh doped titanate nanosheet*

The obtained powder of Rh-doped sodium titanate,  $\text{Na}_2\text{Ti}_{3-x}\text{Rh}_x\text{O}_7$  ( $x$  is doping amount (mol/mol)), is shown in Figure 3.5. The powder color changed from white to yellow brown depended on amount of added Rh. The XRD patterns of all samples shown in Figure 3.6. All samples showed diffraction peaks originated from  $\text{Na}_2\text{Ti}_3\text{O}_7$  crystal. However, some of diffraction peaks from impurities could be found also in XRD patterns of Rh-doped samples as shown in a red strip in Figure 3.6. Thus, These these impurities was induced by adding Rh. This might cause the formation of another crystalline of Na and Ti. The reason is that Na/Ti ratio was decreased by the dope of Rh atom. However, SEM imaging of  $\text{Na}_2\text{Ti}_{3-x}\text{Rh}_x\text{O}_7$  with no Rh added and 10% added did not allow their microstructural differences to be observed as shown in Figure 3.7.

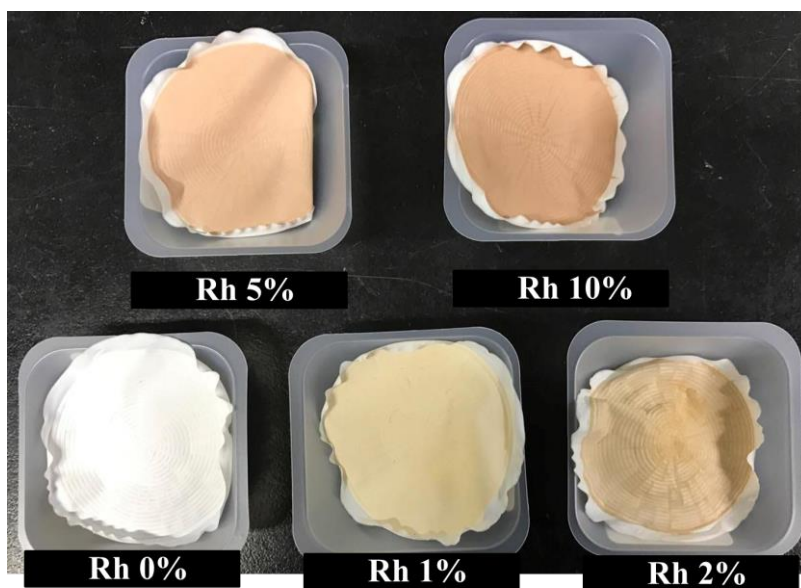


Figure 3.5 Picture of synthesized  $\text{Na}_2\text{Ti}_3\text{O}_7$  and Rh doped  $\text{Na}_2\text{Ti}_3\text{O}_7$  with varied added amount.

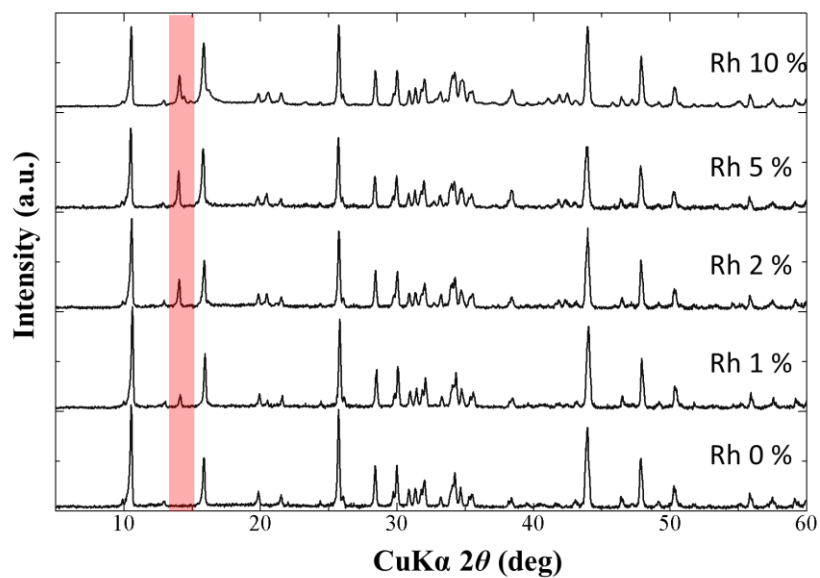


Figure 3.6 XRD pattern of synthesized  $\text{Na}_2\text{Ti}_3\text{O}_7$  and Rh doped  $\text{Na}_2\text{Ti}_3\text{O}_7$  with varied added amount. The red strip displayed an impurities peak.

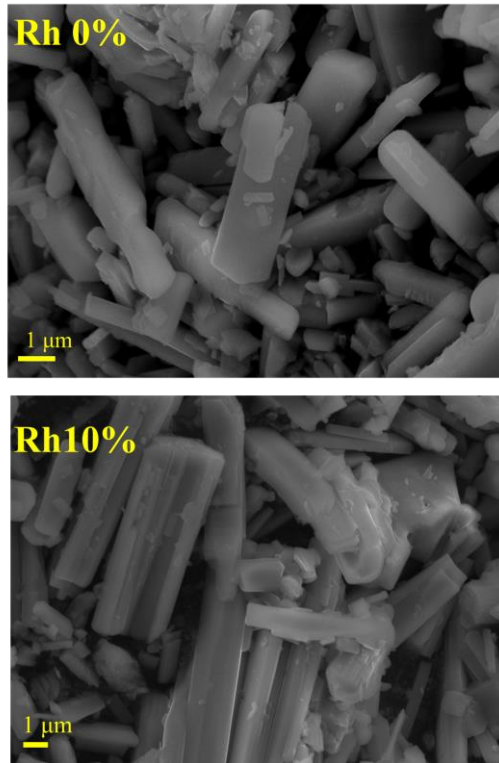


Figure 3.7 SEM image of  $\text{Na}_2\text{Ti}_3\text{O}_7$  and Rh 10% added  $\text{Na}_2\text{Ti}_3\text{O}_7$

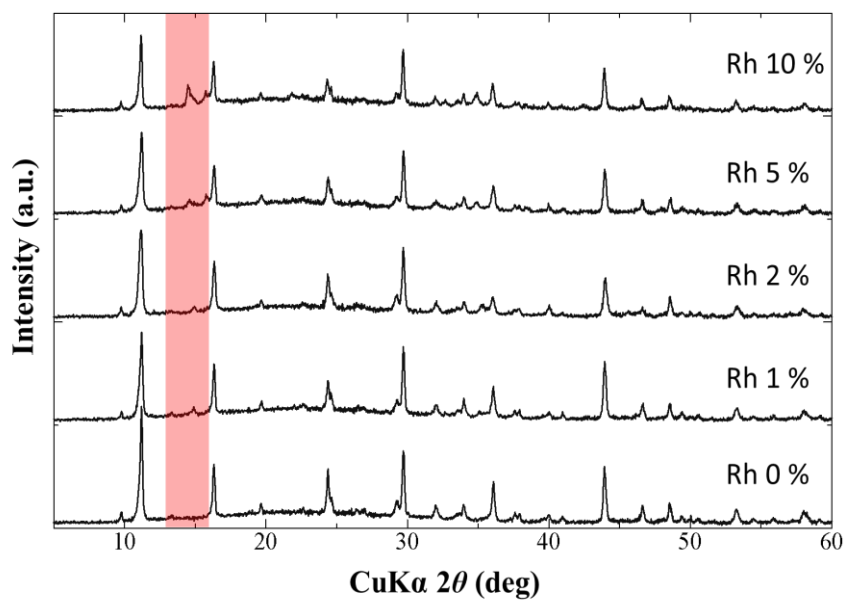


Figure 3.8 XRD pattern of synthesized  $\text{H}_2\text{Ti}_3\text{O}_7$  and Rh doped  $\text{H}_2\text{Ti}_3\text{O}_7$  with varied added amount. The red strip displayed an impurities peak.

In Figure 3.8, XRD patterns of powdery samples obtained by protonation process were shown. All samples showed the diffraction peaks from protonated titanate,  $\text{H}_2\text{Ti}_{3-x}\text{Rh}_x\text{O}_7$ , and  $\text{Na}_2\text{Ti}_{3-x}\text{Rh}_x\text{O}_7$  was found to be protonated by acid treatment as same as non-doped  $\text{Na}_2\text{Ti}_3\text{O}_7$ . Meanwhile, the diffraction peaks of impurity could not observed for any changes. This result indicated that the impurity cannot be protonated by the acid treatment. Thus, it can be easily predicted that these impurities will be removed by exfoliation process.

The obtained  $\text{Ti}_3\text{NS}:\text{Rh}_x$  colloidal suspension were shown in Figure 3.9. The non-doped  $\text{Ti}_3\text{NS}$  colloidal suspension was white and the color change was occurred in the colloidal suspension doped with Rh. The color alteration was changed from white to light brown as the doping amount of Rh increased. The Tyndall effect could be observed after beaming a laser thru the  $\text{Ti}_3\text{NS}:\text{Rh}_x$  colloidal suspension (Figure 3.9 B). The XRD patterns of  $\text{Ti}_3\text{NS}:\text{Rh}_x$  cast film, which prepared by casting the  $\text{Ti}_3\text{NS}:\text{Rh}_x$  colloidal suspension on the quartz substrate and dried at room temperature under reduced pressure, are shown in Figure 3.10. In XRD patterns of all samples, only 00l diffraction peaks could be observed 001 around  $2\theta$  of  $4.5^\circ$ , 002 around  $2\theta$  of  $9.0^\circ$  and 003 around  $2\theta$  of  $13.5^\circ$ . There are also no diffraction peaks from any impurities as it was observed in case of  $\text{Na}_2\text{Ti}_{3-x}\text{Rh}_x\text{O}_7$  and  $\text{H}_2\text{Ti}_{3-x}\text{Rh}_x\text{O}_7$ .

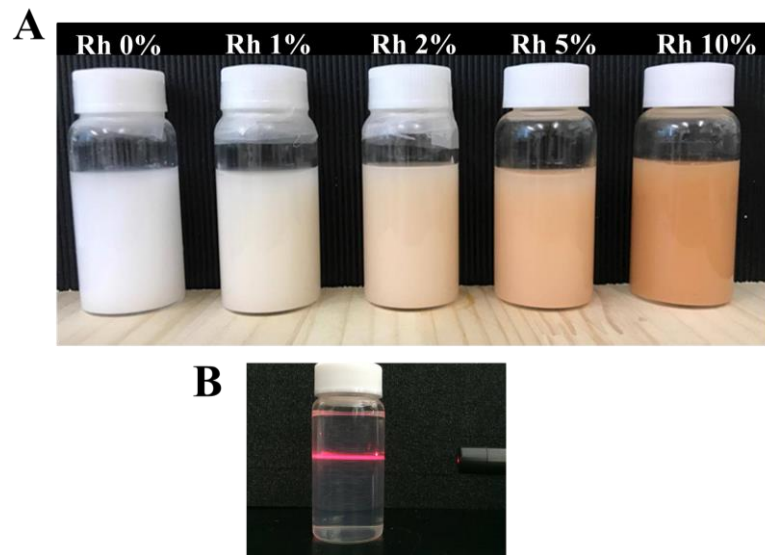


Figure 3.9 The photograph of A) Ti3NS:Rh<sub>x</sub> colloidal suspension with varied Rh added amount at concentration of 1 g/dm<sup>3</sup>, and B) the Tyndall effect after pass a laser thru the Ti3NS:Rh<sub>x</sub> colloidal suspension at concentration of 0.001 g/dm<sup>3</sup>.

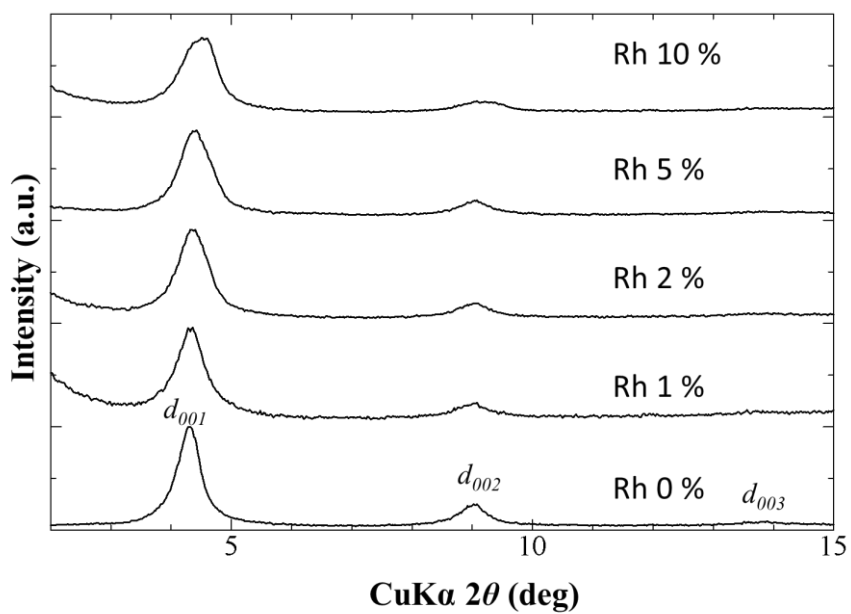


Figure 3.10 XRD patterns of Ti<sub>3</sub>NS:Rh<sub>x</sub> cast films prepared cast on quartz substrates.

From ICP-AES, the amount of Ti and Rh atom in Ti3NS:Rh<sub>x</sub> nanosheet was measured, and the chemical formula of Ti3NS:Rh<sub>x</sub> were also comprehended as written in Table 3.1. From this result, it showed that the Rh doped amount was lower than added amount. This was due to solid state reaction of Rh<sub>2</sub>O<sub>3</sub> melting point is about 1100 °C and the heating process was about 900 °C. As a result, Rh<sub>2</sub>O<sub>3</sub> was partially melted causing the doping amount lower than added amount. Moreover, the ionic radius of Rh<sup>3+</sup> or Rh<sup>4+</sup> is slightly larger than Ti<sup>4+</sup>. Subsequently, this is one of the reasons why the doping amount is lower than the added amount. Nevertheless, the doping amount is increased as the added amount is increased.

Figure 3.11 shows the AFM image and its cross-sectional profiles of Ti3NS:Rh0 on Si substrate. The sample was prepared by dipping a Si substrate in the Ti3NS:Rh0 colloidal solution (pH 11) overnight, then washed and dried under vacuum condition. A-B showed the cross section of Ti3NS 1 sheet. The thickness value of 1 sheet (~1.5-1.6 nm) is 2 times larger than its theoretical value (~0.7 nm) because of TMA cation on Ti3NS surface. C-D showed cross section of overlapped 2 sheets. The thickness value of overlapped 2 sheets is about 2 times larger than 1 sheet.<sup>34-35</sup> Thus, this results indicate that the exfoliation process was successful, and Ti3NS:Rh<sub>x</sub> nanosheet can be succeeded by the present experiment procedures.

Table 3.1 The chemical formula of Ti<sub>3</sub>NS:Rh<sub>x</sub> at each Rh added amount.

Rh added amount (% Ti atom)	Chemical formula Ti <sub>3-x</sub> Rh <sub>x</sub> O <sub>7</sub>
0	[Ti <sub>3.00</sub> O <sub>7</sub> ] <sup>2-</sup>
1	[Ti <sub>2.999</sub> Rh <sub>0.001</sub> O <sub>7</sub> ] <sup>(2+δ)-</sup>
2	[Ti <sub>2.992</sub> Rh <sub>0.008</sub> O <sub>7</sub> ] <sup>(2+δ)-</sup>
5	[Ti <sub>2.970</sub> Rh <sub>0.030</sub> O <sub>7</sub> ] <sup>(2+δ)-</sup>
10	[Ti <sub>2.952</sub> Rh <sub>0.048</sub> O <sub>7</sub> ] <sup>(2+δ)-</sup>

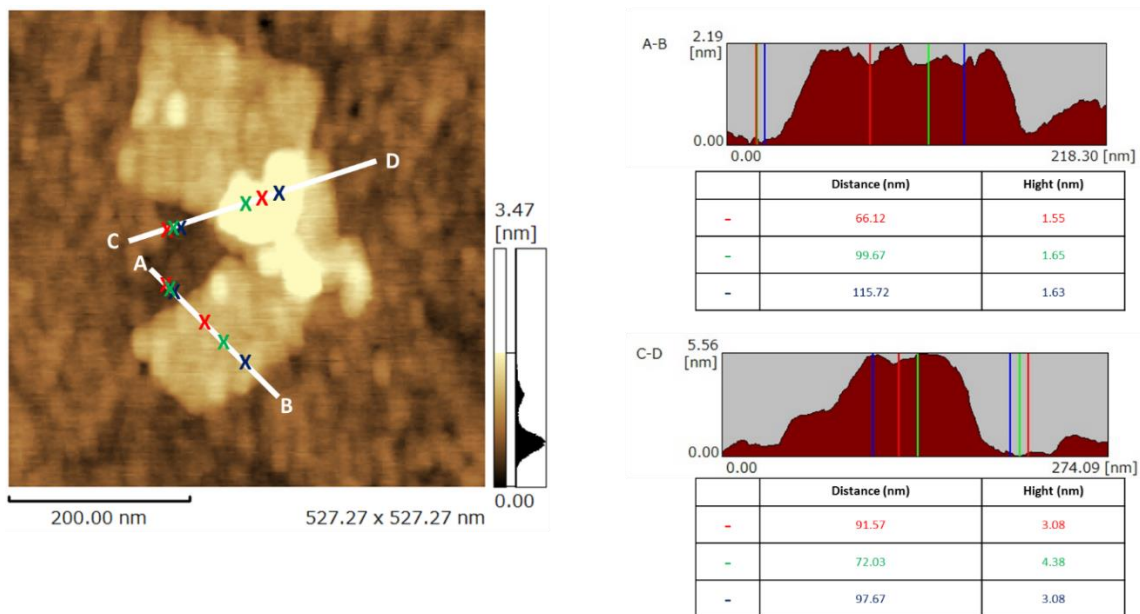


Figure 3.11. AFM image of Ti<sub>3</sub>NS:Rh<sub>0</sub> on Si substrate, and the cross section.

### *Optical and electrical properties of Ti<sub>3</sub>NS:Rh<sub>x</sub> and the effect of Rh*

Figure 3.12 shows the diffuse reflectance spectra of H<sub>2</sub>Ti<sub>3-x</sub>Rh<sub>x</sub>O<sub>7</sub> in term of Kubelka-Munk function. The adsorption of H<sub>2</sub>Ti<sub>3</sub>O<sub>7</sub> ranged from 380 nm to 350 nm and the highest peak was detected at about 350 nm. Hence, H<sub>2</sub>Ti<sub>3</sub>O<sub>7</sub> can absorb only UV light. On the other hand, the adsorption spectra of H<sub>2</sub>Ti<sub>3-x</sub>Rh<sub>x</sub>O<sub>7</sub> showed new adsorption bands from 380 to 600 nm. Likewise, this new adsorption was increased due to the Rh-doped amount. However, the adsorption band does not come from Rh<sub>2</sub>O<sub>3</sub> because the adsorption band of Rh<sub>2</sub>O<sub>3</sub> is clearly distinguished from the new adsorption band of the H<sub>2</sub>Ti<sub>3-x</sub>Rh<sub>x</sub>O<sub>7</sub>. Consequently, this suggests that the new adsorption band was introduced by the Rh-doping effect. According to A. Kudo et al., the new adsorption was a result of Rh<sup>3+</sup> and Rh<sup>4+</sup> doping effect.<sup>36-38</sup> The adsorption band originated from 380 to 500 nm caused by Rh<sup>3+</sup>. While the adsorption band about 500 to 600 nm was caused by Rh<sup>4+</sup>. It was concluded that the new absorption bands were composed by the summation of the absorption bands of Rh<sup>3+</sup> and Rh<sup>4+</sup>. However, the amount of Rh<sup>3+</sup> and Rh<sup>4+</sup> in each sample cannot be determined.

Figure 3.13 showed adsorption of each colloidal suspension in term of Kubelka-Munk function. The adsorption edge was shifted to shorter wavelengths as a result of exfoliation, which was ascribed to quantum size effects. This indicates that the compound structure was changed from bulk molecule to nanosheet.

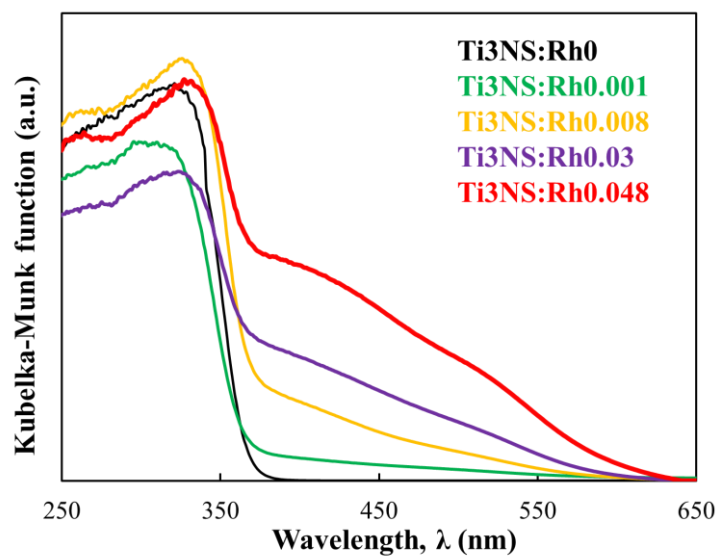


Figure 3.12 The diffuse reflectance spectra of  $H_2Ti_{3-x}Rh_xO_7$  in term of Kubelka-Munk function.

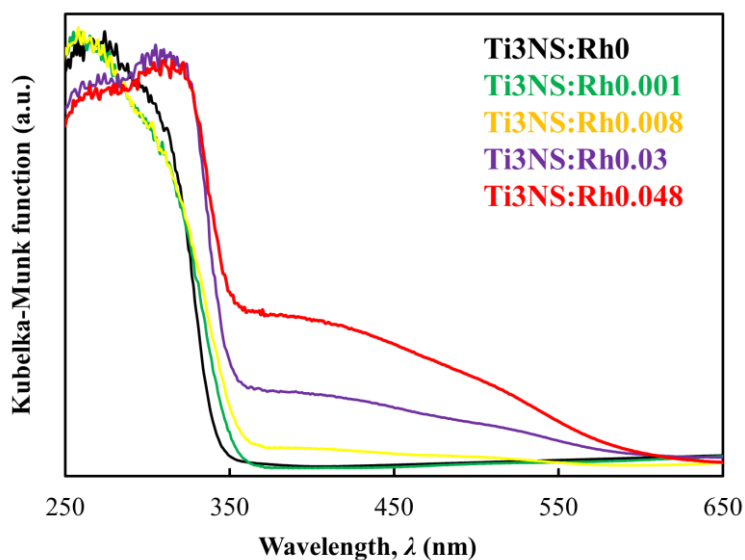


Figure 3.13 The diffuse reflectance spectra in term of Kubelka-Munk function of all  $Ti_3NS:Rh_x$  colloidal suspension

**Table 3.2.** The optical band gap ( $E_g$ ) of all prepared TiNS:Rh $x$  samples.

Sample Name	Energy band gap, $E_g$ (eV)
Ti3NS:Rh0	3.61
Ti3NS:Rh0.001	3.47
Ti3NS:Rh0.008	3.44
Ti3NS:Rh0.030	3.39
Ti3NS:Rh0.048	3.32

In Table 3.2, the optical band gap ( $E_g$ ) energies of the samples were determined by extrapolating the rising part of the onset of the absorption edge to the  $x$ -axis ( $\lambda$ , nm). The values of  $\lambda$  was used in the Planck's Einstein equation to calculate the band gap,  $E_g = hc/\lambda$ , where  $E_g$  is band gap energy in eV,  $h$  is Planck's constant in eV. s,  $c$  is the speed of light in m/s, and  $\lambda$  is the absorption wavelength in nm.<sup>39</sup> The calculated band gap energy values for Ti3NS:Rh $x$  are shown in Table 3.2. The decreased band gap energy values of rhodium-doped Ti3NS designated the formation of new energy levels within the Ti3NS band gap and resulted in redshift of the absorption edge. This shift can be attributed to the incorporation of Rh 4d levels into the Ti<sub>3</sub>O<sub>7</sub> crystal structure just below the conduction band of Ti<sub>3</sub>O<sub>7</sub> and thereby reducing the effective band gap.

#### *The energy band structure of Ti3NS:Rh $x$*

From the previous result of photo-absorption of Ti3NS:Rh $x$ , the energy band gaps of Ti3NS:Rh $x$  have been estimated. However, only the energy band gap cannot estimate another parameter in energy band structure such as conduction band level and valence band level. These two parameters are important for understanding the photocatalytic reaction in predicting reaction possibility. For example, a photocatalyst is used to oxidize organic compounds; the conduction band level of photocatalyst has to be higher than the reduction potential of the targeted. In contrast, reducing organic compounds require the valence band level of photocatalyst to be lower than the oxidation potential of the targeted. Hence, if these two parameters are known, it is possible to predict the reaction possibility.

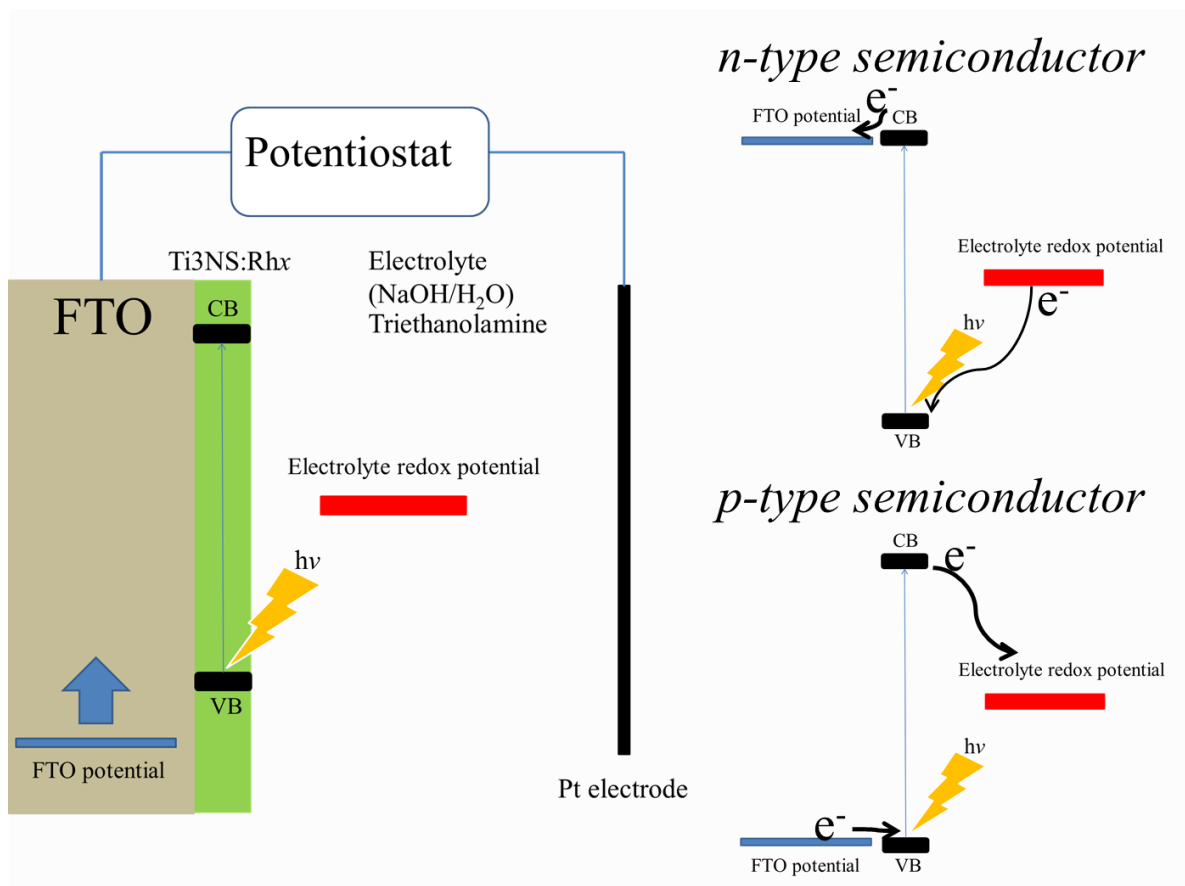
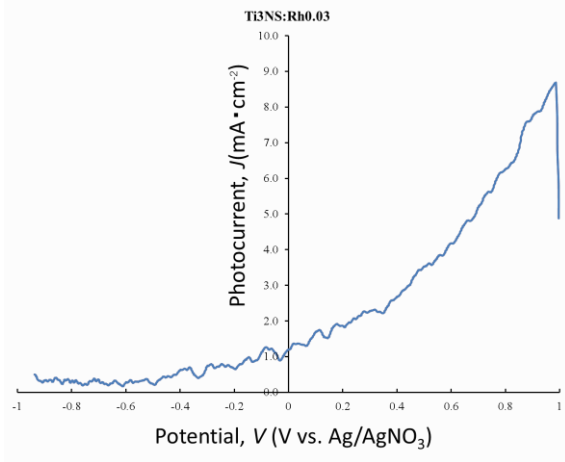
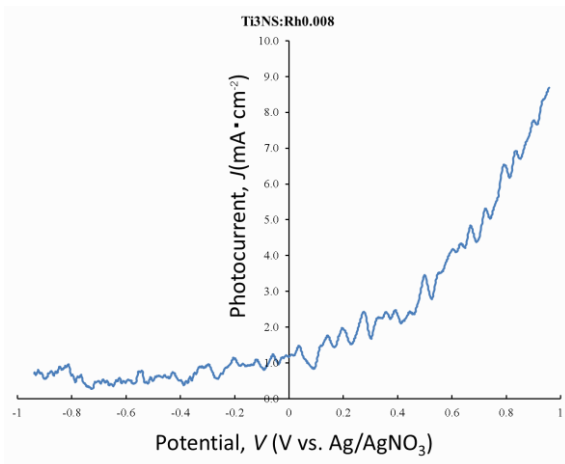
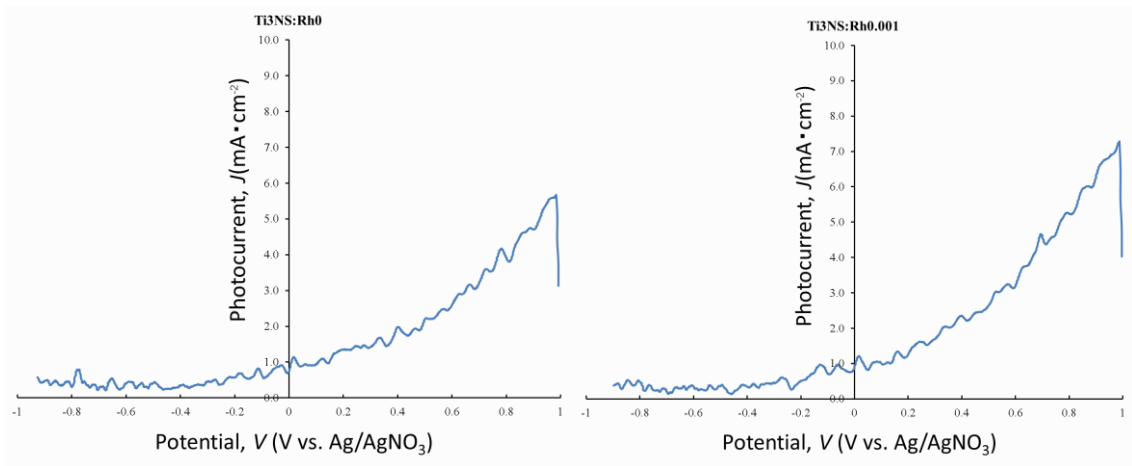


Figure 3.14 The schematic diagram of photocurrent measurement.



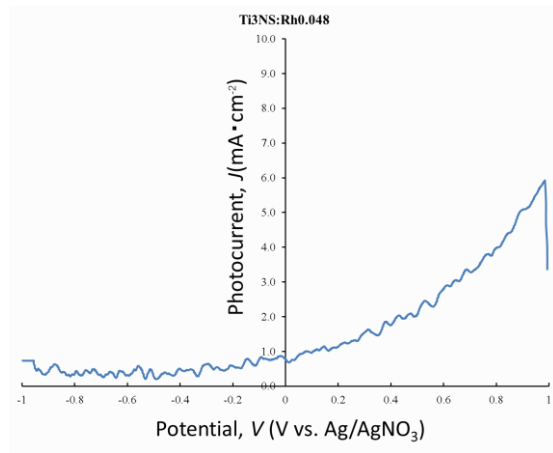


Figure 3.15 The Photocurrent density of Ti<sub>3</sub>NS:Rh<sub>x</sub> on FTO substrate under light irradiation.

Table 3.3 The electronic band structure of Ti3NS:Rh $x$  shown as a conduction band level ( $E_{cb}$ ), valence band level ( $E_{vb}$ ) and energy band gap( $E_g$ )

<b>Sample</b>	<b>Energy band gap, <math>E_g</math> (eV)</b>	<b>Conduction band level, <math>E_{cb}</math> (V vs. NHE)</b>	<b>Valence band level, <math>E_{vb} = E_{cb} + E_g</math> (V vs. NHE)</b>
Ti3NS:Rh0	3.61	0.0	3.61
Ti3NS:Rh0.001	3.47	0.0	3.47
Ti3NS:Rh0.008	3.44	0.0	3.44
Ti3NS:Rh0.030	3.39	0.0	3.39
Ti3NS:Rh0.048	3.32	0.0	3.32

Figure 3.14 showed the schematic of photocurrent measurement of Ti<sub>3</sub>NS:Rh<sub>x</sub>. The applied potential on FTO substrate was adjusted to find the point that current start to flow. The results were plotted between photocurrent density,  $J$  (mA/cm<sup>2</sup>) generated by Ti<sub>3</sub>NS:Rh<sub>x</sub> with the applied electrical potential as shown in Figure 3.15. The Ag/AgNO<sub>3</sub> was used as a reference electrode but the potential of conduction band level and valence band level were shown as a normal hydrogen electrode (NHE) at pH 7 which generally uses in photochemistry. As a result, all synthesized Ti<sub>3</sub>NS:Rh<sub>x</sub> exhibited the *n*-type semiconductor property which conduction band level can be detected at the point where the photocurrent started to flow. This was due to the applied potential of FTO is exactly equal to the conduction band potential of Ti<sub>3</sub>NS:Rh<sub>x</sub>. Consequently, the conduction band level can be predicted by reading the potential of FTO compared with reference electrode. All the data are shown in Table 3.3 as compared with NHE. Accordingly, the valence band can be calculated from the band gap and conduction level. Thus, all the valence band levels were obtained and are shown in Table 3.3.

Generally, the band structure of Ti<sub>3</sub>NS is composed of valence band of O 2*p* and conduction band of Ti 3*d*. Ti<sub>3</sub>NS:Rh<sub>0</sub> is shown in the table 3.3. However, Ti<sub>3</sub>NS:Rh<sub>x</sub> showed no difference in the conduction band level indicating that the conduction band level of all samples is still Ti 3*d*. Moreover, the energy band gap was reduced in Ti<sub>3</sub>NS:Rh<sub>x</sub> where *x* is not 0 indicating that the valence band level was not designated only O 2*p* but a combination of O 2*p* and Rh 4*d* as shown in figure 3.16.

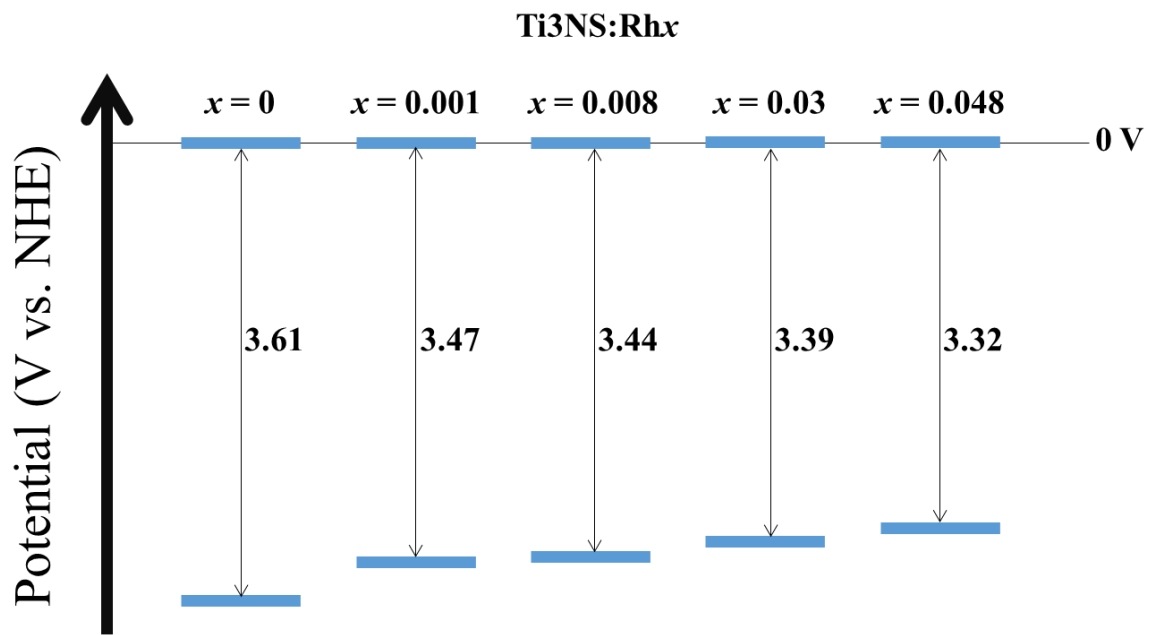


Figure 3.16 The potential diagram shows the energy band structure of Ti<sub>3</sub>NS:Rh<sub>x</sub>. Ti also shows that Rh doping and doped amount affects a valence band potential of Ti<sub>3</sub>NS.

### *Adsorption capacity for cationic methylene blue dye*

Figure 3.17 shows the adsorption kinetic of MB by Ti3NS:Rh $x$ . The graph was plotted between the molar amount of adsorbed MB per [Ti $_{3-x}$ Rh $_x$ O $_7^{2-}$ ] unit,  $C^{abs}$  (mol/mol) against adsorption time,  $t$ . The reaction reached the equilibrium point within 30 minutes.

The adsorption of MB by Ti3NS:Rh $x$  was evaluated by plotting  $C^{abs}$  against the molar amount of added MB per [Ti $_{3-x}$ Rh $_x$ O $_7^{2-}$ ] unit,  $C^0$  (mol/mol), as shown in Figure 3.18. The value of  $C^{abs}$  increased along with an increase in the  $C^0$  value. Therefore, the amount of adsorbed MB at saturation point could be calculated, and this is shown in Table 3.4. The adsorbed amount was much lower than the formal anionic charge of Ti3NS:Rh $x$  (2 mol/mol) in all cases because of the competitive adsorption of MB and TMAOH. Table 3.4 also shows the amount of adsorbed MB slightly decreased with an increase in Rh doping. This can be explained by the anionic charge of Ti3NS:Rh $x$ . In the case of Ti3NS:Rh $x$  ( $x > 0$ ), the anionic charge altered because the ionic state of Rh was Rh $^{3+}$  or Rh $^{4+}$ . This led to an increase in the anionic charge of Ti3NS:Rh $x$ . However, the result did not affect the MB adsorption because it strongly interacted with the TMA cation. Therefore, the adsorption of MB decreased when Rh incorporated into the Ti sites.

The shape of the adsorption isothermal curve was different for each sample (Figure 3.18). The  $C^{abs}$  value of the Ti3NS:Rh0 and Ti3NS:Rh0.001 linearly increased with an increase in the  $C^0$  value. The adsorption isothermal curve of Ti3NS:Rh0.001 behaved similarly to Ti3NS:Rh0 but the  $C^{abs}$  value of Ti3NS:Rh0.008, Ti3NS:Rh0.03 and Ti3NS:Rh0.048 logarithmically increased. Thus, these results suggest that the surface properties of Ti3NS varied with Rh doping into the Ti sites.

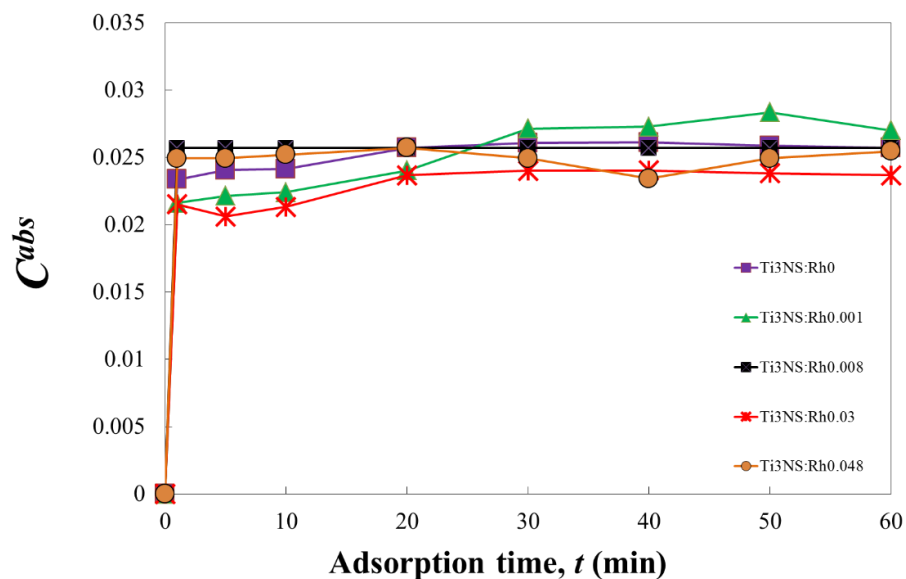


Figure 3.17 The time dependent adsorption activity of Ti3NS:Rh<sub>x</sub> for MB dyes. The initial Ti3NS/MB ratio was set as 1 mol/mol.

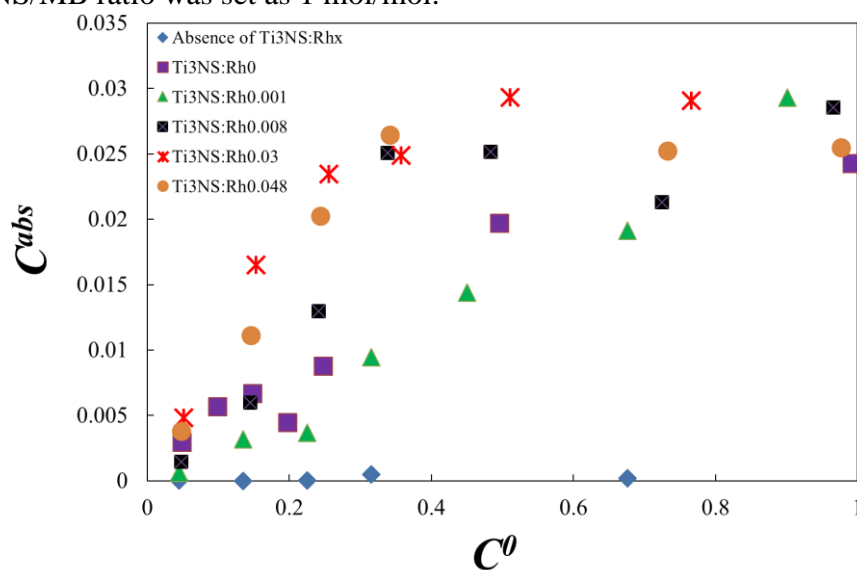


Figure 3.18 The adsorption isothermal curves of MB by Ti3NS:Rh<sub>x</sub>.

Table 3.4 The saturated adsorption amount of MB by Ti3NS:Rh<sub>x</sub> at equilibrium.

<b>Sample</b>	<b>Saturated amount of absorbed MB per molar amount of Ti3NS:Rh<sub>x</sub> at equilibrium (mg/g)</b>
Ti3NS:Rh0	37 ± 3
Ti3NS:Rh0.001	36 ± 3
Ti3NS:Rh0.008	35 ± 3
Ti3NS:Rh0.030	31 ± 3
Ti3NS:Rh0.048	29 ± 3

### *Adsorption capacity for anionic methyl orange dye*

The adsorption capacity of Ti3NS:Rh $x$  for MO was also evaluated as same as adsorption capacity for MB. The plot between  $C^{abs}$  against  $C^0$  is shown in Figure 3.19. As a result, it could not observe an adsorption of MO. This indicated that the MO cannot be adsorbed by Ti3NS:Rh $x$ . The reason for this phenomena is clearly simple as both of MO and Ti3NS:Rh $x$  are anionic molecules. Due to the electrostatic reaction between MO and Ti3NS:Rh $x$ , both of them should repulse each other. Moreover, it was previously explained that the interacted between Ti3NS:Rh $x$  and TMA cation is very strong. Thus, the Ti3NS:Rh $x$  do not adsorb MO and also have no adsorption capacity for MO.

From the result of adsorption activity of Ti3NS:Rh $x$  for MB and MO dye, it exhibited that the Ti3NS:Rh $x$  selectively adsorbed only the cationic MB dye. However, the adsorption capacity of the cationic dye on Ti3NS:Rh $x$  is low. The reason is due to the strong interaction between Ti3NS:Rh $x$  and TMA<sup>+</sup> which does not allowed other cation to be exchanged.

### *Photodegradation of MB dye*

The degradation of MB by UV light irradiation was observed with the changing of UV-visible absorption spectra. Figure 3.20 and Figure 3.21 show the UV-visible absorption spectra of filtrated MB solution from mixed solution between Ti3NS:Rh0 and Ti3NS:Rh0.0048, respectively, after irradiated by UV light at 254 nm with different irradiation times. The peak around 663 nm originated from MB was gradually decreased. This tendency could be observed for all of Ti3NS:Rh $x$  which denoted that the MB was degraded by UV light irradiation. Hence, It was found that the Ti3NS:Rh $x$  can act as a photocatalyst for MB degradation.

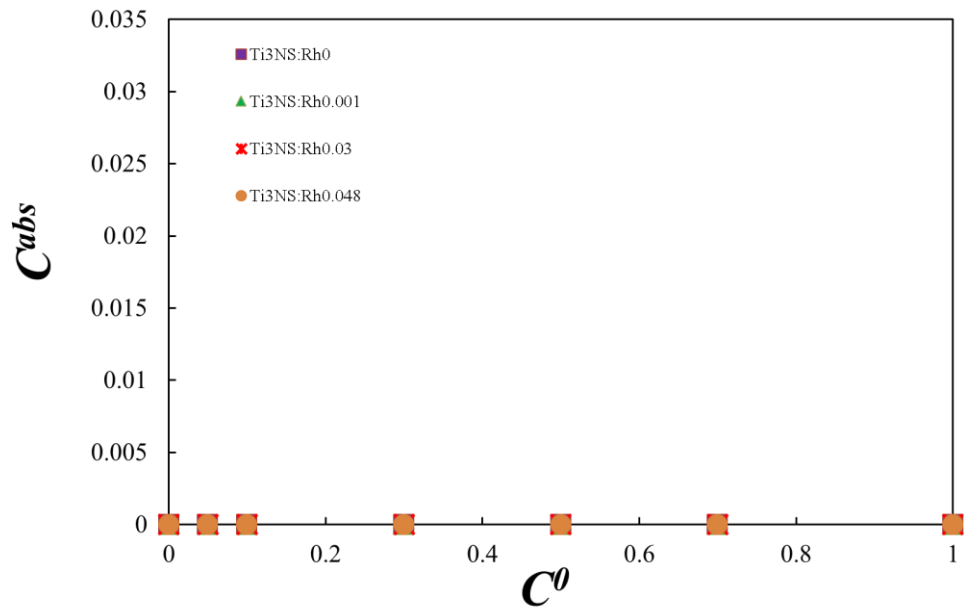


Figure 3.19 The adsorption isothermal curves of MO by Ti3NS:Rh<sub>x</sub>.

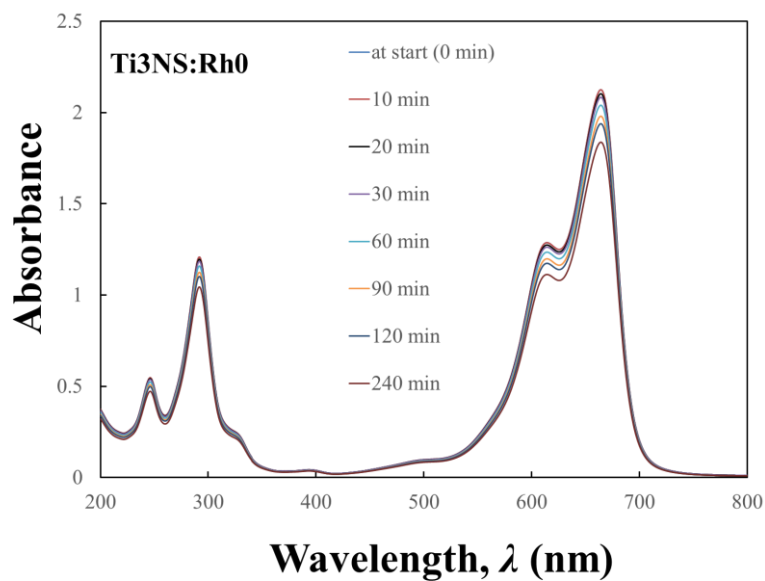


Figure 3.20 UV-vis absorption spectral changes of MB solution under UV light ( $\lambda$  is 254 nm) irradiation in presence of Ti3NS:Rh0.

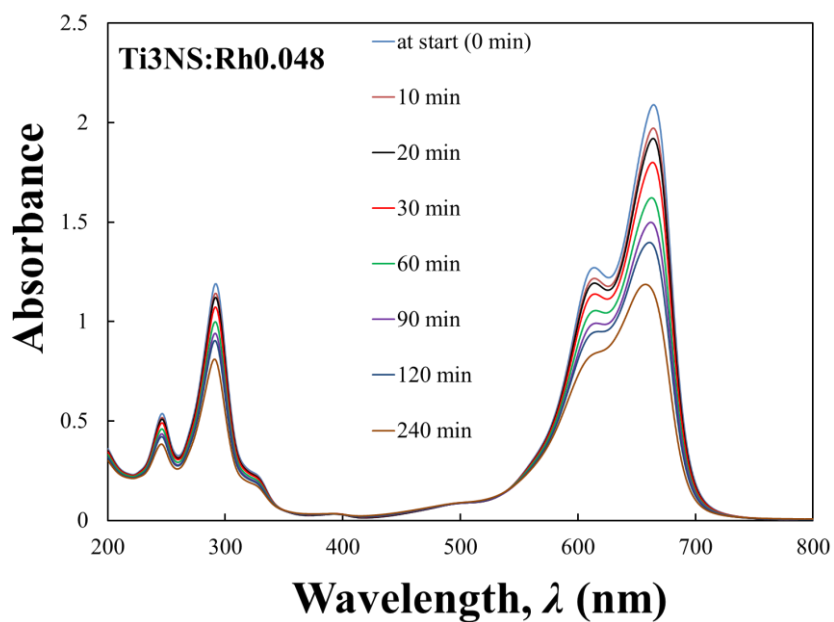


Figure 3.21 UV-vis absorption spectral changes of MB solution under UV light ( $\lambda$  is 254 nm) irradiation in presence of Ti3NS:Rh0.048.

Comparison of photocatalytic activity of each Ti3NS:Rh $x$  series, the absorbance ratio values at 663 nm ( $Abs_t/Abs_0$ ; where  $Abs_t$  is an absorbance at each interval and  $Abs_0$  is the initial absorbance or absorbance at  $t = 0$ ) are plotted against the irradiation time in Figure 3.22. All Ti3NS:Rh $x$  samples photocatalytically degraded MB. However, the duration of the reaction were varied. Ti3NS:Rh0 and Ti3NS:Rh0.001 showed almost the same photodegradation ratio curve, while Ti3NS:Rh0.008, Ti3NS:Rh0.03, and Ti3NS:Rh0.048 showed a different result. This indicates that photocatalytic activity can be improved by Rh doping at the Ti sites of Ti3NS:Rh $x$ .

The quantum yield ( $\Phi_{deg}$ ) of the photodegradation of MB by Ti3NS:Rh $x$  at initial time was calculated by:

$$\Phi_{deg} = \frac{\text{number of degraded MB molecules}}{\text{number of incident photons}}$$

Table 3.5 shows the  $\Phi_{deg}$  value of each Ti3NS:Rh $x$  sample. Ti3NS:Rh0 and Ti3NS:Rh0.001 exhibit almost the same  $\Phi_{deg}$  value. In contrast, the  $\Phi_{deg}$  value of Ti3NS:Rh0.008, Ti3NS:Rh0.03, and Ti3NS:Rh0.048 are higher than that of Ti3NS:Rh0; thus,  $\Phi_{deg}$  increased with increasing Rh doping. A similar grouping between samples was observed in the adsorption study. Thus, it is evident that Rh doping modifies the surface properties of Ti3NS:Rh $x$ . However, the adsorption ability was not improved with an increase in Rh doping. Thus, the change in adsorption ability cannot explained the increasing of photocatalytic activity for MB degradation.

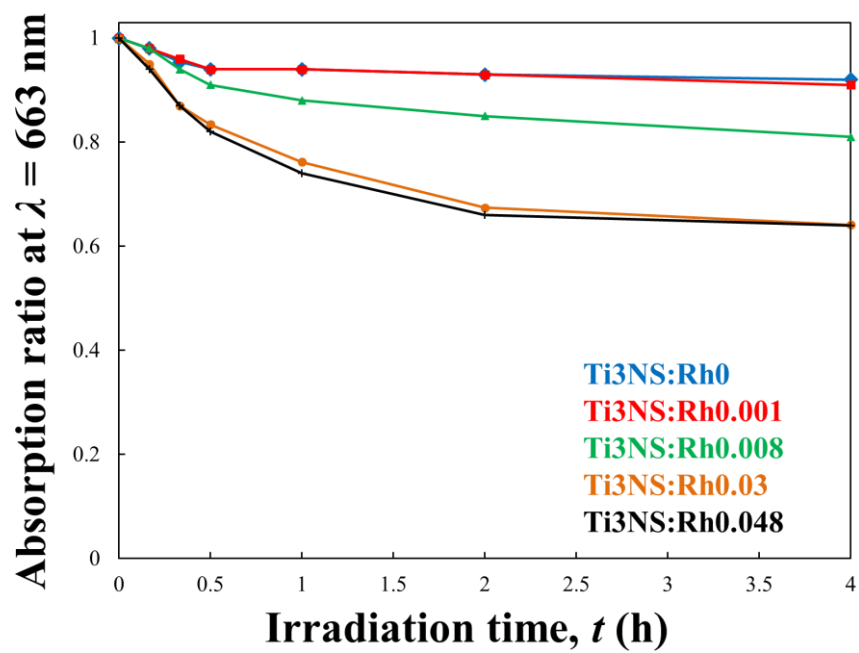


Figure 3.22 The photo-degradation ratio curves of the maximum absorption band of MB over the different Ti3NS:Rh $x$  (at 663 nm) after the UV light ( $\lambda$  is 254 nm) irradiation at each irradiation times.

Table 3.5 Quantum yield ( $\Phi_{\text{deg}}$ ) of MB photodegradation.

Sample	$\Phi_{\text{deg}}$ (%)
Ti3NS:Rh0	0.30
Ti3NS:Rh0.001	0.31
Ti3NS:Rh0.008	0.34
Ti3NS:Rh0.03	0.81
Ti3NS:Rh0.048	0.97

### *Photodegradation of MO dye*

The degradation of MO by UV light irradiation was also observed in a similar manner to MB dye by detecting the changing of MO solution UV-visible absorption spectra. Figure 3.23 shows the UV-visible absorption spectra of MO solution before and after the Ti3NS:Rh0-MO mixed solution was irradiated by UV light for 2 hours, and Figure 3.24 shows that of Ti3NS:Rh0.048-MO mixed solution. The degradation of MO was found due to the peak at about 464 nm which originated from decreasing MO. Figure 3.25 shows a plot between degradation amount of MO by Ti3NS:Rh0, Ti3NS:Rh0.03, Ti3NS:Rh0.048, and in case of no Ti3NS:Rh<sub>x</sub> against UV irradiation time. As a result, the degradation amount of MO shows almost same values for all samples at the same UV irradiation time. This value is not different from no Ti3NS:Rh<sub>x</sub>. This degradation of MO might be normally occurred when the MO solution was irradiated by UV light, or it might be found only the self-degradation of MO. This indicated that MO molecules were not degraded by the photocatalytic activity of Ti3NS:Rh<sub>x</sub>. The reason might be that Ti3NS:Rh<sub>x</sub> did not adsorb MO due to that both of them are in same anionic state.

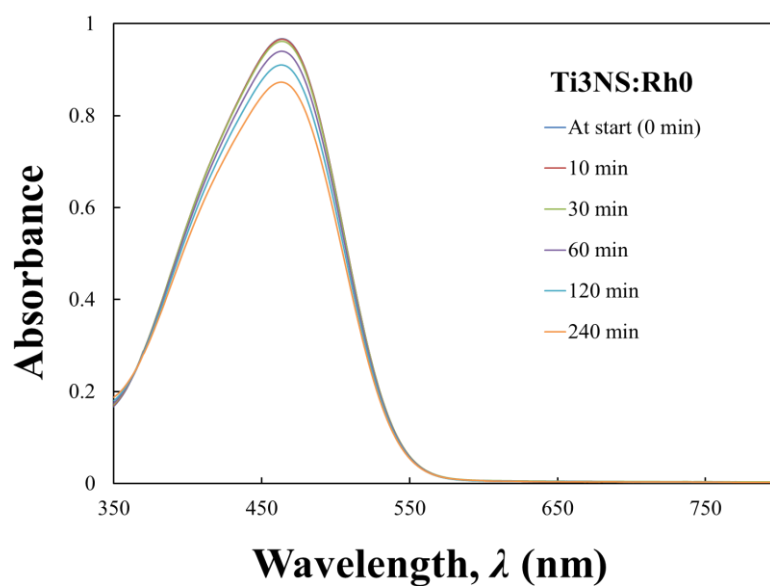


Figure 3.23 UV-vis absorption spectral changes of MO solution under UV light ( $\lambda$  is 254 nm) irradiation in presence of Ti3NS:Rh0.

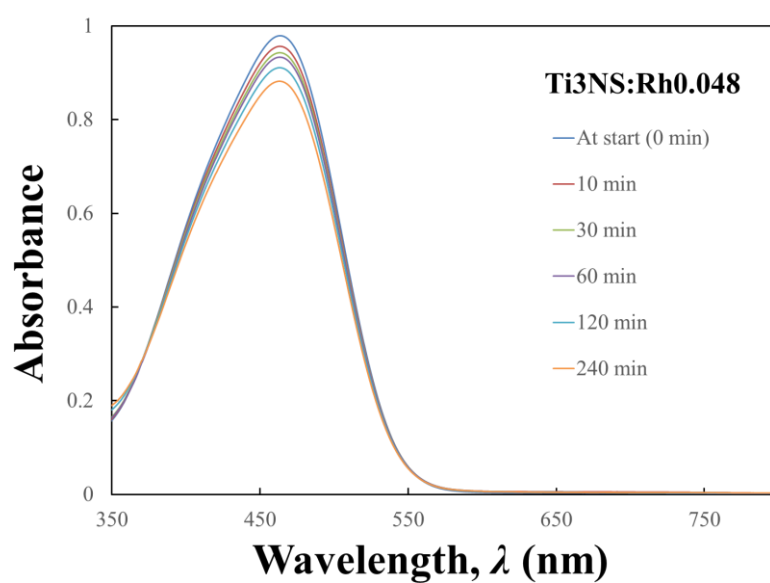


Figure 3.24 UV-vis absorption spectral changes of MO solution under UV light ( $\lambda$  is 254 nm) irradiation in presence of Ti3NS:Rh0.048.

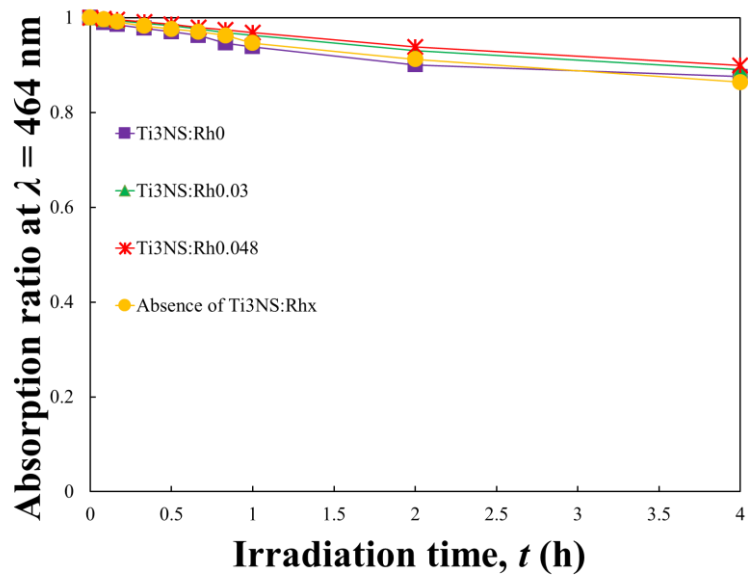


Figure 3.25 The photo-degradation ratio curves of the maximum absorption band of MO over the different Ti3NS:Rh $x$  (at 464 nm) after the UV light ( $\lambda$  is 254 nm) irradiation at each irradiation times.

### *Photocatalytic activity of Ti3NS:Rh<sub>x</sub>*

Generally, the photocatalytic degradation of organic molecule in solution can occur directly from photocatalyst material to organic molecule, or occur via the OH<sup>-</sup> radical or O<sub>2</sub> radical. In case of OH<sup>-</sup> radical or O<sub>2</sub> radical, the oxidation or reduction of water molecule and photo-induced electron or hole in photocatalyst material should be progressed to form OH<sup>-</sup> radical or O<sub>2</sub> radical.<sup>18,40-41</sup> While these radical contracts with organic molecules, the organic molecules will be degraded even when organic molecules do not exist on the surface of photocatalyst. On the other hand, the direct degradation of organic dye by photo-induced hole from photocatalyst material can be observed only on the surface of photocatalyst material. In the case of the photodegradation experiment for MO, slight photodegradation of MO could be observed under UV irradiation, although MO molecules were not absorbed on Ti3NS:Rh<sub>x</sub>. Thus, it can be explained that the photodegradation of MO was mainly caused by OH and O<sub>2</sub> radical species. In the case of MB, both adsorption and photodegradation of MB could be observed. Thus, MB was directly photodegraded by the photo-induced holes produced on the surface Ti3NS:Rh<sub>x</sub> under UV irradiation.

Moreover, Rh doping could improve the photocatalytic activity of Ti3NS:Rh<sub>x</sub>. The adsorption capacity of MB by Ti3NS:Rh<sub>x</sub> decreased as Rh doped amount increased. Conversely, the photocatalytic activity of Ti3NS:Rh<sub>x</sub> for MB degradation increased as Rh doped amount increased. However, this cannot explain the improvement of photocatalytic activity due to the photodegradation of MB might be caused by photo-induced hole in Ti3NS valence band; the improvement of photocatalytic activity by Rh doped might be related to the change in valence band level. From a result of energy band structure, the Rh doping affected a valence band level of Ti3NS. The valence band level became higher than TiNS:Rh<sub>0</sub>, and it increased as Rh doped amount increased. However, the leveling of valence band level did not agree with the improvement of photocatalytic activity. Generally, the photodegradation will greatly occur when the catalyst has valence band level significantly lower than oxidation potential of organic molecules. However, the valence band level of Rh-doped Ti3NS:Rh<sub>x</sub> is increased as the doping amount increased; this should render the Ti3NS:Rh<sub>x</sub>'s efficiency. In spite of that, Ti3NS:Rh<sub>x</sub>'s efficiency is increased. As a result, the photocatalytic activity cannot be explained by the change of valence band level using Rh-doping.

Recently, K. Maeda *et al.*, and R. Abe *et al.* reported that the ratio of Rh<sup>3+</sup> and Rh<sup>4+</sup> in SrTiO<sub>3</sub> and BaTiO<sub>3</sub> has a huge impact on photocatalytic activity of Rh-doped SrTiO<sub>3</sub> and/or BaTiO<sub>3</sub>.<sup>42-48</sup> In our studies, Ti3NS:Rh<sub>x</sub>'s photocatalytic effect shows a correlational tendency of Rh<sup>4+</sup>/Rh<sup>3+</sup> change with Rh-doped amount due to the absorption spectra. Ti3NS:Rh<sub>0.001</sub> has the lowest ratio of Rh<sup>4+</sup>/Rh<sup>3+</sup> causing low photocatalytic activity for MB degradation. In contrast, Ti3NS:Rh<sub>0.008</sub> has higher ratio of Rh<sup>4+</sup>/Rh<sup>3+</sup> resulting in a slightly increase of quantum yield of photodegradation. Ti3NS:Rh<sub>0.03</sub> and Ti3NS:Rh<sub>0.048</sub> has high ratio of Rh<sup>4+</sup>/Rh<sup>3+</sup> and the quantum yield of photodegradation is nearly the same in both.

From this result, we can conclude that Rh<sup>4+</sup>/Rh<sup>3+</sup> is a key factor in explaining the change of photocatalytic activity for dye degradation, nonetheless, there are no experiments which can explain this phenomenon. We assume that there may be another

factor besides ratio of  $\text{Rh}^{4+}/\text{Rh}^{3+}$  which is the redox reaction of  $\text{Rh}^{3+}$  and  $\text{Rh}^{4+}$ . We suggest that  $\text{Rh}^{3+}$  and  $\text{Rh}^{4+}$  are responsible for activating reaction under UV light irradiation by  $\text{Rh}^{3+}$  accepting photo-induced hole from valence band of Ti3NS; While  $\text{Rh}^{4+}$  takes out electron from MB molecule which absorbs by Ti3NS. This results in a redox cycle of  $\text{Rh}^{3+}$  and  $\text{Rh}^{4+}$  which improves a photocatalytic reaction under UV light irradiation. Thus, the ratio of  $\text{Rh}^{4+}/\text{Rh}^{3+}$  and the reaction of oxidation and reduction time will affect this redox cycle directly. However, there is still no evidence to confirm this redox cycle. This will be the new challenge in the field of photocatalyst and also semiconducting material.

### 3.4 Conclusions

In this chapter, the synthesis and photoelectrochemical characterization of Ti3NS:Rh<sub>x</sub> were performed. The adsorption spectra showed a new absorption band which originated from Rh in 2 ionic states:  $\text{Rh}^{3+}$  and  $\text{Rh}^{4+}$ . A ratio of this absorption of  $\text{Rh}^{3+}$  and  $\text{Rh}^{4+}$  seem to be varied by Rh doped amount. The valence band level of the Ti3NS:Rh<sub>x</sub> was affected by Rh incorporation into the Ti sites. Adsorption capacity and photodegradation of MB under UV light by Ti3NS:Rh<sub>x</sub> was observed, and it varied with Rh doping. On the other hand, Ti3NS:Rh<sub>x</sub> did not adsorb MO due to the anionic charge of MO, and photodegradation of MO by Ti3NS:Rh<sub>x</sub> did not occur. The photodegradation activity of Ti3NS:Rh<sub>x</sub> was significantly improved with increased Rh doping, suggesting that the  $\text{Rh}^{4+}/\text{Rh}^{3+}$  ratio and redox cycle of  $\text{Rh}^{3+}$  and  $\text{Rh}^{4+}$  plays an important role in the photodegradation of MB under UV light irradiation in the presence of Ti3NS:Rh<sub>x</sub>.

### References

1. Sato, H., Ono, K., Sasaki, T., Yamagishi, A. (2003). First-Principles Study of Two-Dimensional Titanium Dioxides. *J. Phys. Chem. B*, 107(36), 9824-9828.
2. Sasaki, T., Ebina, Y., Watanabe, M., Decher, G. (2000). Multilayer ultrathin films of molecular titania nanosheets showing highly efficient UV-light absorption. *Chem. Commun.*, (21), 2163-2164.
3. Sasaki, T., Ebina, Y., Kitami, Y., Watanabe, M., Oikawa, T. (2001). Two-Dimensional Diffraction of Molecular Nanosheet Crystallites of Titanium

- Oxide. *J. Phys. Chem. B*, *105*(26), 6116-6121.
4. Sasaki, T., Ebina, Y., Fukuda, K., Tanaka, T., Harada, M., & Watanabe, M. (2002). Titania Nanostructured Films Derived from a Titania Nanosheet/Polycation Multilayer Assembly via Heat Treatment and UV Irradiation. *Chem. Mater.*, *14*(8), 3524-3530.
  5. Tanaka, T., Ebina, Y., Takada, K., Kurashima, K., Sasaki, T. (2003). Oversized Titania Nanosheet Crystallites Derived from Flux-Grown Layered Titanate Single Crystals. *Chem. Mater.*, *15*(18), 3564-3568.
  6. Maluangnont, T., Matsuba, K., Geng, F., Ma, R., Yamauchi, Y., & Sasaki, T. (2013). Osmotic Swelling of Layered Compounds as a Route to Producing High-Quality Two-Dimensional Materials. A Comparative Study of Tetramethylammonium versus Tetrabutylammonium Cation in a Lepidocrocite-type Titanate. *Chem. Mater.*, *25*(15), 3137-3146.
  7. Kikkawa, S., Yasuda, F., & Koizumi, M. (1985). Ionic conductivities of Na<sub>2</sub>Ti<sub>3</sub>O<sub>7</sub>, K<sub>2</sub>Ti<sub>4</sub>O<sub>9</sub> and their related materials. *Mater. Res. Bull.*, *20*(10), 1221-1227.
  8. Ogawa, M., & Takizawa, Y. (1999). Intercalation of Alkylammonium Cations into a Layered Titanate in the Presence of Macrocyclic Compounds. *Chem. Mater.*, *11*(1), 30-32.
  9. Sun, H., Zhou, G., Liu, S., Ang, H. M., Tadé, M. O., & Wang, S. (2013). Visible light responsive titania photocatalysts codoped by nitrogen and metal (Fe, Ni, Ag, or Pt) for remediation of aqueous pollutants. *Chem. Eng. J.*, *231*, 18-25.
  10. Okamoto, Y., Ida, S., Hyodo, J., Hagiwara, H., & Ishihara, T. (2011). Synthesis and Photocatalytic Activity of Rhodium-Doped Calcium Niobate Nanosheets for Hydrogen Production from a Water/Methanol System without Cocatalyst Loading. *J Am Chem Soc.*, *133*(45), 18034-18037.
  11. Ida, S., Kim, N., Ertekin, E., Takenaka, S., & Ishihara, T. (2014). Photocatalytic Reaction Centers in Two-Dimensional Titanium Oxide Crystals. *J. Am. Chem. Soc.*, *137*(1), 239-244.
  12. Milanović, M., Nikolić, L. M., Stijepović, I., Kontos, A. G., & Giannakopoulos, K. P. (2014). Steps in growth of Nb-doped layered titanates with very high surface area suitable for water purification. *Mater. Chem. Phys.*, *148*(3), 874-881.
  13. Dong, X., Osada, M., Ueda, H., Ebina, Y., Kotani, Y., Ono, K., Ueda, S., Kobayashi, K., Takada, K., Sasaki, T. (2009). Synthesis of Mn-Substituted Titania Nanosheets and Ferromagnetic Thin Films with Controlled Doping. *Chem. Mater.*, *21*(19), 4366-4373.
  14. Harada, M., Sasaki, T., Ebina, Y., & Watanabe, M. (2002). Preparation and characterizations of Fe- or Ni-substituted titania nanosheets as photocatalysts. *J. Photochem. Photobiol., A*, *148*(1-3), 273-276.
  15. Andersson, S., & Wadsley, A. D. (1961). The crystal structure of Na<sub>2</sub>Ti<sub>3</sub>O<sub>7</sub>. *Acta Crystallogr.*, *14*(12), 1245-1249.
  16. Yu, L., Xi, J., Li, M., Chan, H. T., Su, T., Phillips, D. L., & Chan, W. K. (2012). The degradation mechanism of methyl orange under photo-catalysis of TiO<sub>2</sub>. *Phys. Chem. Chem. Phys.*, *14*(10), 3589.
  17. Li, N., Zhang, L., Chen, Y., Fang, M., Zhang, J., & Wang, H. (2011).

- Highly Efficient, Irreversible and Selective Ion Exchange Property of Layered Titanate Nanostructures. *Adv. Funct. Mater.*, 22(4), 835-841.
18. Houas, A. (2001). Photocatalytic degradation pathway of methylene blue in water. *Appl. Catal., B*, 31(2), 145-157.
  19. Shang, X., Li, B., Zhang, T., Li, C., & Wang, X. (2013). Photocatalytic Degradation of Methyl Orange with Commercial Organic Pigment Sensitized TiO<sub>2</sub>. *Procedia Environ. Sci.*, 18, 478-485.
  20. Chen, T., Zheng, Y., Lin, J., & Chen, G. (2008). Study on the Photocatalytic Degradation of Methyl Orange in Water Using Ag/ZnO as Catalyst by Liquid Chromatography Electrospray Ionization Ion-Trap Mass Spectrometry. *J. Am. Soc. Mass Spectrom.*, 19(7), 997-1003.
  21. Xie, S., Huang, P., Kruzic, J. J., Zeng, X., & Qian, H. (2016). A highly efficient degradation mechanism of methyl orange using Fe-based metallic glass powders. *Sci. Rep.*, 6(1).
  22. Izawa, H., Kikkawa, S., & Koizumi, M. (1982). Ion exchange and dehydration of layered [sodium and potassium] titanates, Na<sub>2</sub>Ti<sub>3</sub>O<sub>7</sub> and K<sub>2</sub>Ti<sub>4</sub>O<sub>9</sub>. *J. Phys. Chem.*, 86(25), 5023-5026.
  23. Miyamoto, N., Kuroda, K., & Ogawa, M. (2004). Exfoliation and film preparation of a layered titanate, Na<sub>2</sub>Ti<sub>3</sub>O<sub>7</sub>, and intercalation of pseudoisocyanine dye. *J. Mater. Chem.*, 14(2), 165.
  24. Kuo, W., & Ho, P. (2006). Solar photocatalytic decolorization of dyes in solution with TiO<sub>2</sub> film. *Dyes Pigm.*, 71(3), 212-217.
  25. Kuo, W., & Ho, P. (2001). Solar photocatalytic decolorization of methylene blue in water. *Chemosphere*, 45(1), 77-83.
  26. Feng, M., You, W., Wu, Z., Chen, Q., & Zhan, H. (2013). Mildly Alkaline Preparation and Methylene Blue Adsorption Capacity of Hierarchical Flower-like Sodium Titanate. *ACS Appl. Mater. Interfaces*, 5(23), 12654-12662.
  27. Du, L., Wu, J., Qin, S., & Hu, C. (2011). Degradation mechanism of Methyl Orange by electrochemical process on RuO<sub>x</sub>-PdO/Ti electrode. *Water Sci. Technol.*, 63(7), 1539.
  28. Wetchakun, K., Wetchakun, N., & Phanichphant, S. (2015). Optimization of horizontal photocatalytic reactor for decolorization of methylene blue in water. *Desalin. Water Treat.*, 57(22), 10286-10294.
  29. Matthews, R. (1991). Photooxidative degradation of coloured organics in water using supported catalysts. TiO<sub>2</sub> on sand. *Water Res.*, 25(10), 1169-1176.
  30. Mills, A., and Wang, J. (1999). Photobleaching of methylene blue sensitised by TiO<sub>2</sub>: an ambiguous system? *J. Photochem. Photobiol., A*, 127(1-3), 123-134.
  31. Lv, T., Pan, L., Liu, X., & Sun, Z. (2012). Enhanced visible-light photocatalytic degradation of methyl orange by BiPO<sub>4</sub>-CdS composites synthesized using a microwave-assisted method. *RSC Adv.*, 2(33), 12706.
  32. Usami, H., & Sasaki, S. (2013). Fabrication and Photochemical Characterization of Organic Dye-Metal Oxide Hybrid Langmuir Blodgett Film. *J. Photopolym. Sci. Technol.*, 26(2), 207-211.
  33. Usami, H., Iijima, Y., Moriizumi, Y., Fujimatsu, H., Suzuki, E., & Inoue, H. (2007). Fabrication of dialkyldimethylammonium/vanadium oxide gel hybrid Langmuir-Blodgett membranes. *Res. Chem. Intermed.*, 33(1-2), 101-

110.

33. Konta, R., Ishii, T., Kato, H., & Kudo, A. (2004). Photocatalytic Activities of Noble Metal Ion Doped SrTiO<sub>3</sub> under Visible Light Irradiation. *J. Phys. Chem. B*, 35(37)
34. Sasaki, T., Watanabe, M., Hashizume, H., Yamada, H., & Nakazawa, H. (1996). Macromolecule-like Aspects for a Colloidal Suspension of an Exfoliated Titanate. Pairwise Association of Nanosheets and Dynamic Reassembling Process Initiated from It. *J. Am. Chem. Soc.*, 118(35), 8329-8335.
35. Osada, M., & Sasaki, T. (2012). 2D Inorganic Nanosheets: Two-Dimensional Dielectric Nanosheets: Novel Nanoelectronics From Nanocrystal Building Blocks. *Adv. Mater.*, 24(2), 209-209.
36. Kawasaki, S., Akagi, K., Nakatsuji, K., Yamamoto, S., Matsuda, I., Harada, Y., Yoshinobu, H., Komori, F., Takahashi, R., Lippmaa, M., Sakai, C., Niwa, H., Oshima, M., Iwashina, K., and Kudo, A. (2012). Elucidation of Rh-Induced In-Gap States of Rh:SrTiO<sub>3</sub> Visible-Light-Driven Photocatalyst by Soft X-ray Spectroscopy and First-Principles Calculations. *J. Phys. Chem. C*, 116(46), 24445-24448.
37. Iwashina, K., & Kudo, A. (2011). Rh-Doped SrTiO<sub>3</sub> Photocatalyst Electrode Showing Cathodic Photocurrent for Water Splitting under Visible-Light Irradiation. *J. Am. Chem. Soc.*, 133(50).
38. Kudo, A., & Miseki, Y. (2009). Heterogeneous photocatalyst materials for water splitting. *Chem. Soc. Rev.*, 38(1), 253-278.
39. Al-Ghamdi, A. (2006). Optical band gap and optical constants in amorphous Se<sub>96-x</sub>Te<sub>4</sub>Ag<sub>x</sub> thin films. *Vacuum*, 80(5), 400-405.
40. Zhang, J., & Nosaka, Y. (2014). Mechanism of the OH Radical Generation in Photocatalysis with TiO<sub>2</sub> of Different Crystalline Types. *J. Phys. Chem. C*, 118(20), 10824-10832.
41. Tseng, D., Juang, L., & Huang, H. (2012). Effect of Oxygen and Hydrogen Peroxide on the Photocatalytic Degradation of Monochlorobenzene in Aqueous Suspension. *Int. J. Photoenergy*, 2012, 1-9.
42. Kuncewicz, J., & Ohtani, B. (2015). Titania photocatalysis through two-photon band-gap excitation with built-in rhodium redox mediator. *Chem. Commun.*, 51(2), 298-301.
43. Maeda, K. (2014). Rhodium-Doped Barium Titanate Perovskite as a Stable p-Type Semiconductor Photocatalyst for Hydrogen Evolution under Visible Light. *ACS Appl. Mater. Interfaces*, 6(3), 2167-2173.
44. Okunaka, S., Tokudome, H., & Abe, R. (2015). Facile water-based preparation of Rh-doped SrTiO<sub>3</sub> nanoparticles for efficient photocatalytic H<sub>2</sub> evolution under visible light irradiation. *J. Mater. Chem. A*, 3(28), 14794-14800.
45. Yin, S., & Yu, F. T. (2000). *Photorefractive optics: materials, properties, and applications*. San Diego, CA: Academic.
46. Schneider, J., Bahnemann, D., Ye, J., Puma, G. L., & Dionysiou, D. D. (2016). *Photocatalysis: fundamentals and perspectives*. Cambridge: Royal Society of Chemistry.
47. Oropeza, F., & Egdell, R. (2011). Control of valence states in Rh-doped

TiO<sub>2</sub> by Sb co-doping: A study by high resolution X-ray photoemission spectroscopy. *Chem. Phys. Lett.*, 515(4-6), 249-253.

48. Kučera, M., Kuneš, J., & Gerber, R. (1999). Magneto-optical effects of Rh<sup>3+</sup> and Rh<sup>4+</sup> doped yttrium iron garnet. *J. Appl. Phys.*, 85(8), 5986-5988.

## Chapter 4

# The photocatalytic Activity of Rh Doped Titanate Nanosheet for Hydrogen Evolution

### 4.1 Introduction

The efficient production of H<sub>2</sub> gas from water by using sun-light energy is one of the artificial photosynthesis field's goals. Thus, the researches and developments of various photocatalytic materials for water-splitting reaction under sun-light irradiation have been studied by many researchers.<sup>1-5</sup>

Due to large specific surface area and semiconducting property, titanate nanosheets (TiNS) is well known as the promising photocatalyst for photo-induced water splitting reaction and can be prepared from alkaline titanate such as A<sub>2</sub>Ti<sub>n</sub>O<sub>2n+1</sub> (A: alkaline metal, *n* = 3, 4, ...). This alkaline titanate can work as a photocatalyst for production of H<sub>2</sub> gas from water-splitting reaction. However, the large energy band gap makes them active only under the UV light irradiation. The development of novel photocatalytic materials which can work under sun-light irradiation are actively carried out due to sun-light is an unlimited source of energy without cost. Therefore, the photocatalytic properties of the synthesized noble materials have been investigated intensively.

Currently, Rh doping on metal oxides i.e. TiO<sub>2</sub> or SrTiO<sub>3</sub> causes metal oxides to be photocatalytically active under visible light due to Rh replaces Ti. In addition, Rh also creates a new electronic band structure which reduces the energy band gap.<sup>5-11</sup> Nonetheless, its photocatalytic activity is low, hence, cocatalyst is used to enhance the photocatalytic activity. Cocatalyst, which are metal or metal oxides of transition metals such as Rh, Pt, Au, and Ag, acts as an electron pool meaning it collects photogenerated electron from photocatalyst.<sup>12-20</sup> Unfortunately, this cocatalyst only attaches on the surface area, therefore, the inward photogenerated electrons in bulk molecule requires long life times to transport to the cocatalyst for the reaction to occur. Even with the help of cocatalyst, the bulk molecule has a wide width which makes it hard for the reaction to occur resulting in low photocatalytic activity.

In order to increase the photocatalytic activity, photocatalysts with a sheet like structure are necessary. Accordingly, titanate nanosheet is thought to be a promising

photocatalyst but it still requires the abilities to photocatalytically active under visible light irradiation.

In previous chapter, we synthesized Rh-doped Ti3NS ( $[\text{Ti}_{3-x}\text{Rh}_x\text{O}_7]^{2-}$ ). As results, the Rh doping affects energy band structure causing Ti3NS to absorb visible light. This implies that it can be used for H<sub>2</sub> production under visible irradiation. However, there are no reports about this and Rh doping was suggested to have same effect as cocatalyst in the past few years. Consequently, this chapter aims to find the differences between Rh doping and Rh cocatalyst loading on titanate nanosheet.<sup>21-23</sup>

In this chapter, Rh loaded Ti3NS with Rh amount equal to Rh doped Ti3NS as previously mentioned in chapter 3 were studied for their physical properties, and photocatalytic activities on H<sub>2</sub> production. Moreover, the effect of Rh doping on Ti3NS was also investigated for photocatalytic H<sub>2</sub> production under visible light irradiation.

## 4.2 Experimental Procedures

### *Materials*

Sodium carbonate Na<sub>2</sub>CO<sub>3</sub> (99.9%) from Wako Pure Chemical Industries Co., anatase-type TiO<sub>2</sub> (99.7%) from High Purity Chemicals Co., Rh<sub>2</sub>O<sub>3</sub> (99.9%) and RhCl<sub>3</sub>·9H<sub>2</sub>O from Wako Pure Chemical Industries Co., methylamine (CH<sub>3</sub>NH<sub>2</sub>, 40wt.% solution) and tetramethylammonium hydroxide (TMAOH, 26wt.% solution) from Tokyo Chemical Industry Co., and triethylamine (N(CH<sub>2</sub>CH<sub>3</sub>)<sub>3</sub>, TEA) from Wako Pure Chemical Industries Co. were used without further purification.

### *Preparation of the Rh-doped titanate nanosheets and Rh-load titanate nanosheets*

The colloidal suspension of Ti3NS:Rh<sub>x</sub> ( $[\text{Ti}_{3-x}\text{Rh}_x\text{O}_7]^{2-}$ ) was prepared as described in previous chapter. Meanwhile, the Rh co-catalyst loaded titanate nanosheets (Rh<sub>x</sub>-Ti3NS, where  $x$  is loading amount) was prepared by the photodeposition method reported by Shimura *et al.*<sup>24-25</sup> In the photodeposition method, the powder of photocatalyst (H<sub>2</sub>Ti<sub>3</sub>O<sub>7</sub>, 0.2 g) was dispersed into 10% vol methanol solution (5 ml) containing the RhCl<sub>3</sub>·9H<sub>2</sub>O. The solution was stirred in room temperature and in

present of oxygen from the atmosphere. The photodeposit was done by irradiating using 300 W xenon lamp, which emitted from UV to visible light for 24 hours with continuous stirring. The Rh-loaded photocatalyst powder was collected by filtration, and washing with distilled water. Then, the powder was dried in vacuum overnight, and Rh loaded  $\text{H}_2\text{Ti}_3\text{O}_7$  was obtained. The Ti/Rh ratio was set as same as Rh-doped Ti3NS. The collected Rh loaded  $\text{H}_2\text{Ti}_3\text{O}_7$  was neutralized by methylamine aqueous solution at 333 K for 6 days to yield Rh loaded  $(\text{CH}_3\text{NH}_3)_2\text{Ti}_3\text{O}_7$  powder. Subsequently, Rh loaded  $(\text{CH}_3\text{NH}_3)_2\text{Ti}_3\text{O}_7$  was dispersed in TMAOH solution ( $[\text{Ti}_3\text{O}_7^{2-}]/[\text{TMAOH}] = 5$ ) by sonication for 5 days. Non-exfoliated was removed by centrifugation (at 4000 rpm or 1150 G for 15 min, IEC61010-2-020, KUBOTA). The Rh $_x$ -Ti3NS colloidal suspension was obtained as the supernatant.

#### *H<sub>2</sub> evolution experiment.*<sup>26-27</sup>

All photochemical reactions were performed in a closed gas circulation system with a Pyrex reaction cell. The reaction solution (10 cm<sup>3</sup>) containing TEA (0.36 mol/dm<sup>3</sup>) and Ti3NS:Rh $_x$  and Rh $_x$ -Ti3NS colloidal suspension (1 mg) was degassed by repeated freeze pump-thaw cycles. The reaction solution was shifted into the reaction vessel with a glove box under an Ar-saturated atmosphere. The reaction solution was irradiated at 300 K using a 500 W Xe lamp (USHIO Co.) equipped with optical cut-off filters (short pass filter  $\lambda < 220$ , and long pass filter  $\lambda > 340$ ,  $\lambda > 380$ , and  $\lambda > 480$  nms, Kenko Co.). The amount of evolved H<sub>2</sub> gas was determined using a gas chromatograph (Shimadzu; GC-8A with TCD detector, a stainless-steel column packed with molecular sieves-5A, and ultra-pure Ar carrier gas). All measurements were performed under non-oxygen conditions.

## *Characterization*

To analyze crystal structure of all materials, the powder X-ray diffraction (XRD) analysis was carried out by X-ray diffractometer (RIGAKU, MiniFlex II). Absorption spectra of various samples was measured by UV-Vis spectrophotometer (V-670 UV-VIS-NIR spectrophotometer, JASCO). Absorption spectra of liquid samples was measured by transmission mode. Diffuse reflectance (DR) spectra of solid sample was measured by UV-Vis spectrophotometer attached to an integrating sphere system (ISN-723, JASCO). Doped and loaded amount of Rh in and Rh<sub>x</sub>-Ti<sub>3</sub>NS was estimated by ICP-AES apparatus (Optima2000DV, Perkinelmer). Scanning electron microscopy imaging was performed using JEOL-7001FA (JEOL Ltd.) operated at 12 kV.

### **4.3 Results and discussion**

#### *Preparation of Rh-loaded titanate nanosheets by photodeposition method and comparison with Rh-doped titanate nanosheets*

Figure 4.1 shows the the obtained powder of non-doped Ti<sub>3</sub>NS (Ti<sub>3</sub>NS:Rh<sub>0</sub>), Rh-loading Ti<sub>3</sub>NS (Rh<sub>0.03</sub>-Ti<sub>3</sub>NS), and Rh-doping Ti<sub>3</sub>NS (Ti<sub>3</sub>NS:Rh<sub>0.03</sub>). The powder color changed from white to yellow brown by the way of Rh addition. Figure 4.2 shows a transmission electron microscopy (TEM) images of Rh<sub>0.03</sub>-Ti<sub>3</sub>NS and Ti<sub>3</sub>NS:Rh<sub>0.03</sub>. Although only homogeneous nanosheet shape could be observed in the TEM image of Ti<sub>3</sub>NS:Rh<sub>0.03</sub>, black spots in homogeneous nanosheet image could be observed in the TEM image of Rh<sub>0.03</sub>-Ti<sub>3</sub>NS. These results indicate that Rh was doped in skeleton structure of titanate as atom in the case of Ti<sub>3</sub>NS:Rh<sub>0.03</sub>. On the other hand, Rh existed as Rh<sub>2</sub>O<sub>3</sub> nano particles (< 10 nm) in Rh<sub>0.03</sub>-Ti<sub>3</sub>NS.



Figure 4.1 Picture of synthesized non-doped Ti3NS (Ti3NS:Rh0), Rh-loading Ti3NS (Rh0.03-Ti3NS), and Rh-doping Ti3NS (Ti3NS:Rh0.03).

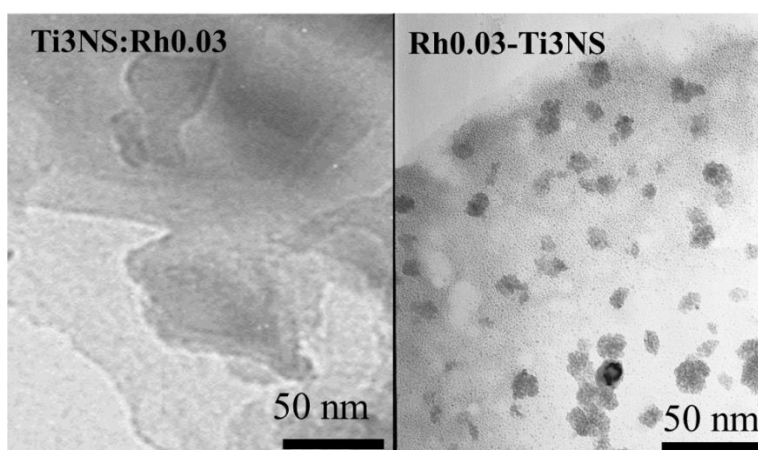


Figure 4.2 TEM image of Rh-doped (Ti3NS:Rh0.03) and Rh-loaded (Rh0.03-Ti3NS) titrate nanosheet.

Figure 4.3 shows the photo-adsorption of Rh<sub>0.03</sub>-Ti<sub>3</sub>NS and Ti<sub>3</sub>NS:Rh<sub>0.03</sub> in term of Kubelka-Munk function. The result shows the difference in absorption band. Ti<sub>3</sub>NS:Rh<sub>0.03</sub> showed the absorption band in visible region, while the Rh<sub>0.03</sub>-Ti<sub>3</sub>NS did not show another absorption band except the absorption band originated from Ti<sub>3</sub>NS. This result designated that the Rh loading did not affect the energy band structure of Ti<sub>3</sub>NS.

From ICP-AES, the ratio of Ti and Rh atom in Ti<sub>3</sub>NS:Rh<sub>x</sub> and Rh<sub>x</sub>-Ti<sub>3</sub>NS nanosheet was measured, and the chemical formula of Ti<sub>3</sub>NS:Rh<sub>x</sub> were also realized as written in Table 4.1. The Rh/Ti ratio of Rh<sub>x</sub>-Ti<sub>3</sub>NS are same as in Ti<sub>3</sub>NS:Rh<sub>x</sub>. From this result, the Rh loading which has a same Rh/Ti ratio as compared with Rh doping can be prepared from the present method.

#### *Photocatalytic H<sub>2</sub> evolution by Ti<sub>3</sub>NS:Rh<sub>x</sub> under UV light and effect of Rh-doping and Rh loading*

The dependence of photocatalytic H<sub>2</sub> evolution on irradiation time of UV light (< 220 nm) is shown in Figure 4.4. All of Ti<sub>3</sub>NS:Rh<sub>x</sub> exhibited the photo-induced H<sub>2</sub> production reaction under UV light irradiation. The H<sub>2</sub> evolution linearly increased with an increase in irradiation time. As a result, this reaction can be proceeded by the oxidation reaction of TEA as a sacrificial agent.

The H<sub>2</sub> evolution by Ti<sub>3</sub>NS:Rh<sub>x</sub> was measured for 3 cycles to confirm the stability of Ti<sub>3</sub>NS:Rh<sub>x</sub> photocatalytic ability as shown in Figure 4.5. Ti<sub>3</sub>NS:Rh<sub>x</sub> sample show the good stability due to the reaction could be repeated under the same condition.

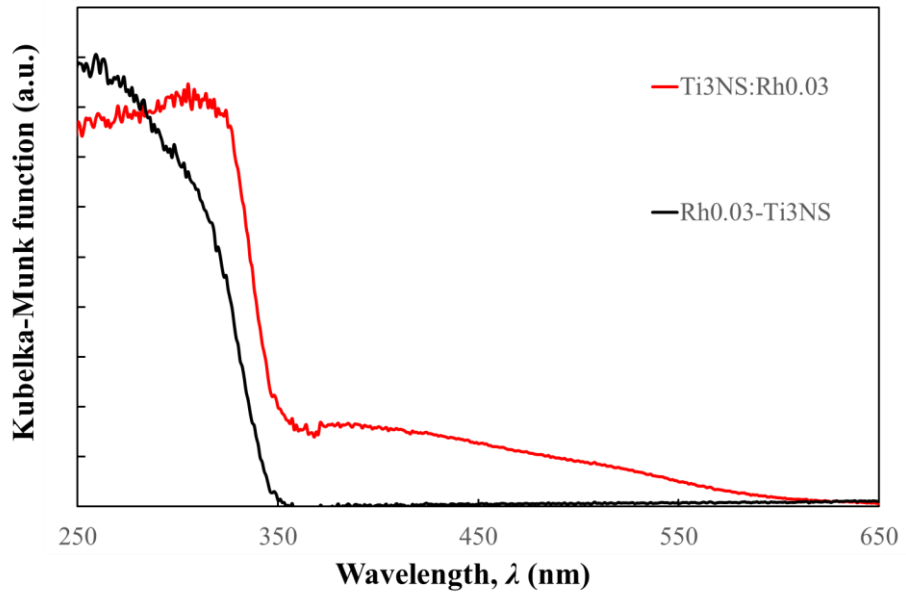


Figure 4.2 The diffuse reflectance spectra in term of Kubelka-Munk function of Rh-doped (Ti3NS:Rh0.03) and Rh-loaded (Rh0.03-Ti3NS) titnate nanosheet.

Table 4.1 Rh/Ti ratio of all prepared samples.

Sample	Rh/Ti ratio
Ti3NS:Rh0.008	0.0028
Ti3NS:Rh0.03	0.0101
Ti3NS:Rh0.048	0.0163
Rh0.008-Ti3NS	0.0026
Rh0.03-Ti3NS	0.0098
Rh0.048-Ti3NS	0.0155

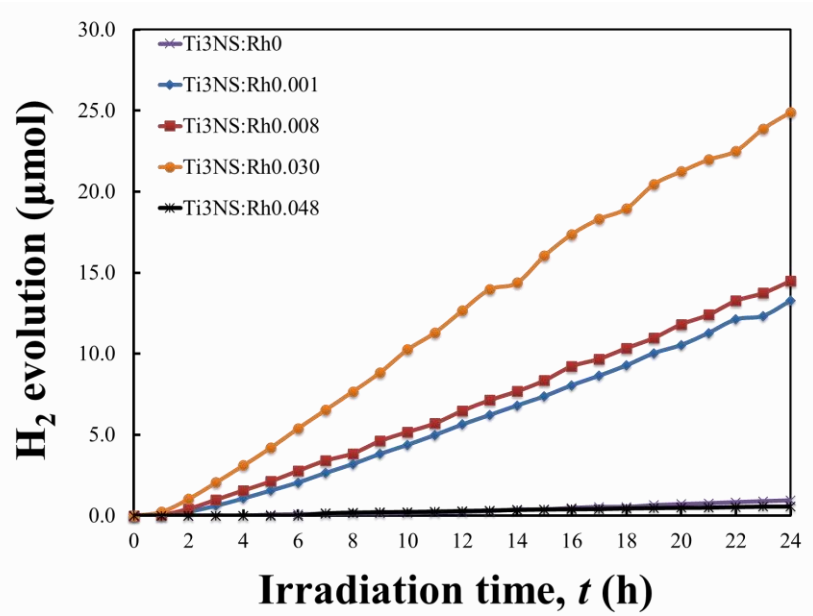


Figure 4.4 The H<sub>2</sub> evolution by Ti3NS:Rh<sub>x</sub> plotted with irradiation time by using UV light ( $\lambda < 220$  nm).

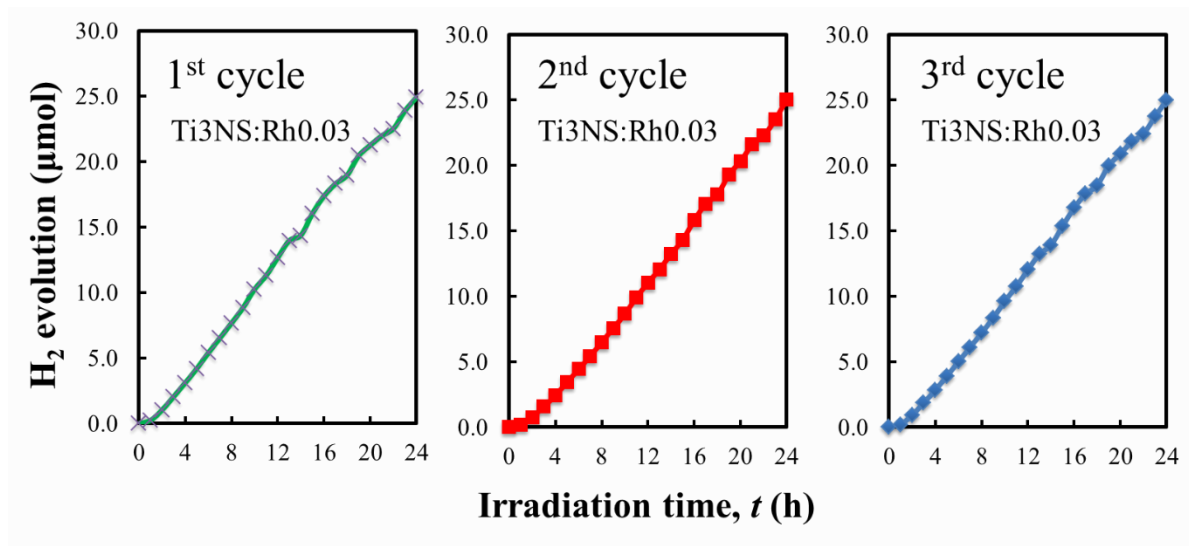


Figure 4.5 The H<sub>2</sub> evolution by Ti<sub>3</sub>NS:Rh<sub>0.03</sub> measured 3 cycles to observe the stability under UV light ( $\lambda < 220$  nm) irradiation.

However, the photo-induced H<sub>2</sub> evolution activity of Ti<sub>3</sub>NS:Rh<sub>0</sub> was extremely low. Additionally, this low activity agreed with the results reported by Mallouk *et.al.*; they reported that H<sub>2</sub>Ti<sub>3</sub>O<sub>7</sub> was not a good photocatalyst for photo-induced H<sub>2</sub> production. Meanwhile, the photo-induced H<sub>2</sub> evolution of Ti<sub>3</sub>NS:Rh<sub>x</sub> increased with an increase in Rh doping amount up to  $x = 0.03$ . These results indicated that Rh doping can improve the photocatalytic activity of Ti<sub>3</sub>NS for H<sub>2</sub> evolution because the doping Rh atom could work as H<sub>2</sub>-production active site. Nevertheless, the photo-induced H<sub>2</sub> evolution of Ti<sub>3</sub>NS:Rh<sub>x</sub> drastically decreased at  $x = 0.048$ . This experimental fact implies that the optimal doping amount of Rh for the photo-induced H<sub>2</sub> evolution reaction exists.

Figure 4.6 exhibits the photocatalytic H<sub>2</sub> production of each Ti<sub>3</sub>NS:Rh<sub>x</sub> compared with Rh<sub>x</sub>-Ti<sub>3</sub>NS at same  $x$ . These results indicated that the Rh<sub>2</sub>O<sub>3</sub> nano particles on titanate nanosheet could work as the H<sub>2</sub> evolution active site. However, the H<sub>2</sub> evolution amount was different.

In Figure 4.7, the H<sub>2</sub> evolution rate was plotted against the molar ratio of Rh and Ti. Interestingly, the H<sub>2</sub> evolution rate exhibited the different dependence on the molar ratio of Rh and Ti. In the case of Ti<sub>3</sub>NS:Rh<sub>x</sub>, the H<sub>2</sub> evolution rate was drastically increased by the small doping amount of Rh, and then, gradually increased with an increase in the doping amount of Rh up to  $x = 0.03$ . When the doping amount of Rh was  $x = 0.048$ , the H<sub>2</sub> production could not be observed under UV irradiation. Then, the H<sub>2</sub> evolution rate showed maximum value at  $x = 0.03$  in the case of the Rh<sub>x</sub>-Ti<sub>3</sub>NS. The maximum value of H<sub>2</sub> evolution rate for Rh<sub>0.03</sub>-Ti<sub>3</sub>NS (1970  $\mu\text{mol}\cdot\text{g}^{-1}\cdot\text{h}^{-1}$ ) was higher than that for Ti<sub>3</sub>NS:Rh<sub>0.03</sub> (1040  $\mu\text{mol}\cdot\text{g}^{-1}\cdot\text{h}^{-1}$ ), but it was found that the higher efficiency for the photo-induced H<sub>2</sub> evolution reaction was yielded by doping Rh atom to Ti sites than the Rh loading.

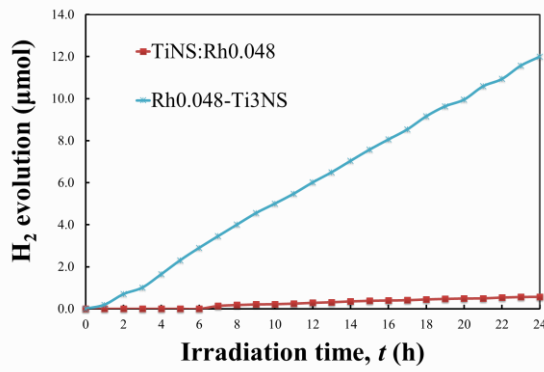
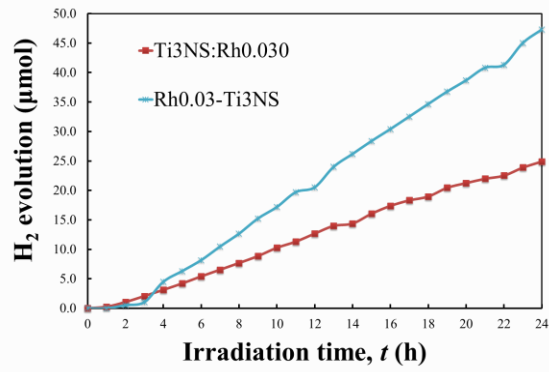
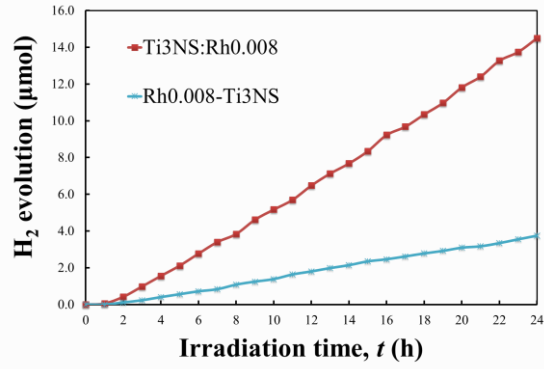


Figure 4.6 The H<sub>2</sub> evolution by Ti<sub>3</sub>NS:Rh<sub>x</sub> and Rh<sub>x</sub>-Ti<sub>3</sub>NS compared at each same amount of Rh doping and/or Rh loading.

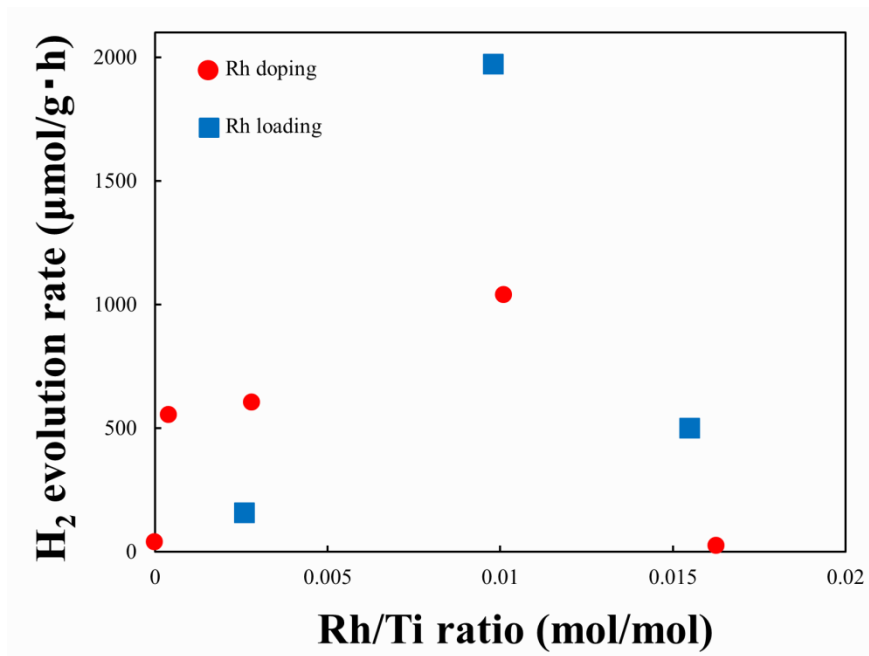


Figure 4.7 The H<sub>2</sub> evolution rate plotted with Rh/Ti ratio of Ti<sub>3</sub>NS:Rh<sub>x</sub> and Rh<sub>x</sub>-Ti<sub>3</sub>NS.

The renowned method for enhancing H<sub>2</sub> evolution is to load catalysts onto the photocatalyst surface. Rh loading displays an enhancement of H<sub>2</sub> evolution from decomposition of TEA. In contrast, Rh doping has a quadruple of H<sub>2</sub> evolution rate at x=0.008 compared to Rh loading. On the other hand, Rh loading has an extremely higher H<sub>2</sub> evolution rate than Rh doping at x=0.048. Hence, the effect of Rh doping and Rh loading is completely distinct.

According to Chapter 3, the Rh doping effect on photocatalytic activity of Ti3NS for photodegradation of organic dyes was studied. The result revealed that Rh doping can improve the photocatalytic activity of Ti3NS for photo oxidative degradation of organic dyes. The improvement is increased as the Rh doped amount increases. We assumed that this aspect was due to presence of Rh<sup>3+</sup> and Rh<sup>4+</sup>, and redox reaction of Rh<sup>3+</sup> and Rh<sup>4+</sup> under UV light irradiation.

We can consider the ratio of Rh<sup>3+</sup> to Rh<sup>4+</sup> by estimating the ratio of adsorption peak of adsorption band of Rh<sup>3+</sup> to Rh<sup>4+</sup> (see figure 3.12, and 3.13 in chapter 3). From Kudo *et.al.* report, it has been found that the absorption band of Rh<sup>4+</sup> was indicated around 500-650 nm, while the absorption band of Rh<sup>3+</sup> was indicated around 350-450 nm.<sup>8-10</sup> If we defined the absorbance at 550 nm represent the top absorption peak of Rh<sup>4+</sup> and absorbance at 400 nm represent the top absorption peak of Rh<sup>3+</sup>, then plotted between Rh doped amount and the absorbance at 400 nm per absorbance at 550 nm which represent the Rh<sup>3+</sup>/Rh<sup>4+</sup> ratio. We would find that Rh<sup>3+</sup>/Rh<sup>4+</sup> ratio gradually decrease when Rh doped amount increases meaning Rh<sup>4+</sup> will steadily increase (Figure 4.8). When Rh<sup>4+</sup> increases, H<sub>2</sub> evolution rate will slowly increase and then progressively decrease at Ti3NS: Rh0.048 where the amount of Rh<sup>4+</sup> is the highest. Nevertheless, Maeda, *et. al.* reported about the effect of Rh<sup>4+</sup> on photocatalytic activity of BaTiO<sub>3</sub> for H<sub>2</sub> evolution.<sup>28</sup> When Rh<sup>4+</sup> is increased in the system of BaTiO<sub>3</sub> resulting in H<sub>2</sub> evolution rate decreases since Rh<sup>4+</sup> is not stable; therefore, it consumes electrons to reduce itself to Rh<sup>3+</sup>. The electrons used in reducing Rh<sup>4+</sup> come from two pathways which are electron donor or TEA molecule, and photogenerated electron.

Consequently, when there are high numbers of Rh<sup>4+</sup> in the system; the photo-generated electron will be consumed by Rh<sup>4+</sup> causing the H<sub>2</sub> evolution reaction to hardly occur or reaction rate decreases.<sup>29-32</sup> Simply, Rh<sup>4+</sup> acts as hole pool, in contrast, Rh<sup>3+</sup> acts as electron pool. Although, Rh<sup>4+</sup> will accept electron and reduce itself to Rh<sup>3+</sup> but this does not increase the H<sub>2</sub> evolution reaction. The reason is that Rh<sup>3+</sup> can change to Rh<sup>4+</sup> from the oxidation reaction between Rh<sup>3+</sup> and h<sup>+</sup> in the valence band. Hence, H<sub>2</sub> evolution rate does not rise when Rh doped amount increases. This can be used to explain why the H<sub>2</sub> evolution rate of Ti3NS:Rh0.008 and Ti3NS:Rh0.01 do not differ much. In spite of this, the ratio of Rh<sup>3+</sup>/Rh<sup>4+</sup> is not the only factor; there is another key factor which is the redox reaction of Rh<sup>3+</sup>, and Rh<sup>4+</sup>.

Moreover, Ti3NS:Rh0.03 has lower H<sub>2</sub> evolution rate than Rh0.03-Ti3NS which can be explained by redox reaction of Rh<sup>3+</sup> and Rh<sup>4+</sup>. In the case of Rh-loading, Rh either in the form of metal oxide acts as co-catalyst for accumulation of photo-generated electron as electron pool.<sup>24-25</sup> In addition, it also affects the photogenerated electron-hole to be spatially separated due to the electrons and holes are localized on the surface of photocatalyst and co-catalyst. On the contrary, Rh-doping enhances

photocatalytic activity of Ti3NS by different mechanism. Rh doping can be doped in the form of  $Rh^{3+}$  and  $Rh^{4+}$  in the oxidation state. While  $Rh^{3+}$  acts as an electron pool which is similar to Rh-loading;  $Rh^{4+}$  acts reversely.  $Rh^{4+}$  reduces the efficiency of  $H_2$  evolution; Ti3NS:Rh0.03 has both  $Rh^{3+}$  and  $Rh^{4+}$ , hence, it has  $H_2$  evolution rate lower than Rh0.03-Ti3NS.

$$R_{abs} = \frac{\text{Absorbance at 400 nm}}{\text{Absorbance at 550 nm}}$$

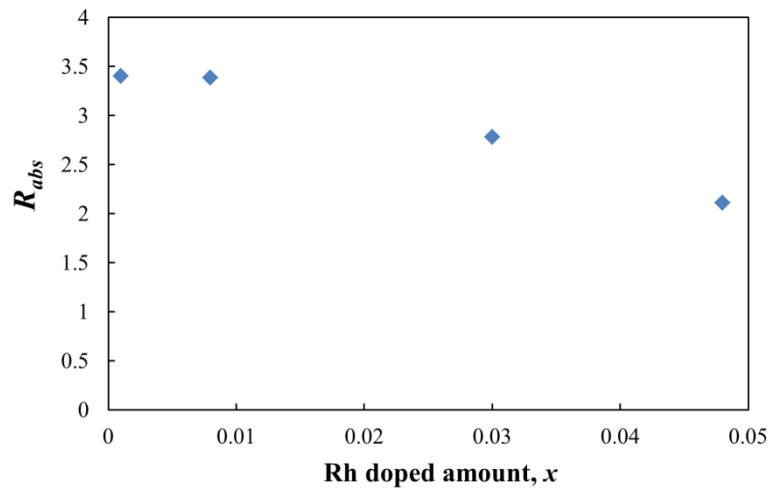


Figure 4.8 The absorbance ratio plotted with Rh doped amount to show the the  $\text{Rh}^{3+}/\text{Rh}^{4+}$  ratio.

In case of Ti3NS:Rh0.001 and Ti3NS:Rh0.008, both of them has higher H<sub>2</sub> evolution rate than Rh0.008-Ti3NS. Thence, the Rh doping helps improving photocatalytic activity better than Rh loading. The reason is that Rh<sup>3+</sup> was only found in photoadsorption spectra of Ti3NS:Rh0.001 and Ti3NS:Rh0.008 resulted in electron pool acts Rh site at the structure of Ti3NS. Furthermore, H<sub>2</sub> evolution rate of Rh doping is higher than Rh-loading due to the distribution of electron pool site is totally different. In Rh-doping, Rh site is diversely distributed than Rh loading. This is because Rh will replace Ti site but it cannot stay close to each other as it will disrupt crystal structure of Ti3NS. Meanwhile, Rh metal or metal oxide in Rh-loading only sticks on the surface of Ti3NS sheet. Accordingly, there is a possibility that particle of Rh metal or metal oxide will combine resulting in conversely distribution. To conclude, this causes Ti3NS:Rh0.001 and Ti3NS:Rh0.008 to has more electron pool and higher H<sub>2</sub> evolution rate than Rh0.08:Ti3NS. This can be described as a simple diagram as shown in figure 4.9.

*Photocatalytic H<sub>2</sub> evolution by Ti3NS:Rh<sub>x</sub> under visible light*

From the absorption spectra result, Ti3NS:Rh<sub>x</sub> showed the absorption band in visible range due to the Rh-doping. However, the absorption spectra of Rh<sub>x</sub>-Ti3NS did not differ from Ti3NS. Thus, Rh-loaded Ti3NS cannot photocatalytic active under visible light. To observe the photocatalytic activity of Ti3NS:Rh<sub>x</sub> under visible light irradiation, we chose Ti3NS:Rh0.03 because Ti3NS:Rh0.03 showed the highest H<sub>2</sub> evolution rate

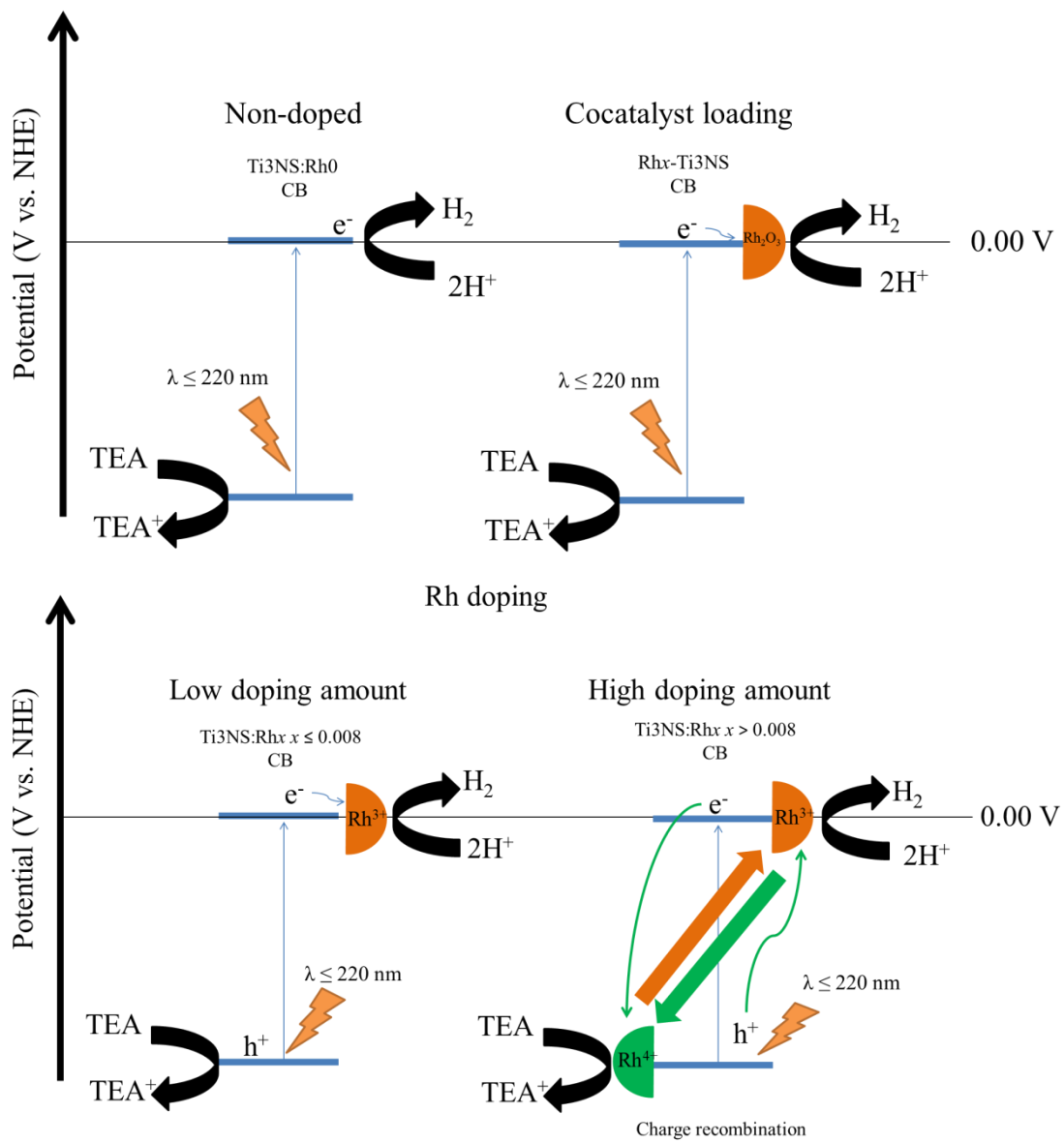


Figure 4.9 Figure 4.8 A schematic diagram of photocatalytic  $H_2$  evolution by Ti3NS with Rh-loading and Rh-doping.

In Figure 4.10, DR spectrum and the dependence of H<sub>2</sub> evolution rate of Ti<sub>3</sub>NS:Rh<sub>0.03</sub> on wavelength of long-pass optical filter are shown. When the light including UV light are irradiated to Ti<sub>3</sub>NS:Rh<sub>0.03</sub>, the photo-induced H<sub>2</sub> evolution could be observed. Nonetheless, the photo-induced H<sub>2</sub> evolution could not be observed with only visible light irradiation to Ti<sub>3</sub>NS:Rh<sub>0.03</sub>, even there are absorption bands originated from Rh<sup>3+</sup> and/or Rh<sup>4+</sup> species in the visible range. These results indicates that the present Ti<sub>3</sub>NS:Rh<sub>x</sub> can have the photo-induced H<sub>2</sub> evolution reaction activity under only UV light irradiation, although Ti<sub>3</sub>NS:Rh<sub>0.03</sub> has the absorption band originated from Rh<sup>3+</sup> and/or Rh<sup>4+</sup> in the visible light range. Thus, it was found that the doped Rh atoms can have roles as photo-induced electron pool and H<sub>2</sub>O reduction site, but doped Rh atoms cannot have an aggressive influence on the electron structure of Ti<sub>3</sub>NS.

#### 4.4 Conclusion

The Rh-loaded titanate nanosheet could be obtained from the photodeposition method. From TEM image, the difference between Rh-doping and loading was found. TEM image of Rh<sub>x</sub>-Ti<sub>3</sub>NS showed the nanoparticle formed on the surface of Ti<sub>3</sub>NS. The absorption spectra of Rh<sub>x</sub>-Ti<sub>3</sub>NS did not exhibit the absorption band except the absorption band of Ti<sub>3</sub>NS. The photocatalytic H<sub>2</sub> evolution have been investigated under UV light and visible light; as a result, the Rh doping can improve the photocatalytic activity of Ti<sub>3</sub>NS for H<sub>2</sub> evolution as same as Rh cocatalyst loading. However, the effect of Rh doping and loading was different. The Rh loading improved the photocatalytic H<sub>2</sub> evolution of Ti<sub>3</sub>NS by acting as the cocatalyst with the electron pool effect. While, the Rh doping improved the photocatalytic activity due to the presence of Rh<sup>3+</sup>. However, in the high doping amount, Rh also existed as both of Rh<sup>3+</sup> and Rh<sup>4+</sup>. The Rh<sup>4+</sup> became the hole pool opposing the electron pool which are generated from Rh<sup>3+</sup> resulting in the charge recombination which cause the lower photocatalyst efficiency than Rh-cocatalyst loading. However, at low doping amount ( $x = 0.001$ , and  $0.008$ ), the Rh doped Ti<sub>3</sub>NS was a better photocatalyst than Rh loaded Ti<sub>3</sub>NS. From a result of photocatalytic H<sub>2</sub> evolution by visible light, Rh doping cannot enhance the photocatalytic activity of Ti<sub>3</sub>NS in the visible region even it showed an absorption band in visible region.

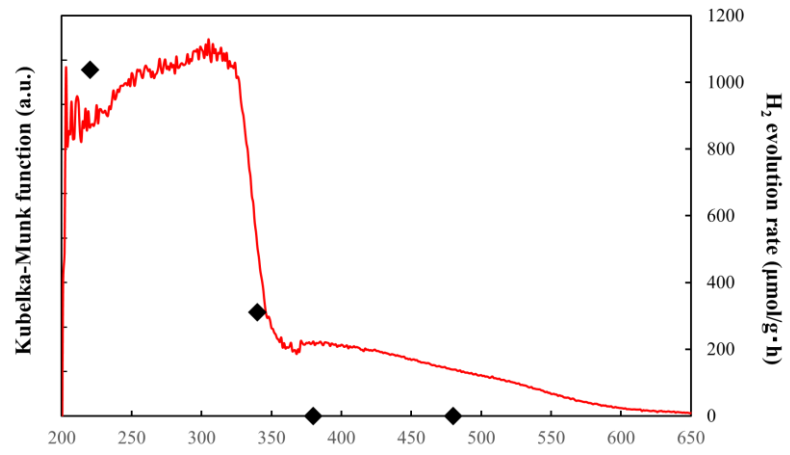


Figure 4.10 The H<sub>2</sub> evolution rate from TiNS:Rh0.03 as a function of wavelength of irradiation light (dot), and the diffuse reflectance spectra in term of Kubelka-Munk function of TiNS:Rh0.03 (line).

## References

1. Jafari, T., Moharreri, E., Amin, A., Miao, R., Song, W., & Suib, S. (2016). Photocatalytic Water Splitting—The Untamed Dream: A Review of Recent Advances. *Molecules*, *21*(7), 900.
2. Zhang, X., Du, Y., Zhou, Z., & Guo, L. (2010). A simplified method for synthesis of band-structure-controlled  $(\text{CuIn})_x\text{Zn}_{2(1-x)}\text{S}_2$  solid solution photocatalysts with high activity of photocatalytic  $\text{H}_2$  evolution under visible-light irradiation. *Int. J. Hydrogen Energy*, *35*(8), 3313-3321.
3. Xiong, X., Zhang, X., & Xu, Y. (2016). Concentration dependent effect of  $\text{CuCl}_2$  on the photocatalytic degradation of phenol over anatase, rutile and brookite  $\text{TiO}_2$ . *RSC Adv.*, *6*(44), 38169-38175.
4. Fujishima, A., Zhang, X., & Tryk, D. (2008).  $\text{TiO}_2$  photocatalysis and related surface phenomena. *Surf. Sci. Rep.*, *63*(12), 515-582.
5. Martin, D. J., Qiu, K., Shevlin, S. A., Handoko, A. D., Chen, X., Guo, Z., & Tang, J. (2014). Highly Efficient Photocatalytic  $\text{H}_2$  Evolution from Water using Visible Light and Structure-Controlled Graphitic Carbon Nitride. *Angew. Chem., Int. Ed.*, *53*(35), 9240-9245.
6. Kudo, A., & Miseki, Y. (2009). Heterogeneous Photocatalyst Materials for Water Splitting. *Chem. Soc. Rev.*, *38*(1), 253-278.
7. Konta, R., Ishii, T., Kato, H., & Kudo, A. (2004). Photocatalytic Activities of Noble Metal Ion Doped  $\text{SrTiO}_3$  under Visible Light Irradiation. *J. Phys. Chem. B*, *35*(37).
8. Iwashina, K., & Kudo, A. (2011). Rh-Doped  $\text{SrTiO}_3$  Photocatalyst Electrode Showing Cathodic Photocurrent for Water Splitting under Visible-Light Irradiation. *J. Am. Chem. Soc.*, *42*(50).
9. Kawasaki, S., Akagi, K., Nakatsuji, K., Yamamoto, S., Matsuda, I., Harada, Y., Yoshinobu, H., Komori, F., Takahashi, R., Lippmaa, M., Sakai, C., Niwa, H., Oshima, M., Iwashina, K., and Kudo, A. (2012). Elucidation of Rh-Induced In-Gap States of Rh: $\text{SrTiO}_3$  Visible-Light-Driven Photocatalyst by Soft X-ray Spectroscopy and First-Principles Calculations. *J. Phys. Chem. C*, *116*(46), 24445-24448.
10. Kunczewicz, J., & Ohtani, B. (2015). Titania photocatalysis through two-photon band-gap excitation with built-in rhodium redox mediator. *Chem. Commun.*, *51*(2), 298-301.
11. Oropeza, F., & Egdell, R. (2011). Control of valence states in Rh-doped  $\text{TiO}_2$  by Sb co-doping: A study by high resolution X-ray photoemission spectroscopy. *Chem. Phys. Lett.*, *515*(4-6), 249-253.
12. Yang, J., Wang, D., Han, H., & Li, C. (2013). Roles of Cocatalysts in Photocatalysis and Photoelectrocatalysis. *Acc. Chem. Res.*, *46*(8), 1900-1909.
13. Zhao, Z. (2014). Theoretical Study of Pt Cocatalyst Loading on Anatase  $\text{TiO}_2(101)$  Surface: From Surface Doping to Interface Forming. *J. Phys. Chem. C*, *118*(42), 24591-24602.
14. Sato, S., & White, J. M. (1981). Photoassisted Hydrogen Production from Titania and Water. *J. Phys. Chem.*, *12*(22).
15. Subramanian, V., Wolf, E., & Kamat, P. V. (2001). Semiconductor–Metal

- Composite Nanostructures. To What Extent Do Metal Nanoparticles Improve the Photocatalytic Activity of TiO<sub>2</sub> Films? *J. Phys. Chem. B*, 105(46), 11439-11446.
16. Jakob, M., Levanon, H., & Kamat, P. V. (2003). Charge Distribution between UV-Irradiated TiO<sub>2</sub> and Gold Nanoparticles: Determination of Shift in the Fermi Level. *Nano Lett.*, 3(3), 353-358.
  17. Sato, S., & White, J. (1980). Photodecomposition of water over Pt/TiO<sub>2</sub> catalysts. *Chem. Phys. Lett.*, 72(1), 83-86.
  18. Sclafani, A., Mozzanega, M., & Pichat, P. (1991). Effect of silver deposits on the photocatalytic activity of titanium dioxide samples for the dehydrogenation or oxidation of 2-propanol. *J. Photochem. Photobiol., A*, 59(2), 181-189.
  19. Wang, N., Tachikawa, T., & Majima, T. (2011). Single-molecule, single-particle observation of size-dependent photocatalytic activity in Au/TiO<sub>2</sub> nanocomposites. *Chem. Sci.*, 2(5), 891.
  20. Thomann, I., Pinaud, B. A., Chen, Z., Clemens, B. M., Jaramillo, T. F., & Brongersma, M. L. (2011). Plasmon Enhanced Solar-to-Fuel Energy Conversion. *Nano Lett.*, 11(8), 3440-3446.
  21. Yoshida, H., & Yamamoto, A. (2016). Photocatalytic activation of water with metal loaded photocatalysts prepared by a flux method. *Proceedings of the 1st International Symposium on Current Progress in Mathematics and Sciences*.
  22. Yoshida, H., Shimura, K. (2012). XAFS Study of Rhodium Cocatalyst Loaded on K<sub>2</sub>Ti<sub>6</sub>O<sub>13</sub> Photocatalyst. *Photon Factory Activity Report 2011*, 29, 40.
  23. Yoshida, H., Takeuchi, M., Sato, M., Zhang, L., Teshima, T., & Chaskar, M. G. (2014). Potassium hexatitanate photocatalysts prepared by a flux method for water splitting. *Catal. Today*, 232, 158-164.
  24. Shimura, K., Kawai, H., Yoshida, T., & Yoshida, H. (2012). Bifunctional Rhodium Cocatalysts for Photocatalytic Steam Reforming of Methane over Alkaline Titanate. *ACS Catal.*, 2(10), 2126-2134.
  25. Yoshida, H., Shimura, K. (2012). XAFS Study of Rhodium Cocatalyst Loaded on K<sub>2</sub>Ti<sub>6</sub>O<sub>13</sub> Photocatalyst. *Photon Factory Activity Report 2011*, 29, 40.
  26. Murata, H., Kataoka, Y., Kawamoto, T., Tanaka, I., & Taniguchi, T. (2014). Photocatalytic activity of α-PbO<sub>2</sub>-type TiO<sub>2</sub>. *Phys. Status Solidi RRL*, 8(10), 822-826.
  27. Sato, K., Kataoka, Y., & Mori, W. (2012). Photochemical Production of Hydrogen from Water Using Microporous Porphyrin Coordination Lattices. *J. Nanosci. Nanotechnol.*, 12(1), 585-590.
  28. Maeda, K. (2014). Rhodium-Doped Barium Titanate Perovskite as a Stable p-Type Semiconductor Photocatalyst for Hydrogen Evolution under Visible Light. *ACS Appl. Mater. Interfaces*, 6(3), 2167-2173.
  29. Okunaka, S., Tokudome, H., & Abe, R. (2015). Facile water-based preparation of Rh-doped SrTiO<sub>3</sub> nanoparticles for efficient photocatalytic H<sub>2</sub> evolution under visible light irradiation. *J. Mater. Chem. A*, 3(28), 14794-

14800.

30. Okunaka, S., Tokudome, H., & Abe, R. (2016). Structure-controlled porous films of nanoparticulate Rh-doped SrTiO<sub>3</sub> photocatalyst toward efficient H<sub>2</sub> evolution under visible light irradiation. *Catal. Sci. Technol.*, 6(1), 254-260.
31. Wang, Q., Hisatomi, T., Ma, S. S., Li, Y., & Domen, K. (2014). Core/Shell Structured La- and Rh-Codoped SrTiO<sub>3</sub> as a Hydrogen Evolution Photocatalyst in Z-Scheme Overall Water Splitting under Visible Light Irradiation. *Chem. Mater.*, 26(14), 4144-4150.
32. Nguyen, C., Dinh, C., & Do, T. (2017). Hollow Sr/Rh-codoped TiO<sub>2</sub> photocatalyst for efficient sunlight-driven organic compound degradation. *RSC Adv.*, 7(6), 3480-3487.

# Chapter 5

## Dye-sensitized Rh-doped Titanate Nanosheets and its Photocatalytic H<sub>2</sub> Production under Visible Light

### 5.1 Introduction

Artificial photosynthesis such as photo-induced H<sub>2</sub> production and CO<sub>2</sub> reduction has caught researchers' attention for many years. H<sub>2</sub> is considered as one of new promising energy resources that may replace the use of fossil fuel in the near future. Sunlight is expected as the source energy for producing H<sub>2</sub> from water. Thus, the photocatalyst with high efficiency under visible light irradiation is essential. The hybrid material of metal oxide semiconductor with photosensitizer is one of promising materials as a photocatalyst, which can be used under visible light irradiation.<sup>1-5</sup> The basic mechanism of the dye-sensitized photocatalytic reaction is preceded as follows: (1) dye molecule such as metal polypyridyl complexes adsorb the visible light. (2) The hot electrons produced by photoexcitation migrate from photoexcited dyes to the conduction band of metal oxide semiconductor; if the LUMO level of dye is higher than energy level of conduction band of metal oxide semiconductor. (3) This migrated electron can cause the photocatalytic water splitting reaction; if the energy level of conduction band of metal oxide semiconductor is higher than the reduction potential level of H<sup>+</sup>/H<sub>2</sub>. Moreover, the electron transfer yields from photoexcited dye to metal oxide semiconductor is one of the significant factors.<sup>6-10</sup>

Photocatalytic activity and efficiency depend on energy level of conduction band and reduction potential of H<sup>+</sup>/H<sub>2</sub>. Another important variable is an injection of electron from dye to metal oxide semiconductor. In order to increase the efficacy of electron injection, one of the methods is to enhance the binding between dye and metal oxide or dye adsorption should not occur only at the surface of metal oxide semiconductor. Consequently, both of them bind with the interaction i.e. electrostatic reaction because metal oxide semiconductor is in the form of layered material with ion-exchange properties which is a good material for based semiconductor. In addition, if semiconductor is a nano-scale material, the surface area for adsorbed dye molecule is increased; therefore, the reaction rate will also increase.<sup>11,12</sup> Accordingly, metal oxide nanosheet (such as titanate nanosheet) is an interesting material for building blocks of dye-sensitized photocatalyst

Many dye-sensitized semiconductors including layered and nanosheet were reported such as Ru(II) bipyridyl complex (Ru(bpy)<sub>3</sub><sup>2+</sup>) dye-sensitized K<sub>2</sub>Nb<sub>3</sub>O<sub>7</sub>, Ru(bpy)<sub>3</sub><sup>2+</sup> dye-

sensitized niobite nanosheet.<sup>13,14</sup> Previously, reported systems of dye-sensitized photocatalyst are all required cocatalyst to aid in the reduction of water molecule for the reaction to progress smoothly and decrease  $e^-/h^+$  recombination or increase life-time of photogenerated  $e^-/h^+$  separation. Cocatalyst is also an important part of the system of dye-sensitized photocatalyst.<sup>15-21</sup> Although, cocatalyst will not directly affect the visible light absorption ability, cocatalyst as a part of the system makes the analysis of the main catalyst to be difficult. Hence, the study of each catalyst's properties should not include cocatalyst in the system.

In the previous chapter, photocatalytic activity of Rh-doped titanate nanosheet in the photocatalytic  $H_2$  production was discussed. The results showed that Rh doping enhance the efficacy of photocatalytic  $H_2$  production without the aid of cocatalyst loading. Even though, Rh-doped titanate nanosheet still responds only UV light, but it can be used as a building block of dye-sensitized semiconductor photocatalyst without the needs to use cocatalyst. Thus, the using of Rh-doped titanate nanosheet as a building block of dye-sensitized semiconductor photocatalyst is a better approach to investigate the photocatalytic activity only occurred from sensitizer dye and semiconductor.

LUMO level of dye is a key factor in choosing a dye as a light acceptor in the dye-sensitized photocatalyst since it has to be more negative than conduction band of semiconductor. In this research, two inorganic and organic dyes are chosen as models which are Ir(III) 2-phenylpyridine, 2,2'-bipyridine [ $Ir(ppy)_2(bpy)^+$ ] as an inorganic dye<sup>23-29</sup> and  $\alpha$ ,  $\beta$ ,  $\gamma$ ,  $\delta$ -tetrakis(1-methylpyridinium-4-yl)porphyrin (TMPyP) as an organic dye.<sup>30</sup> Both dyes have LUMO level higher than conduction band of our synthesized Rh-doped titanate nanosheet. The differences between  $Ir(ppy)_2(bpy)^+$  and TMPyP are chemical structure. Additionally,  $Ir(ppy)_2(bpy)^+$  is based on metal ligand complex with the ability as a catalyst, despite its ability is not high compared to metal oxide semiconductor. While TMPyP is a free ligand as shown in figure 5.1. Generally, TMPyP does not show a photocatalyst property especially in the production of  $H_2$ .

Dye-sensitized photocatalyst by Rh-doped titanate nanosheet which exfoliated from  $H_2Ti_{3-x}Rh_xO_7$  where x is doped amount, and use  $Ir(ppy)_2(bpy)^+$  dye and/or TMPyP dye are used in this chapter. This chapter covers the preparation of dye-sensitized Rh-doped titanate nanosheet on both structure and light properties. The photocatalytic activity of prepared dye-sensitized Rh-doped titanate nanosheet for  $H_2$  production was investigated by using TEA as an electron donor.

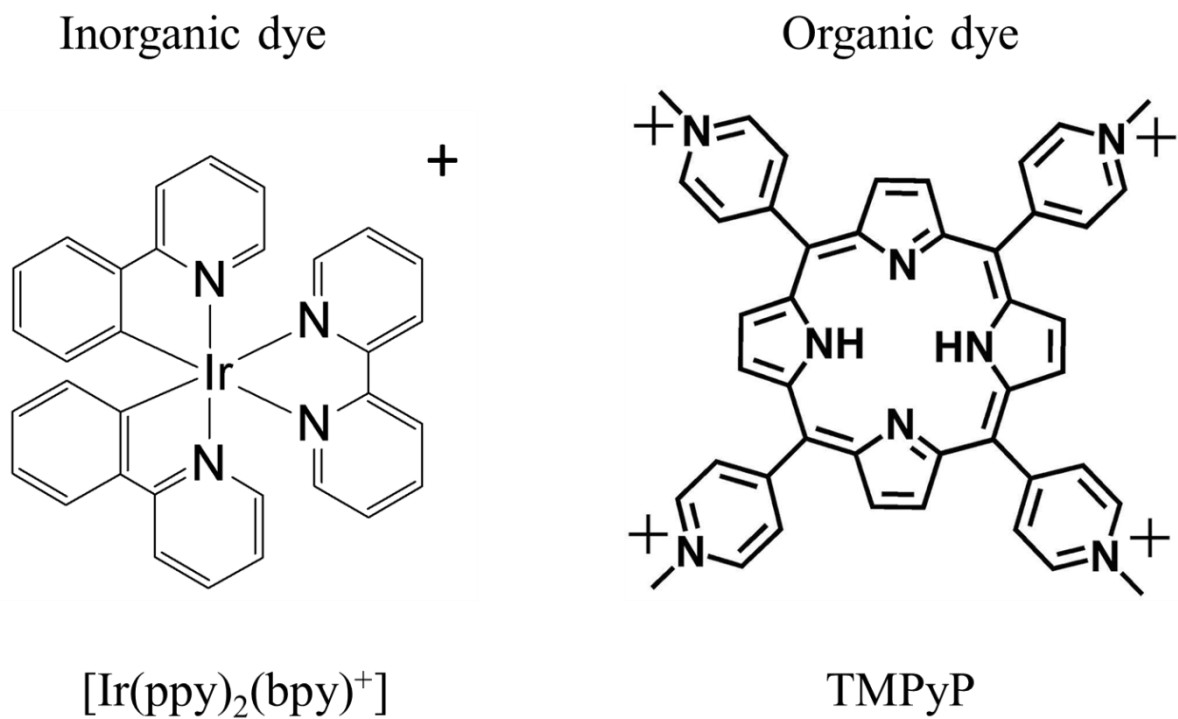


Figure 5.1 Chemical structure of  $[\text{Ir}(\text{ppy})_2(\text{bpy})^+]$  and TMPyP dye.

## 5.2 Experimental

### *Materials*

Sodium carbonate  $\text{Na}_2\text{CO}_3$  (99.9%) from Wako Pure Chemical Industries Co., anatase-type  $\text{TiO}_2$  (99.7%) from High Purity Chemicals Co.,  $\text{Rh}_2\text{O}_3$  (99.9%) from Wako Pure Chemical Industries Co., tetramethylammonium hydroxide (TMAOH, 26wt.% solution) from Tokyo Chemical Industry Co., and triethylamine ( $\text{N}(\text{CH}_2\text{CH}_3)_3$ , TEA) from Wako Pure Chemical Industries Co., were used without further purification.

### *Preparation of the dye-sensitized Rh-doped titanate nanosheets<sup>13-15,17,19</sup>*

The colloidal suspension of  $\text{Ti}_3\text{NS:Rh}_x$  ( $[\text{Ti}_{3-x}\text{Rh}_x\text{O}_7]^{2-}$ ) was prepared as described in previous chapter. The dye-sensitized  $\text{Ti}_3\text{NS:Rh}_x$  was prepared by mixing a  $\text{Ir}(\text{ppy})_2(\text{bpy})^+$  dye or TMpyP with  $\text{Ti}_3\text{NS:Rh}_x$  colloidal suspension for 24 hours protected from any lights to let  $\text{Ti}_3\text{NS:Rh}_x$  adsorbed dye molecules. After 24 hours, the mixed solution was washed by distill water dyes and filtrated by using a hydrophilic polyfluoro resin membrane filter (pore size = 0.1  $\mu\text{m}$ ) to remove non-adsorbed, then a collected powder were dried in vacuum overnight.

### *H<sub>2</sub> evolution experiment<sup>31,32</sup>*

All photochemical reactions were performed in a closed gas circulation system with a Pyrex reaction cell. The reaction solution (10  $\text{cm}^3$ ) containing TEA (0.36  $\text{mol}/\text{dm}^3$ ) and dye-sensitized  $\text{Ti}_3\text{NS:Rh}_x$  (10 mg) was degassed by repeated freeze pump-thaw cycles. The reaction solution was shifted into the reaction vessel with a glove box under an Ar-saturated atmosphere. The reaction solution was irradiated at 300 K using a 500 W Xe lamp (USHIO Co.) equipped with optical cut-off filters (short pass filter  $\lambda < 220$ ,

and long pass filter  $\lambda > 340$ ,  $\lambda > 380$ , and  $\lambda > 480$  nms, Kenko Co.). The amount of evolved  $H_2$  gas was determined using a gas chromatograph (Shimadzu; GC-8A with TCD detector, a stainless-steel column packed with molecular sieves-5A, and ultra-pure Ar carrier gas). All measurements were performed under non-oxygen conditions.

### *Characterization*

To analyze crystal structure of all materials, the powder X-ray diffraction (XRD) analysis was carried out by X-ray diffractometer (RIGAKU, MiniFlex II). Absorption spectra of various samples were measured by UV-Vis spectrophotometer (V-670 UV-VIS-NIR spectrophotometer, JASCO). Absorption spectra of liquid samples were measured by transmission mode. Diffuse reflectance (DR) spectra of solid sample were measured by UV-Vis spectrophotometer attached to an integrating sphere system (ISN-723, JASCO). Doped and loaded amount of Rh in and Rhx-Ti3NS was estimated by ICP-AES apparatus (Optima2000DV, Perkinelmer). Scanning electron microscopy imaging was performed using JEOL-7001FA (JEOL Ltd.) operated at 12 kV.

## **5.3 Result and Discussion**

### *Dye-sensitized Ti3NS:Rh<sub>x</sub>, its physical and optical properties*

Figure 5.2 shows the photo of Ti3NS:Rh<sub>x</sub> powder before and after adsorbed  $Ir(ppy)_2(bpy)^+$  and TMPyP dyes. In the case of  $Ir(ppy)_2(bpy)^+$ , Ti3NS:Rh0 powder changed from white to yellow, thus this indicates that  $Ir(ppy)_2(bpy)^+$  was adsorbed by Ti3NS:Rh0 powder. Meanwhile, Ti3NS:Rh0 white colloidal became red powder when TMPyP was adsorbed. As for Ti3NS:Rh0.03, the powder already has yellowish orange color which makes it difficult to spot the color alteration.

The adsorption maximum of  $Ir(ppy)_2(bpy)^+$  and TMPyP was measured from the isothermal curve plotted between  $C^{add}$ , which a ratio of  $Ir(ppy)_2(bpy)^+$  or TMPyP molecule per Ti3NS molecule in a mol/mol unit and  $C^{ads}$ , which a ratio of adsorbed  $Ir(ppy)_2(bpy)^+$  or TMPyP molecule per Ti3NS molecule in a mol/mol unit (figure 5.3 and 5.4). According to this graph, Ti3NS:Rh0 could adsorb  $Ir(ppy)_2(bpy)^+$  at maximum about 4.5% (mol/mol) and TMPyP dye at maximum 17% (mol/mol). While Ti3NS:Rh0.03 has maximum adsorption value for TMPyP slightly less than Ti3NS:Rh0. This can be referred to Chapter 3 for adsorption of MB dye. However, the maximum adsorption for  $Ir(ppy)_2(bpy)^+$  did not exhibit a considerable difference between Ti3NS:Rh0 and Ti3NS:Rh0.03. The dye-sensitize Ti3NS:Rh<sub>x</sub> was set at  $Ir(ppy)_2(bpy)^+$

with the amount of 4.5% mol of Ti3NS:Rh<sub>x</sub>, while TMPyP with the amount of 17% mol of Ti3NS:Rh<sub>x</sub>.

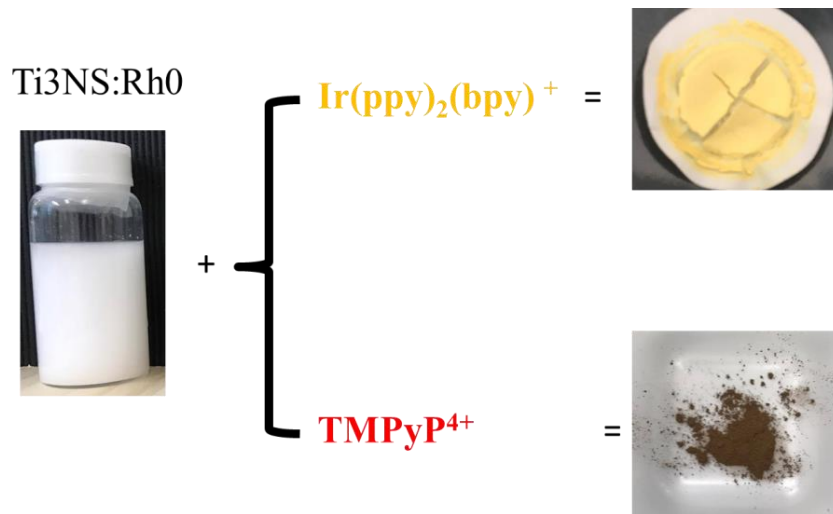


Figure 5.2 The picture of Ti3NS:Rh0 colloidal suspension and the powder obtained after mixed with  $\text{Ir(ppy)}_2(\text{bpy})^+$  and/or TMPyP dye.

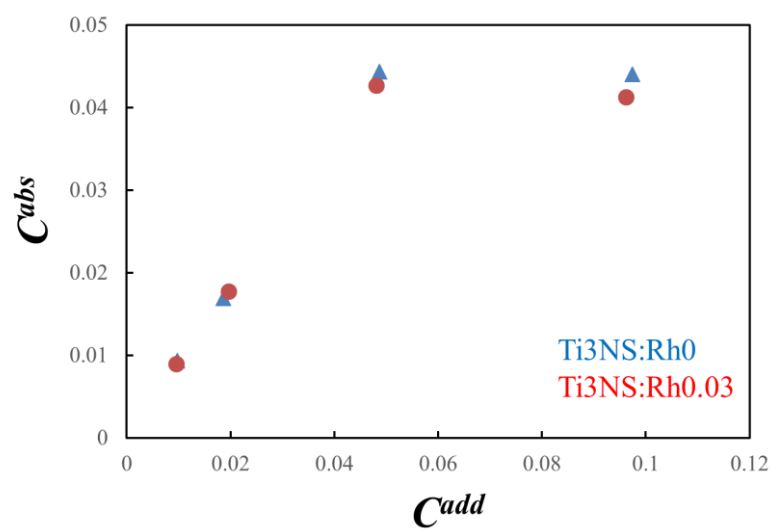


Figure 5.3 The adsorption isothermal curves of Ir(ppy)<sub>2</sub>(bpy)<sup>+</sup> by Ti3NS:Rh<sub>x</sub>.

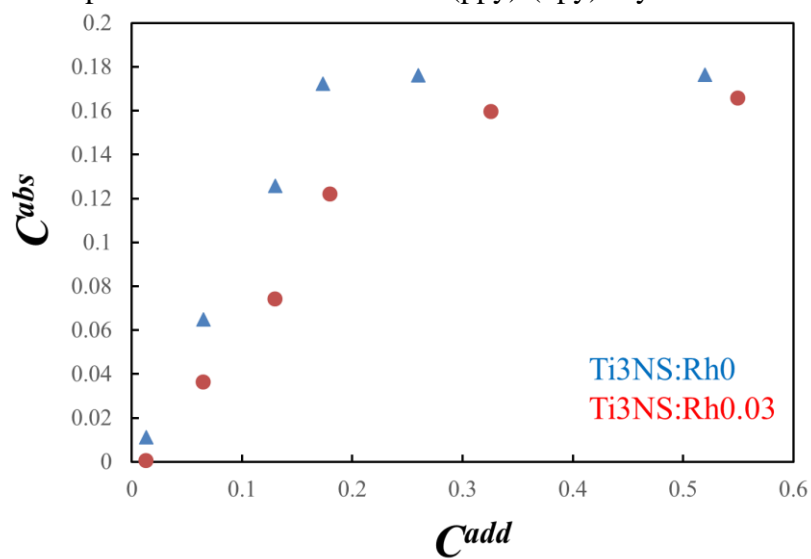


Figure 5.4 The adsorption isothermal curves of TMPyP by Ti3NS:Rh<sub>x</sub>.

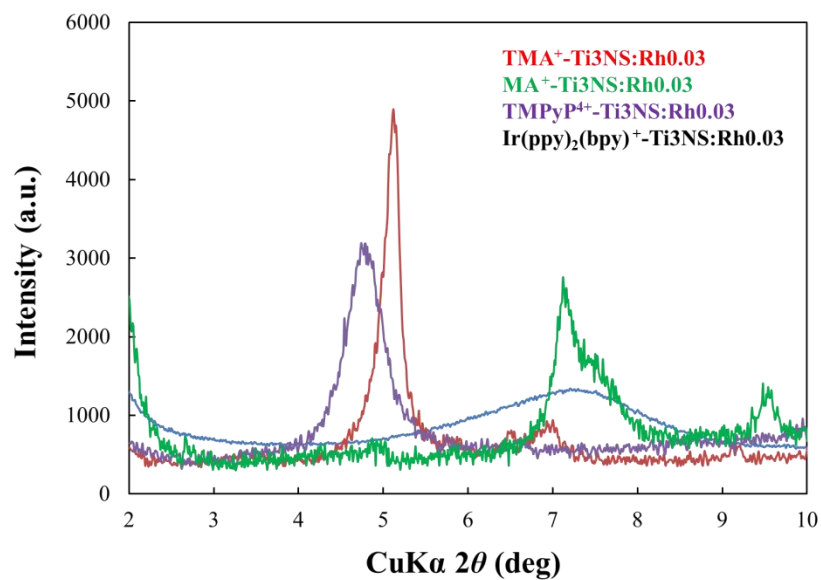


Figure 5.4 The XRD pattern of dye-sensitized Ti3NS:Rh0.03 powder and powder of Ti3NS:Rh0.03 intercalated by TMA<sup>+</sup> and MA<sup>+</sup> ion.

Figure 5.4 displays XRD pattern of Ti3NS:Rh<sub>x</sub> powder before and after adsorbed TMPyP or Ir(ppy)<sub>2</sub>(bpy)<sup>+</sup> dye. Before the adsorption of Ir(ppy)<sub>2</sub>(bpy)<sup>+</sup> or TMPyP dye, XRD pattern exhibited the pattern of Ti3NS intercalated by tetramethylammonium ion (TMA<sup>+</sup>) which was used in the exfoliation process (Figure 5.3). The diffraction peak at about 5° originated from *d*<sub>200</sub> plane can be observed. This reveals that after the adsorption of Ir(ppy)<sub>2</sub>(bpy)<sup>+</sup> dye; *d*<sub>200</sub> diffraction peak was shifted into higher angle about 7.5°. However, this result was not reasonable with the molecular structure of Ir(ppy)<sub>2</sub>(bpy)<sup>+</sup>. Generally, Ir(ppy)<sub>2</sub>(bpy)<sup>+</sup> has a Ir ion at the center of molecule surrounded with bipyridine and phenylpyridine. This bipyridine and phenylpyridine making Ir(ppy)<sub>2</sub>(bpy)<sup>+</sup> become a large rigid structure. Thus, if the Ir(ppy)<sub>2</sub>(bpy)<sup>+</sup> was aligned in the interlayer spacing of Ti3NS, it would cause Ir(ppy)<sub>2</sub>(bpy)<sup>+</sup> situated in the interlayer spacing of Ti3NS. It has only one option due to the Ir(ppy)<sub>2</sub>(bpy)<sup>+</sup> ion was bigger than TMA<sup>+</sup>; theoretically, the interlayer spacing of Ti3NS:Rh<sub>x</sub> should be expanded and we should observed the low-angle shifted instead of the higher-angle shifted. The question is the cause behinds the representation of diffraction peak at 7.5°. This can be explained by the exfoliation method of Ti3NS:Rh<sub>x</sub>. Before Ti3NS:Rh<sub>x</sub> was dispersed and exfoliated in TMAOH solution, the methylammonium ion (MA<sup>+</sup>) have been intercalated in the interlayer spacing of Ti3NS:Rh<sub>x</sub>. The diffraction peak of MA<sup>+</sup> intercalated Ti3NS:Rh<sub>x</sub> was observed about 7.5° which appropriate with the diffraction peak of Ir(ppy)<sub>2</sub>(bpy)<sup>+</sup> dye-sensitized Ti3NS:Rh<sub>x</sub>. This indicated that Ir(ppy)<sub>2</sub>(bpy)<sup>+</sup> did not exist in the interlayer spacing of Ti3NS:Rh<sub>x</sub>. However, we could observe the color powder change. Thus, it has a possibility that Ir(ppy)<sub>2</sub>(bpy)<sup>+</sup> have been adsorbed on the surface of Ti3NS:Rh<sub>x</sub>. In contrast, when TMPyP was adsorbed; it caused the diffraction peak of *d*<sub>200</sub> plane shifted toward lower angle. TMPyP also replaced TMA<sup>+</sup> in the interlayer spacing of Ti3NS.

In the case of TMPyP (figure 5.1), structure of TMPyP is composed of rigid, square-planar made of 5 pyrroles as bases and the four branches are methyl-peridyl group with nitrogen atom position of cationic charge.<sup>27,29,30</sup> The possibility in which TMPyP intercalated into interlayer spacing of Ti3NS is varied; for example, the two branches contracted with an anionic charge at the surface of Ti3NS sheet on the top and bottom, and another case is that TMPyP dovetailed on top and bottom with four branches attached to the sheet. In the previous case, the size of TMPyP was larger than TMA<sup>+</sup> resulted in the extended of interlayer spacing. In latter case, the interlayer spacing should be imposed by the thickness of TMPyP molecule which made the interlayer of Ti3NS sheet to sheet contracted more or the interlayer spacing should become narrower or equal to that of TMA<sup>+</sup> intercalated Ti3NS. Therefore, this may due to two branches of TMPyP molecule attached at the top and the other two at the bottom.

Figure 5.5 and 5.6 show the adsorption spectra of Ir(ppy)<sub>2</sub>(bpy)<sup>+</sup> solution and TMPyP solution compared with the diffuse reflection spectra of dye-sensitized Ti3NS:Rh<sub>x</sub>, respectively. As for Ir(ppy)<sub>2</sub>(bpy)<sup>+</sup>, the adsorption spectra show the maximum peak at 253 nm and the adsorption ranges from 200-420 nm which relates to Ir ion in Ir(ppy)<sub>2</sub>(bpy)<sup>+</sup>. When Ir(ppy)<sub>2</sub>(bpy)<sup>+</sup> was adsorbed by Ti3NS:Rh<sub>x</sub>, the adsorption band of Ir(ppy)<sub>2</sub>(bpy)<sup>+</sup> dye-sensitized Ti3NS:Rh<sub>x</sub> increased only one adsorption band of Ir(ppy)<sub>2</sub>(bpy)<sup>+</sup>. In the case of Ir(ppy)<sub>2</sub>(bpy)<sup>+</sup> dye-sensitized Ti3NS:Rh<sub>0.03</sub>, formerly Ti3NS:Rh<sub>0.03</sub> showed the adsorption spectra of λ < 600 nm; hence, it is difficult to observe the alteration of adsorption spectra and color of powder.



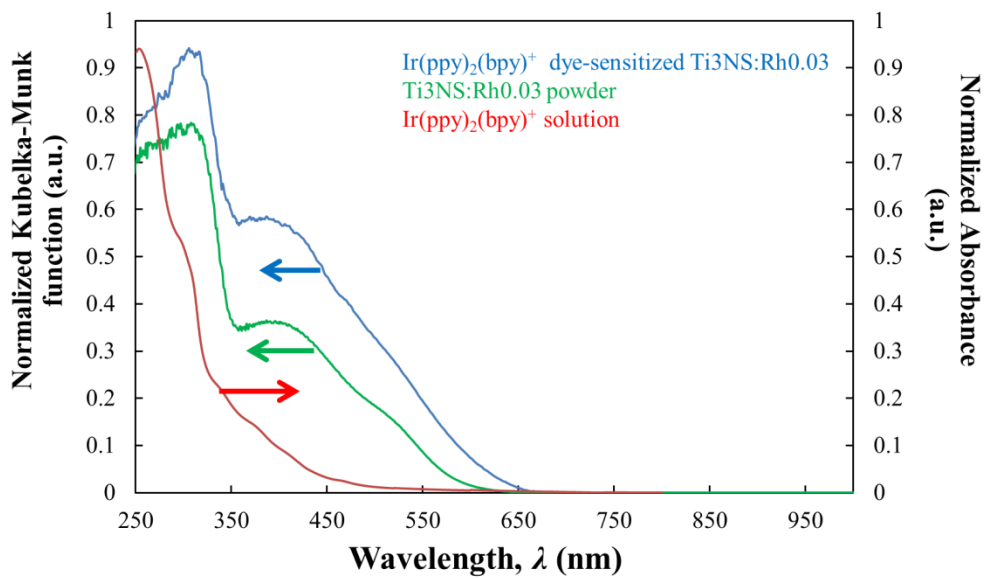


Figure 5.5 The diffuse reflectance spectra of Ti3NS:Rh0.03 before and after mixed with Ir(ppy)<sub>2</sub>(bpy)<sup>+</sup> and the absorption spectra of Ir(ppy)<sub>2</sub>(bpy)<sup>+</sup> solution.

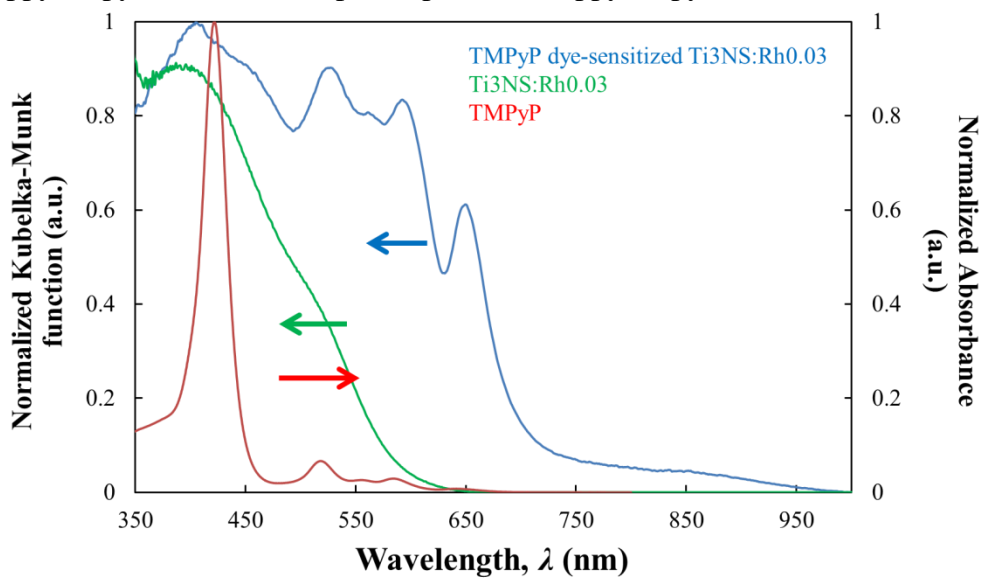


Figure 5.6 The diffuse reflectance spectra of Ti3NS:Rh0.03 before and after mixed with TMPyP and the absorption spectra of TMPyP solution.

As for TMPyP dye-sensitized Ti3NS:Rh<sub>x</sub>, adsorption spectra of powder clearly displayed the adsorption peak at  $\lambda$  about 434 nm. The adsorption peak corresponded with the sorb adsorption of TMPyP. The comparison of sorb adsorption of TMPyP in solution and TMPyP dye-sensitized showed that peak shifted from 424 nm to 434 nm. This can be elucidated by TMPyP intercalated in the interlayer spacing of Ti3NS:Rh<sub>x</sub> affecting the degree of freedom of TMPyP to change. Normally, the value of TMPyP is dependent on the wavelength of sorb adsorption as the environment changes. At first, TMPyP in the solution is in the ion state and surrounded by water molecule. This made the branches of pyridyl of TMPyP in the free state causing sorb adsorption to has lower wavelength.<sup>33-35</sup> On the other hand, when TMPyP is in the interlayer spacing of Ti3NS:Rh<sub>x</sub>; all four branches could not move freely and the surrounded molecules changed from water molecule to Ti3NS sheet resulted in sorb adsorption shift to higher wavelength.

Nonetheless, dye-sensitized Ti3NS:Rh<sub>x</sub> either Ir(ppy)<sub>2</sub>(bpy)<sup>+</sup> or TMPyP showed the adsorption band in the range of  $\lambda \geq 400\text{nm}$ . Thus, Ir(ppy)<sub>2</sub>(bpy)<sup>+</sup> dye sensitized Ti3NS:Rh<sub>x</sub> and TMPyP dye-sensitized Ti3NS:Rh<sub>x</sub> has a tendency to be used as photocatalyst under visible light for H<sub>2</sub> production.

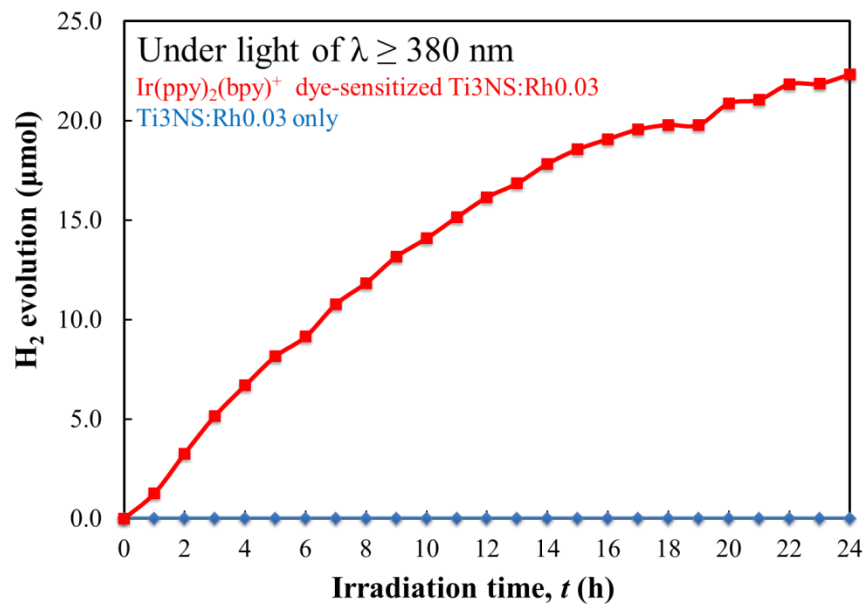


Figure 5.7 The  $H_2$  evolution by  $\text{Ir(ppy)}_2(\text{bpy})^+$  dye-sensitized  $\text{Ti3NS:Rh0.03}$  and only  $\text{Ti3NS:Rh0.03}$  plotted with irradiation time by using UV light ( $\lambda \geq 380$  nm).

### *H<sub>2</sub> production by dye-sensitized Ti3NS:Rh<sub>x</sub> under visible light irradiation*

Figure 5.7 exhibits H<sub>2</sub> evolution plotted against irradiation time from Ir(ppy)<sub>2</sub>(bpy)<sup>+</sup> dye-sensitized Ti3NS:Rh by using light of  $\lambda \geq 380$  nm. Ir(ppy)<sub>2</sub>(bpy)<sup>+</sup> dye-sensitized Ti3NS:Rh<sub>0</sub> does not show H<sub>2</sub> evolution under light of  $\lambda \geq 380$  nm while Ir(ppy)<sub>2</sub>(bpy)<sup>+</sup> dye-sensitized Ti3NS:Rh<sub>0.03</sub> exhibited H<sub>2</sub> evolution. Normally, either Ti3NS:Rh<sub>0</sub> or Ti3NS:Rh<sub>0.03</sub> cannot be used as a photocatalyst for hydrogen evolution under light  $\lambda \geq 380$  nm (see chapter 4). In contrast, Ir(ppy)<sub>2</sub>(bpy)<sup>+</sup> has a photocatalytic hydrogen evolution ability, even though, the capability is low at  $\lambda \geq 380$  nm.

Nevertheless, H<sub>2</sub> evolution cannot be observed in Ir(ppy)<sub>2</sub>(bpy)<sup>+</sup> dye-sensitized Ti3NS:Rh<sub>0</sub> as shown in Figure 5.8. While Ir(ppy)<sub>2</sub>(bpy)<sup>+</sup> dye sensitized Ti3NS:Rh<sub>0.03</sub> showed H<sub>2</sub> evolution at  $\lambda \geq 380$  nm and H<sub>2</sub> evolution rate at 24 hours; the value is relatively similar to H<sub>2</sub> evolution rate of Ti3NS:Rh<sub>0.03</sub> when irradiated under UV  $\lambda < 220$  nm. This denotes that Ir(ppy)<sub>2</sub>(bpy)<sup>+</sup> functions or adsorbs light  $\lambda \geq 380$  nm, and Ti3NS:Rh<sub>x</sub> acts as a reaction center of photocatalytic H<sub>2</sub> evolution reaction.

The energy level of LUMO of Ir(ppy)<sub>2</sub>(bpy)<sup>+</sup> and conduction band of Ti3NS were analyzed; the result implies that LUMO has quite higher value than conduction band (Figure 5.9). This concludes that Ir(ppy)<sub>2</sub>(bpy)<sup>+</sup> acted as light adsorber and excited the photoexcited electron; electron injected to conduction band of Ti3NS to use in the H<sub>2</sub> evolution with TEA as electron donor for Ir(ppy)<sub>2</sub>(bpy)<sup>+</sup>. Although, Ti3NS:Rh<sub>0</sub> does not exhibit any H<sub>2</sub> evolution because the photocatalyst ability for H<sub>2</sub> evolution of Ti3NS:Rh<sub>0</sub> is extremely low. According to Chapter 4, we can conclude that Rh-doping enhances the capability of Ti3NS as a photocatalyst for H evolution due to the electron pool of Rh<sup>3+</sup>. Consequently, when it binds with Ir(ppy)<sub>2</sub>(bpy)<sup>+</sup>, Ir(ppy)<sub>2</sub>(bpy)<sup>+</sup> will send electron to Ti3NS: Rh<sub>0.03</sub> which collects all the photogenerated electron from Ir(ppy)<sub>2</sub>(bpy)<sup>+</sup> and continues the reaction.

On the other hand, TMPyP dye-sensitized Ti3NS:Rh<sub>x</sub> either  $x = 0$  or  $x = 0.03$  does not display any photocatalyst for H<sub>2</sub> evolution under light of  $\lambda \geq 380$  nm (figure 5.10). This divulges that e<sup>-</sup> may not be injected from LUMO of TMPyP to conduction band of Ti3NS, although, the light energy is enough to excite TMPyP to generate excited electron. This may also imply that electron can be injected from LUMO of TMPyP to conduction band of Ti3NS but TMPyP cannot accept any donor electrons from TEA. As a result, when TMPyP is excited and electrons transfer from TMPyP to Ti3NS. This makes TMPyP in the oxidized state at all times because it cannot accept any e<sup>-</sup> from donor atom.

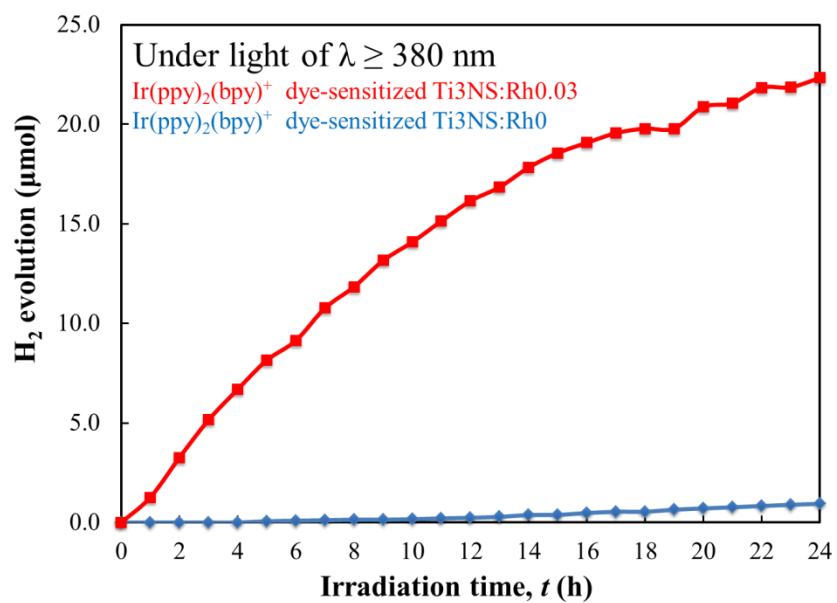


Figure 5.8 The  $\text{H}_2$  evolution by  $\text{Ir}(\text{ppy})_2(\text{bpy})^+$  dye-sensitized  $\text{Ti3NS:Rh0}$  and  $\text{Ir}(\text{ppy})_2(\text{bpy})^+$  dye-sensitized  $\text{Ti3NS:Rh0.03}$  plotted with irradiation time by using UV light ( $\lambda \geq 380$  nm).

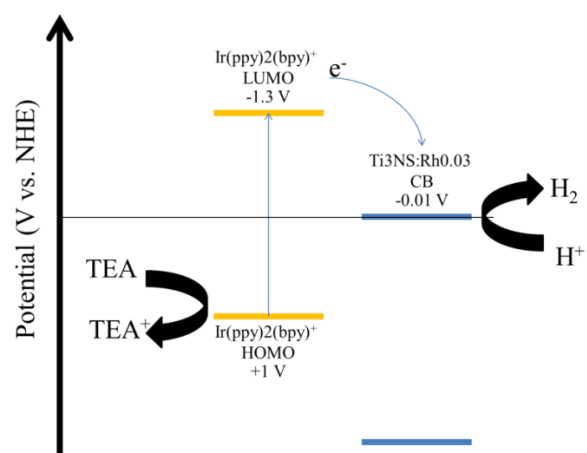


Figure 5.9 The schematic diagram of photocatalytic reaction of Ir(ppy)<sub>2</sub>(bpy)<sup>+</sup> dye-sensitized Ti<sub>3</sub>NS:Rh<sub>0.03</sub>, the electrons transfer from Ir(ppy)<sub>2</sub>(bpy)<sup>+</sup> to Ti<sub>3</sub>NS:Rh<sub>0.03</sub> can occur under visible light irradiation.

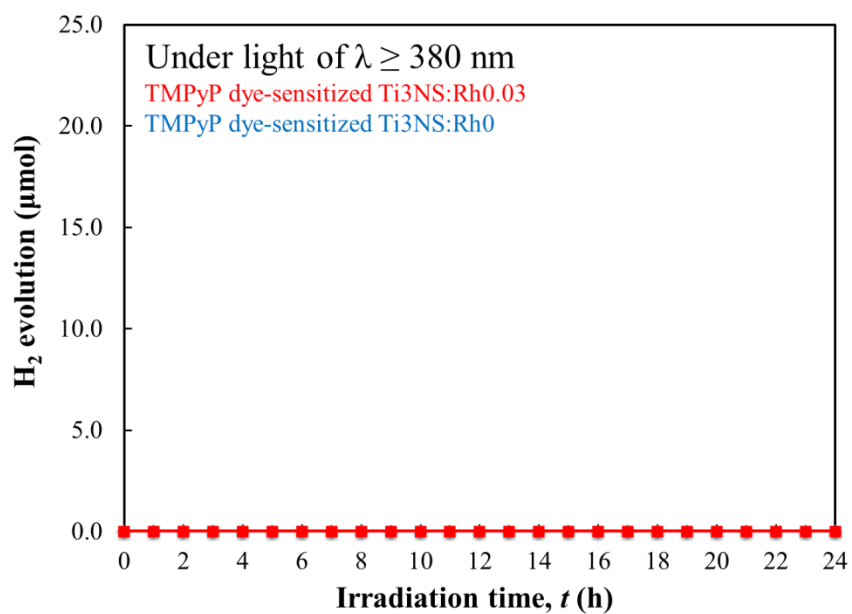


Figure 5.10 The H<sub>2</sub> evolution by TMPyP dye-sensitized Ti3NS:Rh0 and TMPyP dye-sensitized Ti3NS:Rh0.03 plotted with irradiation time by using UV light ( $\lambda \geq 380$  nm).

In order to observe electron transfer between TMPyP and Ti3NS, we measured the photoluminescence. The measurement was done by dispersing the TMPyP dye-sensitized Ti3NS:Rh<sub>x</sub> in TEA solution with the same condition as the photocatalytic H<sub>2</sub> evolution experiment. The N<sub>2</sub> gas bubbling was done to remove O<sub>2</sub> gas from TEA solution. Figure 5.11 shows the emission spectra from TMPyP dye-sensitized Ti3NS:Rh<sub>0</sub> under visible light and UV light ( $400 \leq \lambda \leq 450$  nm) which corresponds with the adsorption band of TMPyP, and light adsorption of Ti3NS was avoided. From these results, emission spectrums were observed around  $\lambda = 675$  nm. The emission spectrum can be found in the case of TMPyP solution or hybrid system with clay material. This suggests that excited electrons in TMPyP did not inject to conduction band of Ti3NS but release energy in the form of fluorescence and went back from LUMO to HOMO.<sup>36-</sup>  
<sup>39</sup> Electron transfer requires longer life time of excited electrons; therefore, electrons was at ground state instead of transferring from LUMO of TMPyP to conduction band of Ti3NS while releasing energy in the form of fluorescence light (figure 5.13). Accordingly, TMPyP dye sensitized Ti3NS:Rh<sub>x</sub> is not suitable for a photocatalyst in the H<sub>2</sub> evolution reaction.

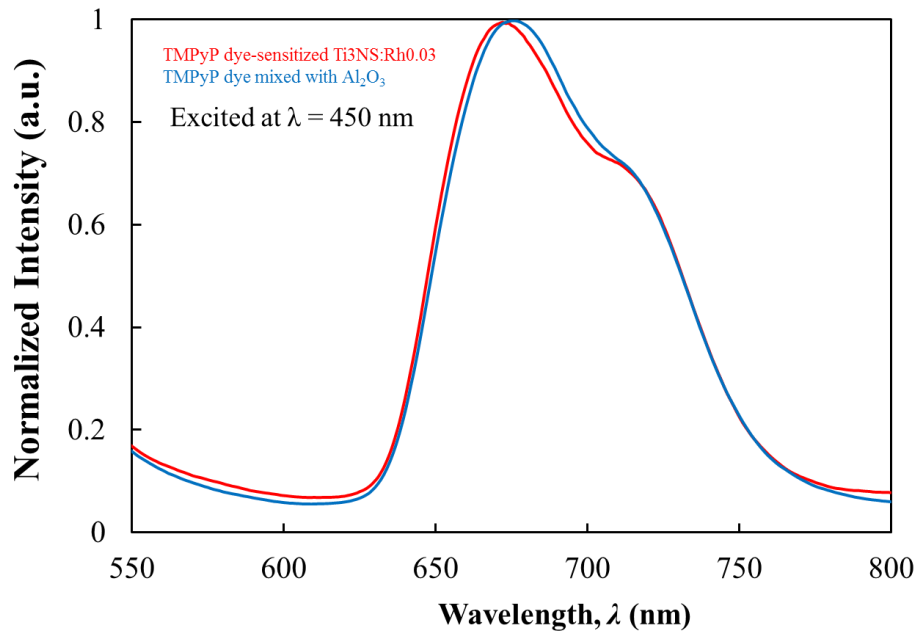


Figure 5.12 The emission spectra for TMPyP dye-sensitized Ti3NS:Rh0.03 with 450 nm excitation, along with that of TMPyP/Al<sub>2</sub>O<sub>3</sub> for reference.

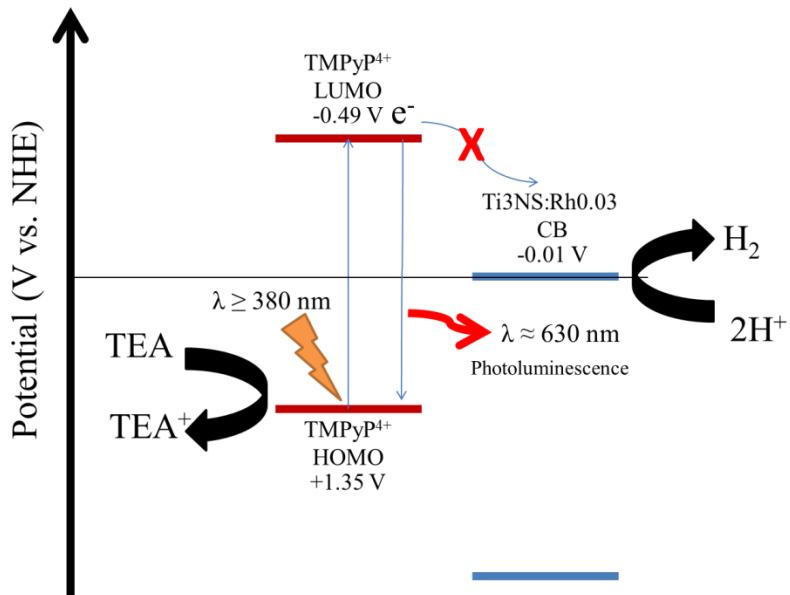


Figure 5.9 The schematic diagram of photocatalytic reaction of TMPyP dye-sensitized Ti3NS:Rh0.03, the electrons transfer from TMPyP to Ti3NS:Rh0.03 cannot occur under visible light irradiation, but it exhibits the photoluminescence which cause by the excited electron.

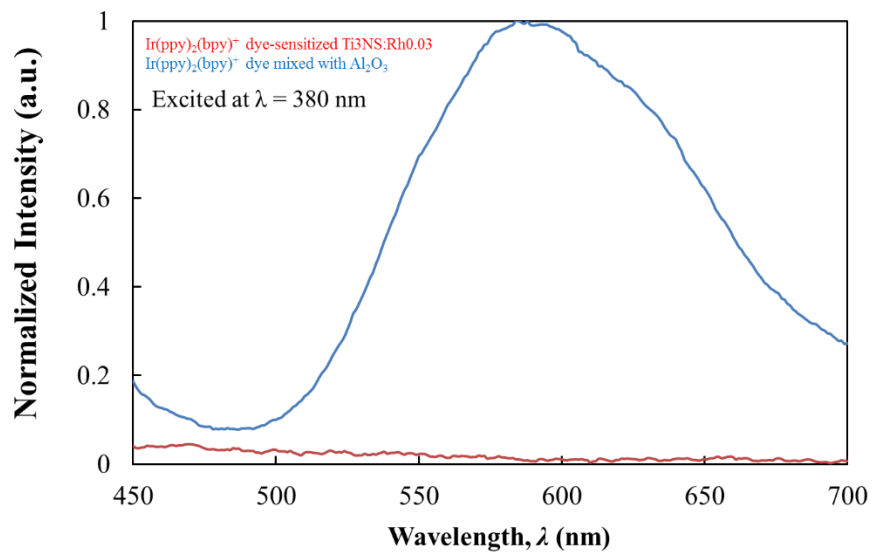


Figure 5.13 The emission spectra for Ir(ppy)<sub>2</sub>(bpy)<sub>3</sub><sup>+</sup> dye-sensitized Ti<sub>3</sub>NS:Rh0.03 with 380 nm excitation, along with that of Ir(ppy)<sub>2</sub>(bpy)<sub>3</sub><sup>+</sup>/Al<sub>2</sub>O<sub>3</sub> for reference.

Moreover,  $\text{Ir(ppy)}_2(\text{bpy})^+$  dye-sensitized  $\text{Ti3NS:Rh}_x$  was also measured the photoluminescence properties. The results are shown in figure 5.13.  $\text{Ir(ppy)}_2(\text{bpy})^+$  dye-sensitized  $\text{Ti3NS:Rh}_x$  did not exhibit any photoluminescence when irradiated at  $\lambda$  from 380 nm. Generally,  $\text{Ir(ppy)}_2(\text{bpy})^+$  dye can exhibit a photoluminescence when the light was fit to the ligand to ligand charge transfer (LLCT) which is about 355 nm. The coupling between LLCT and the metal-ligand charge transfer state will occur, and excited electron will slowly relax and back to ground state. The relaxation will take a long time about 0.5-2  $\mu\text{s}$ .<sup>24,40</sup> This relaxation time is longer than the electron injection, theoretically. The comparison between the photoluminescence of  $\text{Ir(ppy)}_2(\text{bpy})^+$  dye with and without  $\text{Ti3NS:Rh}_x$ , we measured the photoluminescence of  $\text{Ir(ppy)}_2(\text{bpy})^+$  dye mixed  $\text{Al}_2\text{O}_3$ . The result shows that under 380 nm light irradiation the photoluminescence can be observed noticeably at about 500-600 nm from  $\text{Ir(ppy)}_2(\text{bpy})^+$  dye mixed  $\text{Al}_2\text{O}_3$ . This shows that there is a possibility that electron will transfer from LUMO of  $\text{Ir(ppy)}_2(\text{bpy})^+$  to conduction band of  $\text{Ti3NS}$  corresponded with the energy structure in which LUMO is excessively higher than conduction band level. Theoretically, there is a high possibility which electrons will jump from higher energy level to lower energy level. Likewise, the possibility is high because electron has to release energy.

In the case of  $\text{TMPyP}$ , electron chose to move back to ground state rather than to the conduction and of  $\text{Ti3NS}$ . In contrast, excited electron in  $\text{Ir(ppy)}_2(\text{bpy})^+$  chose to jump to the conduction band of  $\text{Ti3NS}$ . The electrons can be transferred when LUMO is higher than conduction band and when there are differences between LUMO level and conduction band level

Besides dye is necessary for visible light absorption, Rh-doping is also vital for this system. This can be seen  $\text{Ir(ppy)}_2(\text{bpy})^+$  dye sensitized  $\text{Ti3NS:Rh0}$  cannot produced  $\text{H}_2$ . In the case of only  $\text{Ir(ppy)}_2(\text{bpy})^+$ ,  $\text{Ir(ppy)}_2(\text{bpy})^+$  dye can act as a photocatalyst for  $\text{H}_2$  production but the reaction can occur for a short time due to self-decomposition. As for  $\text{Ir(ppy)}_2(\text{bpy})^+$  dye-sensitized  $\text{Ti3NS:Rh0}$ ,  $\text{H}_2$  cannot be measured implying that electrons were sent to  $\text{Ti3NS}$  but the reaction cannot occur without the aid of doping Rh at Ti site. From these results, they strongly demonstrated that Rh doping can be used instead of cocatalyst, and we could construct a simple dye-sensitized photocatalyst without any cocatalyst.

#### 5.4 Conclusion

In this chapter, we demonstrated the preparation of dye-sensitized titanate nanosheet, their photo properties, and photocatalytic activity for  $\text{H}_2$  evolution under visible light. Both of inorganic and organic dyes were used as a photoreceptor in the dye-sensitized system.  $\text{Ir(ppy)}_2(\text{bpy})^+$  dye was used as a representative of inorganic dye, while  $\text{TMPyP}$  was used as a representative of organic dye. The XRD result indicated that  $\text{Ir(ppy)}_2(\text{bpy})^+$  dyes were adsorbed on the surface of  $\text{Ti3NS:Rh}_x$ , while  $\text{TMPyP}$  dyes were adsorbed and intercalated in the interlayer spacing of  $\text{Ti3NS:Rh}_x$ . The photocatalytic  $\text{H}_2$  evolution could be found only the  $\text{Ir(ppy)}_2(\text{bpy})^+$  dye-sensitized  $\text{Ti3NS:Rh0.03}$ . The  $\text{TMPyP}$  dye-sensitized  $\text{Ti3NS:Rh0.03}$  did not display any photocatalytic activity because it exhibited the photoluminescence under visible light irradiation which resulting in no electron transferring from LUMO of  $\text{TMPyP}$  to conduction band of  $\text{Ti3NS:Rh0.03}$ . Additionally, the Rh-doping is also the key point of this system due to that the photocatalytic  $\text{H}_2$  evolution cannot be observed in the case of non-doped  $\text{Ti3NS}$ .

## Reference

1. Gong, J., Liang, J., & Sumathy, K. (2012). Review on dye-sensitized solar cells (DSSCs): Fundamental concepts and novel materials. *Renewable Sustainable Energy Rev.*, 16(8), 5848-5860.
2. Gong, J., Sumathy, K., Qiao, Q., & Zhou, Z. (2017). Review on dye-sensitized solar cells (DSSCs): Advanced techniques and research trends. *Renewable Sustainable Energy Rev.*, 68, 234-246.
3. Weickert, J., & Schmidt-Mende, L. (2014). Solid-State Dye-Sensitized Solar Cells. *Org. Photovoltaics*, 465-494.
4. Sahara, G., Abe, R., Higashi, M., Morikawa, T., Maeda, K., Ueda, Y., & Ishitani, O. (2015). Photoelectrochemical CO<sub>2</sub> reduction using a Ru(ii)–Re(i) multinuclear metal complex on a p-type semiconducting NiO electrode. *Chem. Commun.*, 51(53), 10722-10725.
5. Abe, R., Shinmei, K., Hara, K., & Ohtani, B. (2009). Robust dye-sensitized overall water splitting system with two-step photoexcitation of coumarin dyes and metal oxide semiconductors. *Chem. Commun.*,(24), 3577.
6. Kumagai, H., Sahara, G., Maeda, K., Higashi, M., Abe, R., & Ishitani, O. (2017). Hybrid photocathode consisting of a CuGaO<sub>2</sub> p-type semiconductor and a Ru(ii)–Re(i) supramolecular photocatalyst: non-biased visible-light-driven CO<sub>2</sub> reduction with water oxidation. *Chem. Sci.*, 8(6), 4242-4249.
7. Mathew, S., Yella, A., Gao, P., Humphry-Baker, R., Curchod, B. F., Ashari-Astani, N., Grätzel, M. (2014). Dye-sensitized solar cells with 13% efficiency

achieved through the molecular engineering of porphyrin sensitizers. *Nat. Chem.*, 6(3), 242-247.

8. Ferber, J., Stangl, R., Luther, J. (1998). An electrical model of the dye-sensitized solar cell. *Sol. Energy Mater. Sol. Cells.*, 53(1-2), 29-54.
9. Anandan, S. (2007). Recent improvements and arising challenges in dye-sensitized solar cells. *Sol. Energy Mater. Sol. Cells*, 91(9), 843-846.
10. Korfiatis, D. P., Potamianou, S. F., & Thoma, K. T. (2008). Modeling of dye-sensitized titanium dioxide solar cells. *Ionics*, 14, 545-548.
11. Bavarian, M., Nejati, S., Lau, K.K., Lee, D., Soroush, M.(2013). Theoretical and experimental study of a dye-sensitized solar cell. *Ind. Eng. Chem. Res.*, 53, 5234-5247.
12. Kalyanasundaram, K. (2010). *Dye-sensitized solar cells*. Lausanne: EPEL Press.
13. Youngblood, W. J., Lee, S. A., Maeda, K., & Mallouk, T. E. (2010). Visible Light Water Splitting Using Dye-Sensitized Oxide Semiconductors. *Acc. Chem. Res.*, 41(16).
14. Maeda, K., Sahara, G., Eguchi, M., & Ishitani, O. (2015). Hybrids of a Ruthenium(II) Polypyridyl Complex and a Metal Oxide Nanosheet for Dye-Sensitized Hydrogen Evolution with Visible Light: Effects of the Energy Structure on Photocatalytic Activity. *ACS Catal.*, 5(3), 1700-1707.
15. Ozawa, H., Kawaguchi, H., Okuyama, Y., & Arakawa, H. (2013). Ruthenium Sensitizers with 2,2'-Bipyrimidine or a 5,5'-Disubstituted 2,2'-Bipyrimidine Ligand: Synthesis, Photo- and Electrochemical Properties, and Application to Dye-Sensitized Solar Cells. *Eur. J. Inorg. Chem.*, 2013(29), 5187-5195.

16. Maeda, K., & Domen, K. (2007). New Non-Oxide Photocatalysts Designed for Overall Water Splitting under Visible Light. *J. Phys. Chem. C*, *111*(22), 7851-7861.
17. Higashino, T., & Imahori, H. (2015). Porphyrins as excellent dyes for dye-sensitized solar cells: recent developments and insights. *Dalton Trans.*, *44*(2), 448-463.
18. Abe, R. (2010). Recent progress on photocatalytic and photoelectrochemical water splitting under visible light irradiation. *J. Photochem. Photobiol., C*, *11*(4), 179-209.
19. Adeloye, A. O., & Ajibade, P. A. (2010). Synthesis and Characterization of a Heteroleptic Ru(II) Complex of Phenanthroline Containing Oligo-Anthracenyl Carboxylic Acid Moieties. *Int. J. Mol. Sci.*, *11*(9), 3158-3176.
20. Maeda, K., Eguchi, M., Youngblood, W. J., & Mallouk, T. E. (2008). Niobium Oxide Nanoscrolls as Building Blocks for Dye-Sensitized Hydrogen Production from Water under Visible Light Irradiation. *Chem. Mater.*, *20*(21), 6770-6778.
21. Maeda, K., Eguchi, M., Lee, S. A., Youngblood, W. J., Hata, H., & Mallouk, T. E. (2009). Photocatalytic Hydrogen Evolution from Hexaniobate Nanoscrolls and Calcium Niobate Nanosheets Sensitized by Ruthenium(II) Bipyridyl Complexes. *J. Phys. Chem. C*, *113*(18), 7962-7969.
22. Maeda, K., Eguchi, M., Youngblood, W. J., & Mallouk, T. E. (2009). Calcium Niobate Nanosheets Prepared by the Polymerized Complex Method as Catalytic Materials for Photochemical Hydrogen Evolution. *Chem. Mater.*, *21*(15), 3611-3617.

23. Birel, O., Nadeem, S., & Duman, H. (2017). Porphyrin-Based Dye-Sensitized Solar Cells (DSSCs): a Review. *J. Fluoresc.*, 27(3), 1075-1085.
24. Mochizuki, D., Sugiyama, M., Maitani, M. M., & Wada, Y. (2013). Rigidochromic Phosphorescence of [Ir(2-phenylpyridine)2(2,2'-bipyridine)] in C16TMA : Layered Silicate and Its Förster Resonance Energy Transfer. *Eur. J. Inorg. Chem.*, 2013(13), 2324-2329.
25. Yam, V. W. (2007). *Photofunctional Transition Metal Complexes*. New York: Springer-Verlag Berlin Heidelberg.
26. Chung, L., Lo, H., Ng, S., Ma, D., Leung, C., & Wong, C. (2015). Luminescent Iridium(III) Complexes Supported by N-Heterocyclic Carbene-based C<sup>^</sup>C<sup>^</sup>C-Pincer Ligands and Aromatic Diimines. *Sci. Rep.*, 5(1).
27. Metz, S., & Bernhard, S. (2010). Robust photocatalytic water reduction with cyclometalated Ir(III) 4-vinyl-2,2'-bipyridine complexes. *Chem. Commun.*, 46(40), 7551.
28. Zysman-Colman, E. (2017). *Iridium(III) in optoelectronic and photonics applications*. Hoboken, NJ: John Wiley & Sons Ltd.
29. Liu, Z. D., Zhao, H. X., & Huang, C. Z. (2012). Obstruction of Photoinduced Electron Transfer from Excited Porphyrin to Graphene Oxide: A Fluorescence Turn-On Sensing Platform for Iron (III) Ions. *PLoS ONE*, 7(12).
30. Panda, M. K., Ladomenou, K., & Coutsolelos, A. G. (2012). Porphyrins in bio-inspired transformations: Light-harvesting to solar cell. *Coord. Chem. Rev.*, 256(21-22), 2601-2627.
31. Murata, H., Kataoka, Y., Kawamoto, T., Tanaka, I., & Taniguchi, T. (2014).

- Photocatalytic activity of  $\alpha$ -PbO<sub>2</sub>-type TiO<sub>2</sub>. *Phys. Status Solidi RRL*, 8(10), 822-826.
32. Sato, K., Kataoka, Y., & Mori, W. (2012). Photochemical Production of Hydrogen from Water Using Microporous Porphyrin Coordination Lattices. *J. Nanosci. Nanotechnol.*, 12(1), 585-590.
  33. Sonotani, A., Shimada, T., & Takagi, S. (2017). "Size-matching Effect" in a Cationic Porphyrin–Titania Nanosheet Complex. *Chem.Lett.*, 46(4), 499-501.
  34. Morimoto, D., Sato, K., Saito, K., Yagi, M., Takagi, S., & Yui, T. (2017). Color tuning of cationic pyrene derivatives on a clay nanosheet: Retardation of gradual redshift on clay. *J. Photochem. Photobiol., A*, 337, 112-117.
  35. Takagi, S., Eguchi, M., Tryk, D., & Inoue, H. (2006). Porphyrin photochemistry in inorganic/organic hybrid materials: Clays, layered semiconductors, nanotubes, and mesoporous materials. *J. Photochem. Photobiol., C*, 7(2-3), 104-126.
  36. Fujimura, T., Shimada, T., Hamatani, S., Onodera, S., Sasai, R., Inoue, H., & Takagi, S. (2013). High Density Intercalation of Porphyrin into Transparent Clay Membrane without Aggregation. *Langmuir*, 29(16), 5060-5065.
  37. Yui, T., Tsuchino, T., Akatsuka, K., Yamauchi, A., Kobayashi, Y., Hattori, T., Haga, M., Takagi, K. (2006). Visible Light-Induced Electron Transfers in Titania Nanosheet and Mesoporous Silica Integrated Films. *Bull. Chem. Soc. Jpn.*, 79(3), 386-396.
  38. Dias, P. M., Faria, D. L., & Constantino, V. R. (2005). Clay-porphyrin systems: spectroscopic evidence of TMPyP Protonation, non-planar distortion and meso substituent rotation. *Clays Clay Miner.*, 53(4), 361-371.

39. Bhattacharjee, J., Banik, S., Hussain, S., & Bhattacharjee, D. (2015). A study on the interactions of cationic porphyrin with nano clay platelets in Layer-by-Layer (LbL) self assembled films. *Chem. Phys. Lett.*, 633, 82-88.
40. Constable, E. C., Neuburger, M., Rösel, P., Schneider, G. E., Zampese, J. A., Housecroft, C. E., Monti, F., Armaroli, N., Costa, R. D., Ortí, E. (2013). Ligand-Based Charge-Transfer Luminescence in Ionic Cyclometalated Iridium(III) Complexes Bearing a Pyrene-Functionalized Bipyridine Ligand: A Joint Theoretical and Experimental Study. *Inorg. Chem.*, 52(2), 885-897.

## Chapter 6

# The controlled synthesis of Rh doped titanate nanosheets and the crystalline effect on adsorption activity

### 6.1 Introduction

One of the promising nanoscale building blocks for various functional materials is Titanate nanosheets ( $[\text{Ti}_n\text{O}_{2n+1}]^{2-}$ ;  $\text{Ti}_n\text{NS}$ ) prepared by exfoliation of  $\text{A}_2\text{Ti}_n\text{O}_{2n+1}$  (A = alkali metal) in aqueous tetraalkylammonium hydroxide.<sup>1-4</sup> Accordingly, the investigation on both academic and practical viewpoint of  $\text{Ti}_n\text{NS}$  (particularly  $\text{Ti}_3\text{NS}$  and  $\text{Ti}_4\text{NS}$ ) is in progress (e.g., for energy- and environment-related applications).<sup>5-11</sup>

Recently, Rh-doped Ti<sub>3</sub>NS was synthesized by using solid state reaction and it was investigated for the photocatalytic decomposition of methylene blue (MB) in aqueous media,<sup>11</sup> revealing that the above nanosheets showed a very moderate activity. Therefore, the photocatalytic activity of Ti<sub>3</sub>NS was subsequently boosted by Rh doping at Ti sites to afford [Ti<sub>3-x</sub>Rh<sub>x</sub>O<sub>7</sub>]<sup>2-</sup> (Ti<sub>3</sub>NS:Rh<sub>x</sub>). Nevertheless, it was also insufficiently active which may probably due to the low adsorption ability of Ti<sub>3</sub>NS:Rh<sub>x</sub> for MB.

Unfortunately, the Rh doping amount in Ti<sub>3</sub>NS:Rh<sub>x</sub> cannot be control due to the solid state reaction was difficult to let the Ti and Rh atom completely melted and mixed. As a result, the doping amount was lower than adding amount. For example, only 10% of Rh atom was added comparing to Ti atom but only 1.5 % was doped. This indicated that the solid-state reaction is not a good synthesis method for Rh doped titanate compound. Hence, Rh and Ti should be completely mixed in atomic level in order to control the doping amount. Recently, the polymerized complex method has been reported for synthesis of metal oxide nanosheets.

Meanwhile, the crystal structure of Ti<sub>n</sub>NS with only minor differences observed in the basic crystal framework is almost independent of *n* as exemplified by the structures of common titanates such as Na<sub>2</sub>Ti<sub>3</sub>O<sub>7</sub>, and K<sub>2</sub>Ti<sub>4</sub>O<sub>9</sub> (Figure 6.1).<sup>5,7</sup> The three edge-shared TiO<sub>6</sub> octahedra is a basic unit of Ti<sub>3</sub>NS (Figure 6.1a), whereas that of Ti<sub>4</sub>NS contains four octahedra (Figure 6.1b), implying that the latter has a wider terrace than the former. Hence, crystal structure differences may probably affect the adsorption of various molecules and/or ions.

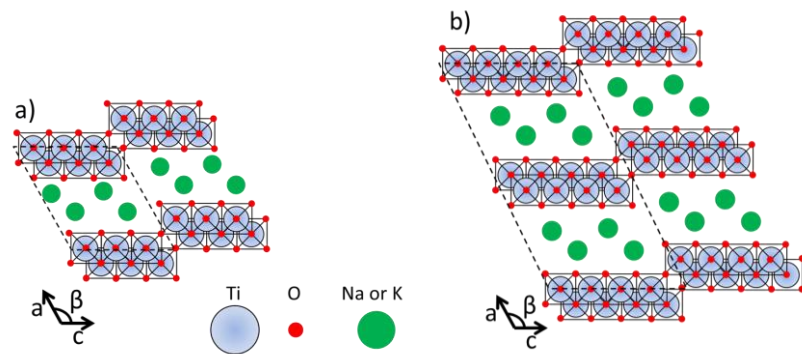


**Figure 6.1** Structures of a) a layered trititanate ( $\text{Na}_2\text{Ti}_3\text{O}_7$ ) and b) a layered tetratitanate ( $\text{K}_2\text{Ti}_4\text{O}_9$ ).

Due to the different particle shapes of these materials, the specific surface area of  $\text{H}_2\text{Ti}_4\text{O}_9$  powder was about 3–4 times larger than that of  $\text{H}_2\text{Ti}_3\text{O}_7$  powder as currently reported by Wang *et.al.* and Tamura *et.al.*.<sup>6,12</sup> Consequently, the molecular adsorption capacity of  $\text{H}_2\text{Ti}_4\text{O}_9$  was remarkably higher than that of  $\text{H}_2\text{Ti}_3\text{O}_7$ , and  $\text{Ti}_4\text{NS}$  was suggested to be a better catalyst for the photocatalytic decomposition of MB than  $\text{Ti}_3\text{NS}$ .

Colloidal aqueous suspensions of non-doped and Rh-doped  $\text{Ti}_4\text{NS}$  ( $[\text{Ti}_{4-x}\text{Rh}_x\text{O}_9]^{2-}$ ;  $\text{Ti}_4\text{NS}:\text{Rh}_x$ ) were prepared in this study. Moreover, their performance was studied for the adsorption and photocatalytic decomposition of MB in aqueous media. As a result, the MB adsorption capacities of these catalysts in the dark and their photocatalytic activity for MB decomposition under UV light irradiation were determined which highlights the effect of Rh doping on these parameters.

## 6.2 Experimental Procedures

### *Materials*

$\text{K}_2\text{CO}_3$  (Wako Pure Chemical Industries Co.),  $\text{Ti}[\text{OCH}(\text{CH}_3)_2]_4$  (Tokyo Chemical Industry Co.),  $\text{Rh}(\text{NO}_3)_3 \cdot 9\text{H}_2\text{O}$  (Wako Pure Chemical Industries Co.), tetramethylammonium hydroxide (TMAOH; Tokyo Chemical Industry Co.), and MB (Kanto Chemical Co.) were used without further purification.

### *Preparation of the Rh-doped potassium titanate*

$\text{K}_2\text{Ti}_{4-x}\text{Rh}_x\text{O}_9$  was synthesized using a polymerized complex (PC) method.<sup>13–16</sup>  $\text{Ti}[\text{OCH}(\text{CH}_3)_2]_4$ ,  $\text{K}_2\text{CO}_3$ , and  $\text{Rh}(\text{NO}_3)_3 \cdot 9\text{H}_2\text{O}$  were dissolved in water (50 mL) to

achieve a pre-set K:Ti:Rh molar ratio of  $2:(4-x):x$ , with  $x = 0, 0.04, 0.08, \text{ and } 0.2$ , and the obtained solution was treated with citric acid (11.5 g) and ethylene glycol (5 g). The reaction mixture was stirred at  $110\text{ }^{\circ}\text{C}$  to produce a transparent polymer gel that was carbonized at  $350\text{ }^{\circ}\text{C}$  for 4 h and subsequently calcined in air at 873 K, 973 K, or 1073 K for 24 h to remove residual carbon.

#### *Preparation of nanosheet colloidal suspensions*

Colloidal suspensions of Ti4NS:Rh $x$  were prepared by modifying the method described by Sasaki *et al.*<sup>17-19</sup>  $\text{K}_2\text{Ti}_{4-x}\text{Rh}_x\text{O}_9$  powder (1.0 g) was dispersed in 3 M aqueous HCl (200 mL) to exchange  $\text{K}^+$  for  $\text{H}^+$  and shaken for five days at room temperature, with the HCl solution replaced every day to increase protonation effectiveness. The precipitate of  $\text{H}_2\text{Ti}_{4-x}\text{Rh}_x\text{O}_9 \cdot n\text{H}_2\text{O}$  was filtered, washed with ultrapure water to remove residual HCl, and dried overnight under reduced pressure at room temperature, followed by dispersion in aqueous TMAOH ( $[\text{Ti}_{4-x}\text{Rh}_x\text{O}_9^{2-}]/[\text{TMAOH}] = 2$ ) by 5 days sonication. Non-exfoliated Ti4NS:Rh $x$  was removed by 15 min centrifugation at 4000 rpm (IEC61010-2-020, KUBOTA Co.), with the obtained supernatant corresponding to a colloidal aqueous suspension of Ti4NS:Rh $x$ .

#### *Adsorption properties of Ti4NS:Rh $x$* <sup>20-21</sup>

To study the adsorption of MB on Ti4NS:Rh $x$ , a 0.1-mg sample of either catalyst was added to 10 mL of aqueous MB ( $0\text{--}1 \times 10^{-4}$  M, pH 11), and the reaction mixture was stirred at room temperature for 24 h in the dark.

The MB/catalyst molar ratio was varied from 0 to 1. After stirring, the mixture was filtered through a hydrophilic polyfluoro resin membrane filter (pore size = 0.1  $\mu\text{m}$ ) to separate Ti4NS:Rh $x$ , and the amount of adsorbed MB was calculated from the absorbance of residual MB in the filtrate at 663 nm, assuming an extinction coefficient ( $\epsilon$ ) of  $5.2 \times 10^4 \text{ dm}^3/(\text{mol}\cdot\text{cm})$  at pH 11.

#### *Photodegradation of organic methylene blue dye<sup>22</sup>*

To characterize the photocatalytic activity of Ti4NS:Rh $x$  in aqueous media, suspensions of these materials in aqueous MB solutions were irradiated with UV light. Typically, the MB solution ( $4.7 \times 10^{-6} \text{ mol}$ ) was treated with Ti4NS:Rh $x$  ( $4.7 \times 10^{-6} \text{ mol}$ ) to afford a total volume of 10 mL (pH 11) and stirred in the dark to establish an adsorption equilibrium. Subsequently, UV light (254 nm, 0.88 mW/cm<sup>2</sup>) emitted by a Xe lamp (MAX-301, Asahi Spectra Co.) and passed through a band pass filter was used to irradiate the obtained mixture for a given time at room temperature, with the irradiation area confined to a 25-cm<sup>2</sup> square. After irradiation, the mixture was filtered through a hydrophilic polyfluoro resin membrane filter (pore size = 0.1  $\mu\text{m}$ ) to separate the catalysts, and the amount of decomposed MB was computed from the absorbance of residual MB in the filtrate at 663 nm.

#### *Characterization*

To analyze crystal structure of all materials, the powder X-ray diffraction (XRD) analysis was carried out by X-ray diffractometer (RIGAKU, MiniFlex II). Absorption spectra of various samples was measured by UV-Vis spectrophotometer (V-670 UV-VIS-NIR spectrophotometer, JASCO). Absorption spectra of liquid samples was measured by transmission mode. Diffuse reflectance (DR) spectra of solid sample was measured by UV-Vis spectrophotometer attached to an integrating sphere system (ISN-723, JASCO). Doped amount of Rh in Ti<sub>4</sub>NS:Rh<sub>x</sub> was estimated by ICP-AES apparatus (Optima2000DV, Perkinelmer). Scanning electron microscopy imaging was performed using JEOL-7001FA (JEOL Ltd.) operated at 12 kV.

### **6.3 Results and discussion**

#### *Synthesis of potassium titanate by PC method*

Figure 6.2 displays a photograph of potassium titanate precursor before and after calcination. Before calcination, the characteristic of precursor was black ash. After calcination, the black ash turned to white powder (Figure 6.2.b) which it was heated at 873 K, 973 K, or 1073 K for 24 hours. The XRD pattern of all synthesized samples is shown in figure 6.3. All the samples exhibited XRD pattern originated from K<sub>2</sub>Ti<sub>4</sub>O<sub>9</sub> indicating that K<sub>2</sub>Ti<sub>4</sub>O<sub>9</sub> can be synthesized by PC method. The diffraction peak at  $2\theta$  about  $10^\circ$  originated from stacked direction of K<sub>2</sub>Ti<sub>4</sub>O<sub>9</sub> crystal ( $d_{200}$ ). This  $d_{200}$  plane peak had higher intensity and got sharper when the temperature used in calcination increased. However, the powder obtained by calcination at 1173 K displays XRD

pattern with a diffraction peak of another structure of potassium titanate which was identified as a  $K_2Ti_2O_5$  and  $K_2Ti_8O_{17}$ . Figure 6.4 shows a SEM image of  $K_2Ti_4O_9$  synthesized at different temperature conditions. At 873 K and 973 K, crystal of  $K_2Ti_4O_9$  was not completely formed. While a rod-liked structure of  $K_2Ti_4O_9$  was completely formed at 1073 K. According to these results, PC method can be used to synthesize  $K_2Ti_4O_9$  and the best condition for calcination was at 1073 K.

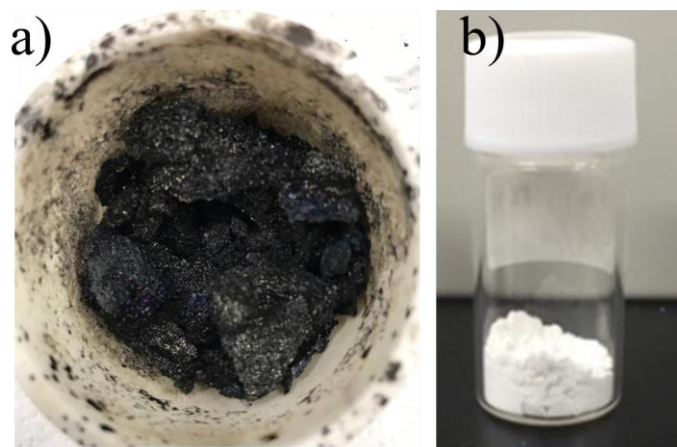


Figure 6.2 A photograph of potassium titanate precursor a) before and b) after calcination.

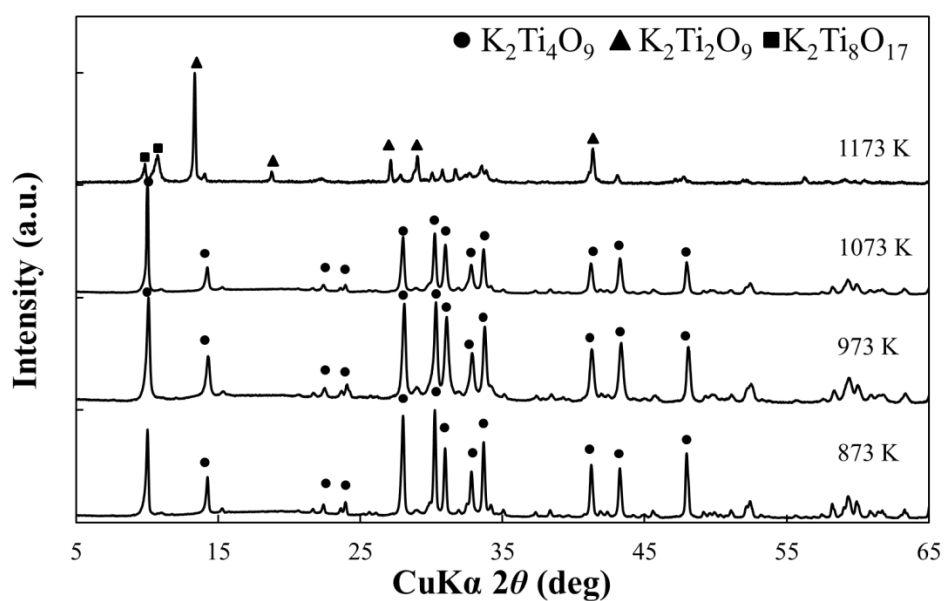


Figure 6.3 XRD pattern of potassium titanate obtained by calcination under various temperature from 873 K to 1173 K.

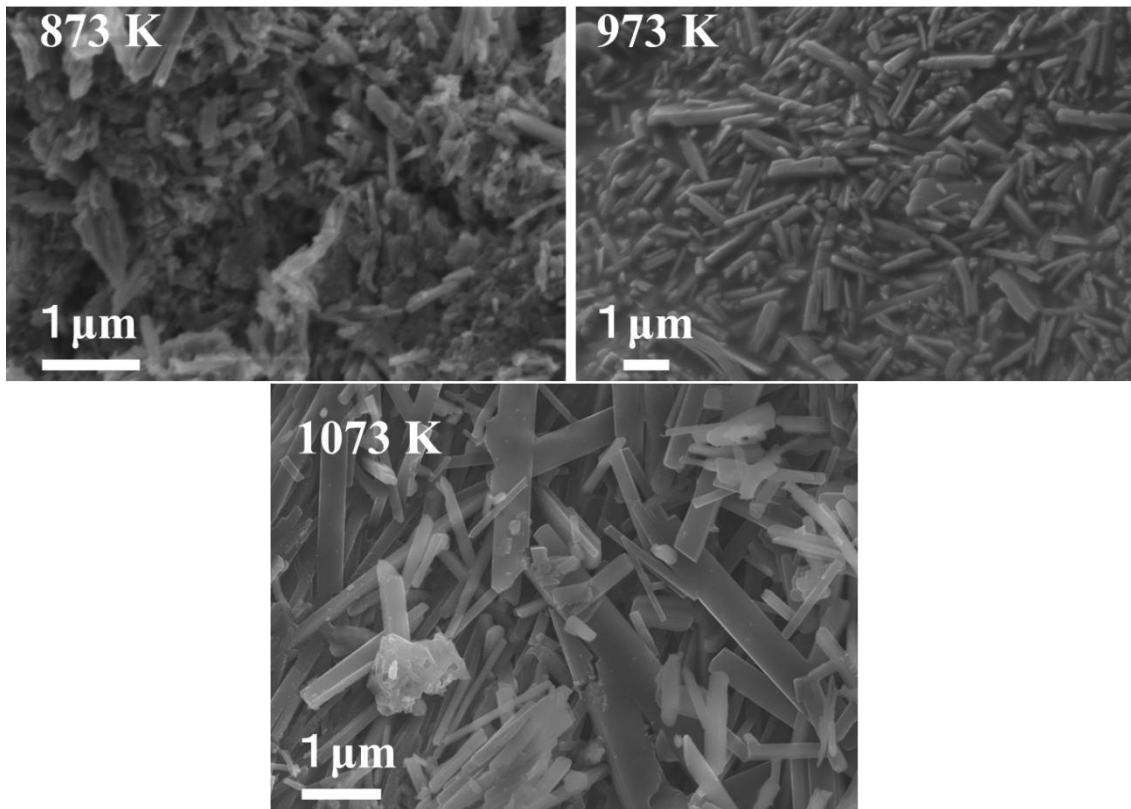


Figure 6.4 SEM image of  $K_2Ti_4O_9$  obtained by calcination under temperatures 873 K, 973, and 1073 K.

The Rh-doped  $\text{K}_2\text{Ti}_4\text{O}_9$  was synthesized by PC method and calcinated at 1073K as same as non-doped  $\text{K}_2\text{Ti}_4\text{O}_9$ . The Rh-added amount was set as 0, 1% ( $x = 0.04$ ), 2% ( $x = 0.08$ ), and 5% ( $x = 0.2$ ) of Ti atoms. When Rh was being added, the power color was changed from white to orange as shown in figure 6.5. Moreover, the orange color got deeper as the Rh added amount increased. Figure 6.6 displays the XRD pattern of Rh-added  $\text{K}_2\text{Ti}_4\text{O}_9$ . Only Rh1% added  $\text{K}_2\text{Ti}_4\text{O}_9$  samples exhibited same XRD pattern as  $\text{K}_2\text{Ti}_4\text{O}_9$  with no impurity observed. While Rh 2% ( $x = 0.08$ ) and 5% ( $x = 0.2$ ) added  $\text{K}_2\text{Ti}_4\text{O}_9$  shows different crystal structure. Although, this XRD pattern cannot be identified. This indicates that the large amount of Rh doping resulted in the distortion of  $\text{K}_2\text{Ti}_4\text{O}_9$  crystal lattice.

The SEM image of Rh 0% ( $x = 0$ ) and Rh 1% ( $x = 0.04$ ) added  $\text{K}_2\text{Ti}_4\text{O}_9$  are shown in figure 6.7. The particle size of Rh 1% ( $x = 0.04$ ) added  $\text{K}_2\text{Ti}_4\text{O}_9$  is almost equal to Rh 0% ( $x = 0$ ) added  $\text{K}_2\text{Ti}_4\text{O}_9$ . Thus, low adding amount of Rh does not change the crystal structure of  $\text{K}_2\text{Ti}_4\text{O}_9$ .

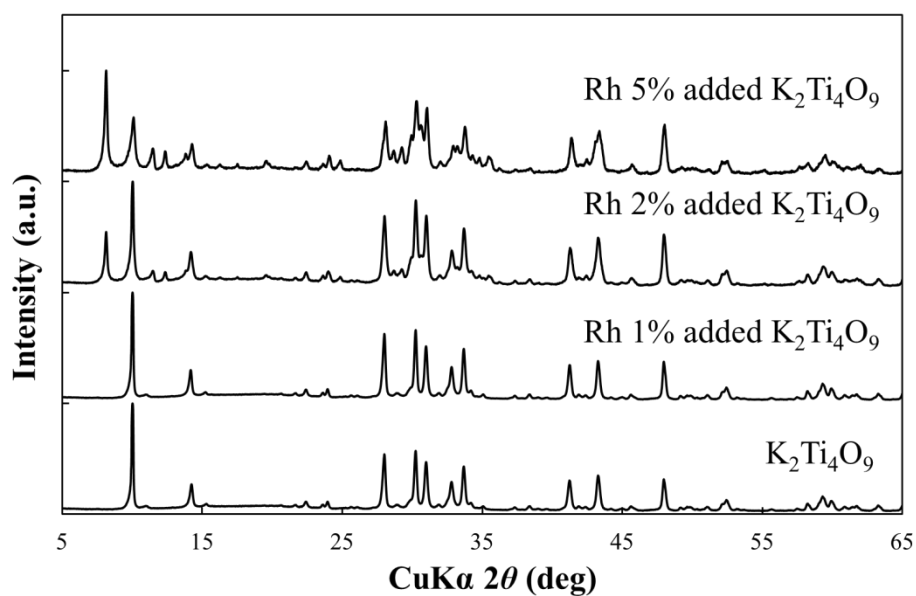


Figure 6.6 XRD patterns of synthesized Rh-doped K<sub>2</sub>Ti<sub>4</sub>O<sub>9</sub> with varied Rh added amount.

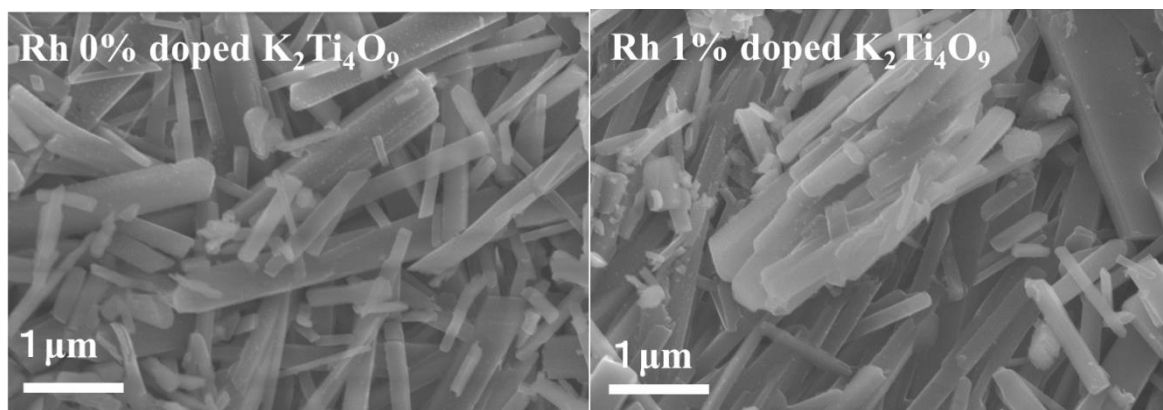


Figure 6.7 SEM image of non-doped and 1% Rh-doped K<sub>2</sub>Ti<sub>4</sub>O<sub>9</sub>

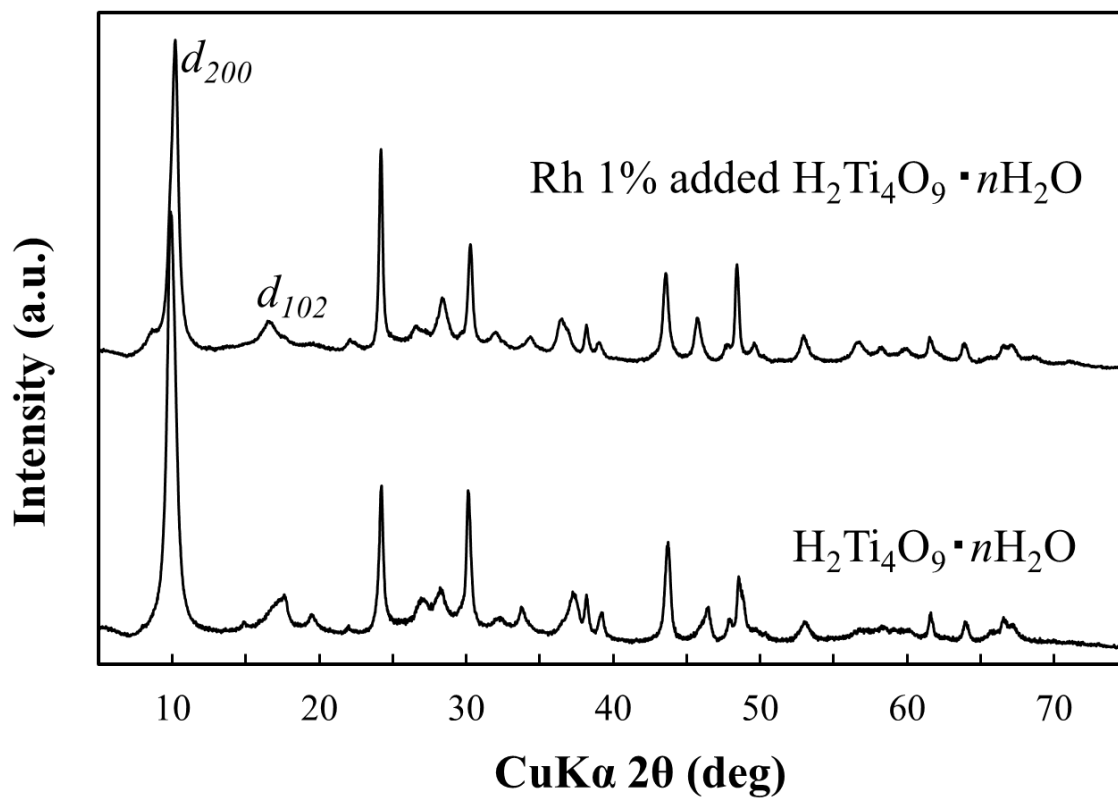


Figure 6.8 XRD patterns of non-doped and 1% Rh-doped H<sub>2</sub>Ti<sub>4</sub>O<sub>9</sub> · nH<sub>2</sub>O.

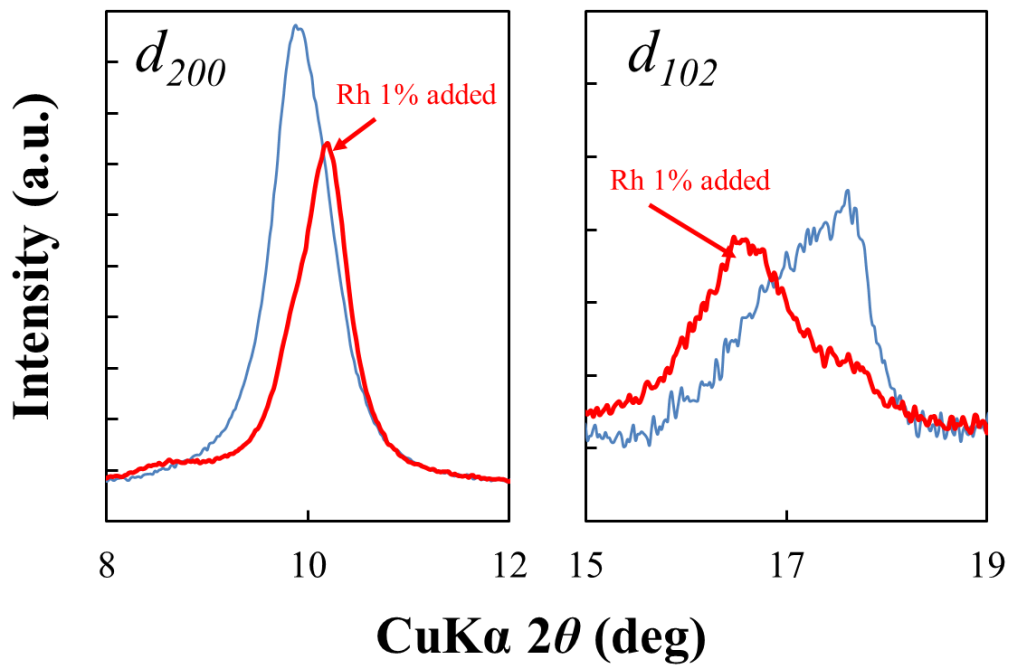


Figure 6.9 XRD patterns show the diffraction peaks originated from  $d_{200}$  and  $d_{102}$  of non-doped and 1% Rh-doped  $\text{H}_2\text{Ti}_4\text{O}_9 \cdot n\text{H}_2\text{O}$ .

Figure 6.8 shows the XRD pattern of  $K_2Ti_4O_9$  after the proton exchange. The XRD pattern agreed with literature data of  $H_2Ti_4O_9 \cdot nH_2O$ . Moreover, Rh 1% ( $x = 0.04$ ) added  $H_2Ti_4O_9 \cdot nH_2O$  was also analogous to the pattern of  $H_2Ti_4O_9 \cdot nH_2O$  with no impurity peaks observed. As shown in Figure 6.9, the  $d_{200}$  diffraction peak of  $H_2Ti_4O_9 \cdot nH_2O$  observed at  $\sim 10^\circ$  shifted to higher angles after doping with Rh. This designated that the crystal structure shrank in the stacking direction. However, this alteration could not be explained by the different amount of water molecule  $n$ , which was almost identical in both cases (1.45 and 1.50 for  $H_2Ti_4O_9 \cdot nH_2O$  and  $H_2Ti_{3.96}Rh_{0.04}O_9 \cdot nH_2O$ , respectively). Therefore, this shift was ascribed to Rh doping, with the same reasoning used to explain the shift of the  $d_{102}$  diffraction peak to lower angles. This could be caused by the ionic radius of  $Rh^{3+}$  is larger than  $Ti^{4+}$ . This made the  $RhO_6$  unit become bigger than  $TiO_6$  enlarging the in-plane direction of  $Ti_4O_9$  units which exhibited in the lower angles shift of the  $d_{102}$  diffraction peak. Simultaneously, the shrinkage of the  $d_{200}$  diffraction peak could be caused by the difference of ionic charge between  $Rh^{3+}$  and  $Ti^{4+}$ . When the  $Rh^{3+}$  species occupying Ti sites, it will make the surface charge density of  $Ti_4O_9$  units become more negative henceforth increases the electrostatic force between  $Ti_4O_9$  units and counter cations which a proton in this case.

The Rh doped amount measured from ICP-AES of  $Ti_4NS$  colloidal suspension shown in table 6.1. The Rh doped amount is nearly equivalent to the added amount. From these results, PC method can be used in synthesizing titanate compound including metal doping which the amount can be controlled unlike the solid-state reaction.

Table 6.1. The chemical formula of synthesized nanosheets.

Sample	Rh added amount	Rh doped amount (x)	Chemical formula
Ti4NS:Rh0	0	0	$\text{Ti}_{4.00}\text{O}_9^{2-}$
Ti4NS:Rh0.04	0.04	$0.039 \pm 0.002$	$\text{Ti}_{3.96}\text{Rh}_{0.04}\text{O}_9^{(2+\delta)-}$

Figure 6.10 shows the adsorption spectra of  $\text{H}_2\text{Ti}_{4-x}\text{Rh}_x\text{O}_9$  in term of Kubelka Munk function and the adsorption spectra of  $\text{Ti}_4\text{NS}:\text{Rh}_x$  measured by transmission mode. The adsorption spectra of  $\text{H}_2\text{Ti}_{4-x}\text{Rh}_x\text{O}_9$  shows an adsorption band about  $<350$  nm which originated from  $\text{H}_2\text{Ti}_4\text{O}_9$ . Furthermore, new adsorption band was observed and new adsorption band increases depending on Rh amount. Thus, this new adsorption is dependent on the amount of Rh being doped. This is different from Rh-doped titanate ( $\text{H}_2\text{Ti}_{3-x}\text{Rh}_x\text{O}_7$ ) compound as mentioned in chapter 3 and 4 as  $\text{H}_2\text{Ti}_{4-x}\text{Rh}_x\text{O}_9$  does not show adsorption band at long wavelength ( $400 < \lambda < 600$ ). This assumes that most of Rh being doped in the state of  $\text{Rh}^{3+}$ .

The calculated energy band gaps are shown in table 6.2. The energy band gaps show the change in values with not much difference from the non-doped case. The adsorption spectra of  $\text{Ti}_4\text{NS}:\text{Rh}_x$  shows that the adsorption band shifted towards blue meaning crystal of titanate compound changed from bulk to nanoscale sheet due to quantum size effect.<sup>23</sup> From these results, the  $\text{K}_2\text{Ti}_4\text{O}_9$  compound and  $\text{K}_2\text{Ti}_{4-x}\text{Rh}_x\text{O}_9$  can be synthesized from PC method and controlled the Rh-doped amount. Furthermore, the present procedure can prepare  $\text{Ti}_4\text{NS}:\text{Rh}_x$  colloidal suspension.

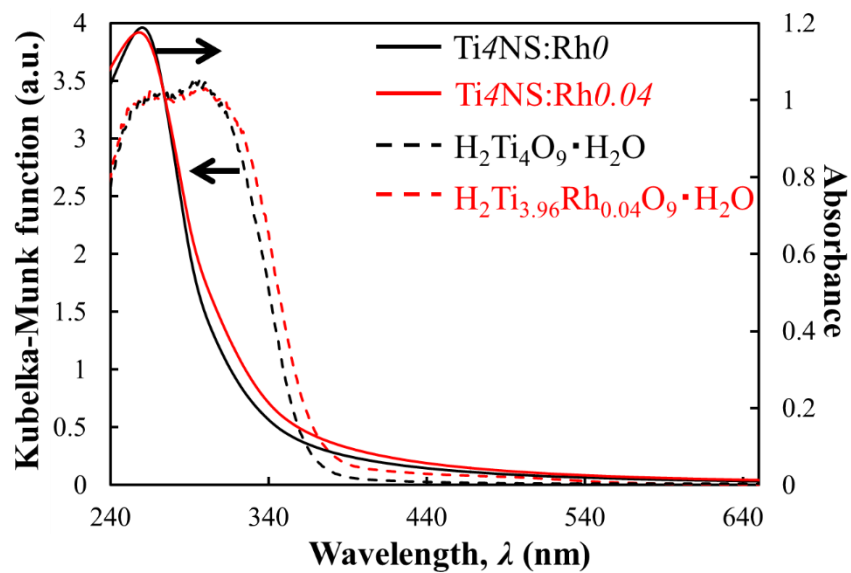


Figure 6.10 The UV-Vis absorption spectra of the Ti4NS:Rh<sub>x</sub> colloidal suspension (concentration of 1 mg/dm<sup>3</sup>) and diffuse reflectance spectra of the H<sub>2</sub>Ti<sub>4-x</sub>Rh<sub>x</sub>O<sub>9</sub> · nH<sub>2</sub>O powders.

Table 6.2. Energy band gap of synthesized nanosheets.

Sample	Energy band gap, $E_g$
Ti4NS:Rh0	$3.45 \pm 0.04$
Ti4NS:Rh0 .04	$3.40 \pm 0.04$

### *The adsorption ability of Ti4NS:Rh<sub>x</sub>*

The organic dye adsorption was observed using Ti4NS:Rh0 and Ti4NS:Rh0.04 degrading methylene blue. Figure 6.11 shows adsorption isothermal curve of Ti4NS:Rh<sub>x</sub> and Ti3NS:Rh0. The adsorption isothermal curve is plotted between  $C^{add}$  and  $C^{ads}$  which denoting the amounts of MB added and adsorbed per Ti4NS:Rh<sub>x</sub> or Ti3NS:Rh<sub>x</sub> unit, respectively. Saturated adsorption capacities ( $C^{max}$ ) estimated from adsorption isotherms are presented in Table 6.3. As a result, Ti4NS:Rh0 has an adsorption at equilibrium at  $C^{max}$  equal to ~0.054 (mol/mol). While, Ti4NS:Rh0.04 has adsorption at equilibrium at  $C^{max}$  equal to ~0.061 (mol/mol). The adsorption of MB by Ti4NS:Rh<sub>x</sub> occurred from electrostatic force between cationic MB and anionic Ti4NS:Rh<sub>x</sub> because of the adsorption ability result of Ti3NS:Rh<sub>x</sub> in chapter 3. Ti4NS:Rh0.04 at equilibrium has higher absorption value than Ti4NS:Rh0 a little. This may due to Rh<sup>3+</sup> was doped to replace Ti<sup>4+</sup> resulting in surface charge becomes more anionic. Additionally, the electrostatic interaction between MB and Ti4NS:Rh<sub>x</sub> increases causing higher adsorption value.

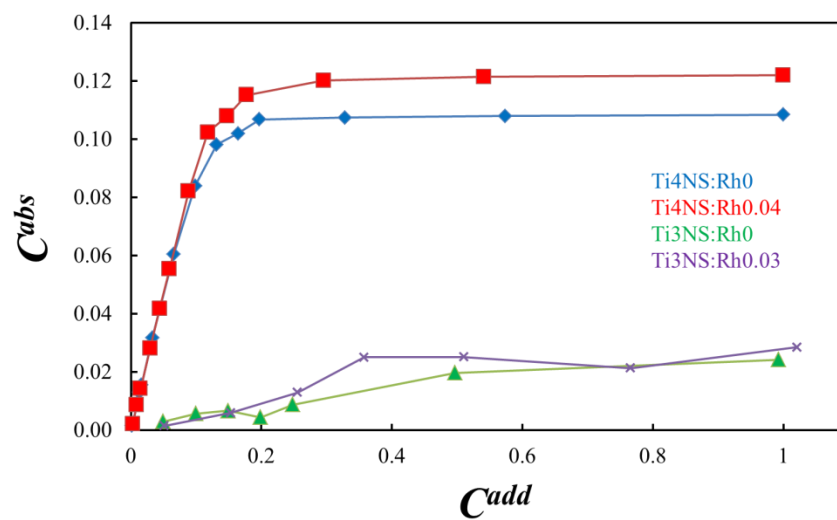


Figure 6.11 The adsorption curves of MB by various titanate nanosheets.(▲ Ti3NS:Rh0, x Ti3NS:Rh0.03, ◆ Ti4NS:Rh0, and ■ Ti4NS:Rh0.04)

Table 6.3. The maximum adsorption amount ( $C^{max}$ ) of MB adsorbed by Ti3NS:Rh<sub>x</sub> and Ti4NS:Rh<sub>x</sub> at equilibrium state.

Sample	$C^{max}$ (% mol/mol)
Ti3NS:Rh0	$1.5 \pm 0.1$
Ti3NS:Rh0.03	$1.4 \pm 0.2$
Ti4NS:Rh0	$5.4 \pm 0.7$
Ti4NS:Rh0.04	$6.1 \pm 0.8$

Comparing to Ti3NS:Rh0 which explained in the chapter 3, Ti4NS:Rh<sub>x</sub> has maximum adsorption at equilibrium higher than Ti3NS:Rh0 about 4 folds. According to the classification of adsorption isotherms proposed by Giles *et al.*,<sup>24</sup> that of Ti4NS:Rh<sub>x</sub> was of the high affinity-type, and that of Ti3NS was of the low affinity-type. This result cannot be explained with anionic charge of Ti3NS:Rh0 and Ti4NS:Rh<sub>x</sub> because both anionic charges do not differ much. This incident can be explained by the interaction between exfoliation reagent TMAOH and the different particle size of Ti3NS and Ti4NS. Figure 6.12 shows the SEM image of Ti3NS and Ti4NS powder which collected by the reaction between Ti3NS or Ti4NS colloidal suspension and hydrochloric acid; then filtered and washed, and dried in vacuum. The SEM image exhibits clearly that particle size of Ti3NS and Ti4NS are entirely different as Ti4NS is smaller than Ti3NS hence the adsorption surface area of Ti4NS is larger than Ti3NS. As a result, the adsorption amount is higher.

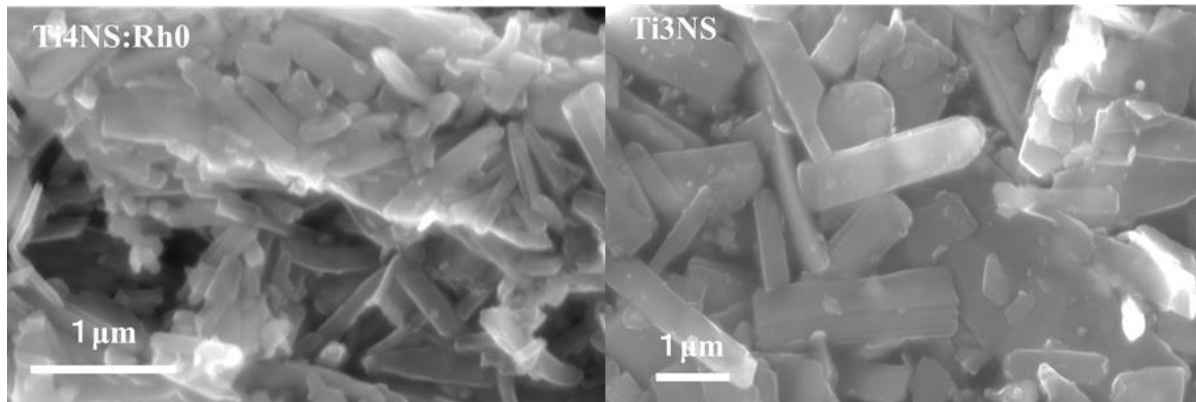


Figure 6.12 SEM image of Ti4NS and Ti3NS after acid treatment by mixed the Ti3NS or Ti4NS with  $1 \text{ mol/dm}^3$  hydrochloric acid for 1 hour. The powders were collected by filtration and drying in vacuum overnight. From this images, it was found that the particle size of Ti3NS is bigger than Ti4NS where both of them have same thickness, theoretically. The average particle size of Ti3NS calculated from this image is about  $1 \mu\text{m}^2$  while that of Ti4NS is about  $0.15 \mu\text{m}^2$ .

*The photocatalytic activity of Ti4NS:Rh<sub>x</sub> on the photodegradation of MB*

Figure 6.13.a) and b) displays the UV-Vis absorption spectra of MB-containing filtrates obtained by filtering suspensions of Ti4NS:Rh<sub>x</sub> in aqueous MB. They were subjected to UV light irradiation for a given time, revealing that the absorbance of the MB filtrate gradually decreased with the increasing of irradiation time. In addition, no byproduct absorption bands could be detected implying that Ti4NS:Rh<sub>x</sub> achieved complete MB decomposition under UV light irradiation.

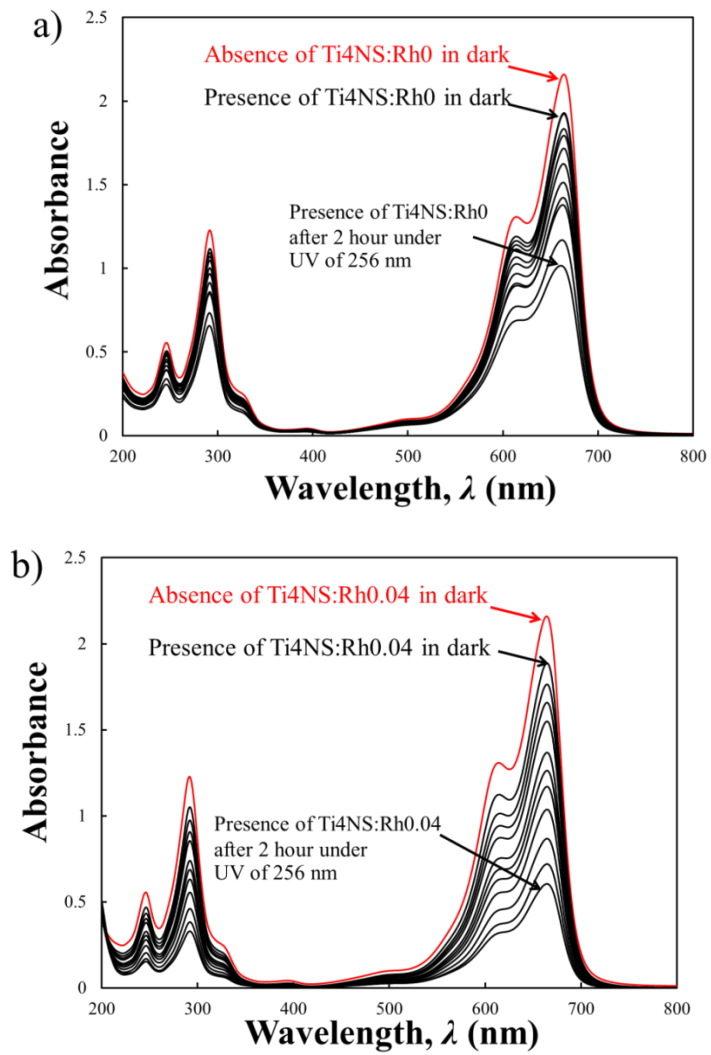


Figure 6.13 UV-vis absorption spectral changes of MB solution under UV light (at a wavelength of 254 nm) irradiation in the presence of a) Ti4NS:Rh0 and b) Ti4NS:Rh0.04.

Figure 6.14 shows a plot of MB decomposition efficiency ( $R$ ) vs. irradiation time, with  $R$  defined as

$$R = \frac{A^{663}(0) - A^{663}(t)}{A^{663}(0)} \times 100\%, \quad (1)$$

where  $A^{663}(0)$  and  $A^{663}(t)$  are absorbances at 663 nm before and after irradiation for a given time  $t$ , respectively. All studied samples, including Ti3NS used as a reference, enhanced the photocatalytic decomposition of MB under UV light irradiation. Additionally, the photocatalytic decomposition activity of Ti4NS:Rh<sub>x</sub> exceeding that of Ti3NS:Rh<sub>x</sub> in agreement with the results of adsorption experiments. Consequently, this behavior was ascribed to the variance of MB adsorption capacity. Furthermore, the activity of Ti4NS:Rh<sub>x</sub> was increased by Rh doping at Ti sites.

The initial quantum yields of photocatalytic MB decomposition ( $\phi_D$ ) were calculated using equation (2) (Table 6.4):

$$\phi_D = \frac{n_D}{n_{\text{photon}}} \times 100. \quad (2)$$

In the above equation,  $n_D$  and  $n_{\text{photon}}$  denote the number of MB molecules photocatalytically decomposed under UV light irradiation and the number of incident photons, respectively. As a result, Ti4NS:Rh<sub>0.04</sub> was shown to exhibit  $\phi_D$  approximately four times higher than Ti4NS:Rh<sub>0</sub>, which was attributed to Rh doping at Ti sites, since both catalysts showed comparable  $C^{\text{max}}$  and bandgap energy values. Thus, Rh doping at Ti sites was proven to significantly enhance the photocatalytic decomposition activity of Ti4NS:Rh<sub>x</sub>.

As it was discussed in chapter 3, the presence of Rh<sup>3+</sup> and Rh<sup>4+</sup> and the redox cycle of Rh atoms doped at Ti sites which triggered by UV-light irradiation can improve the

photocatalytic activity of Ti4NS. Unlike Ti3NS:Rh<sub>x</sub>, Ti4NS:Rh<sub>x</sub> showed only the absorption band of Rh<sup>3+</sup>. However, the photocatalytic activity of Ti4NS:Rh0.04 was higher than Ti4NS:Rh0. This suggested that not only the presence of Rh<sup>3+</sup> and Rh<sup>4+</sup> was important but the redox cycle of Rh improved the photocatalytic activity of Ti4NS.

The Rh<sup>3+/4+</sup> redox cycle of Rh atoms doped at Ti sites is triggered by UV-light irradiation, as stated previously. Moreover, the RhO<sub>6</sub> octahedral unit is known to pool photogenerated holes.<sup>25-27</sup> Since Ti4NS features TiO<sub>6</sub> octahedra as a structural motif, Rh atoms doped at Ti sites are expected to be octahedrally coordinated by oxygen and thus function as hole pools. Hence, we conclude that the improved photocatalytic activity of Ti4NS:Rh<sub>x</sub> was caused by the synergistic effect of the Rh<sup>3+/4+</sup> redox cycle and the hole pooling effect.

#### **6.4 Conclusion**

The PC method can be used to synthesize a Rh-doped titanate compound with controlled doped amount. It has been demonstrated that Ti4NS:Rh<sub>x</sub> is a promising photocatalyst for decomposing cationic organic dyes in aqueous media. Likewise, its activity can be enhanced by Rh doping at Ti sites. The excellent MB degradation performance of Ti4NS:Rh<sub>x</sub> was explained by the high adsorption capacity of this catalyst for MB as well as by the synergistic effect of the Rh<sup>3+/4+</sup> redox cycle. Importantly, the present study reveals the effectiveness of doping with metals exhibiting multiple oxidation states, as demonstrated by the improved photocatalytic decomposition activity of Ti4NS.



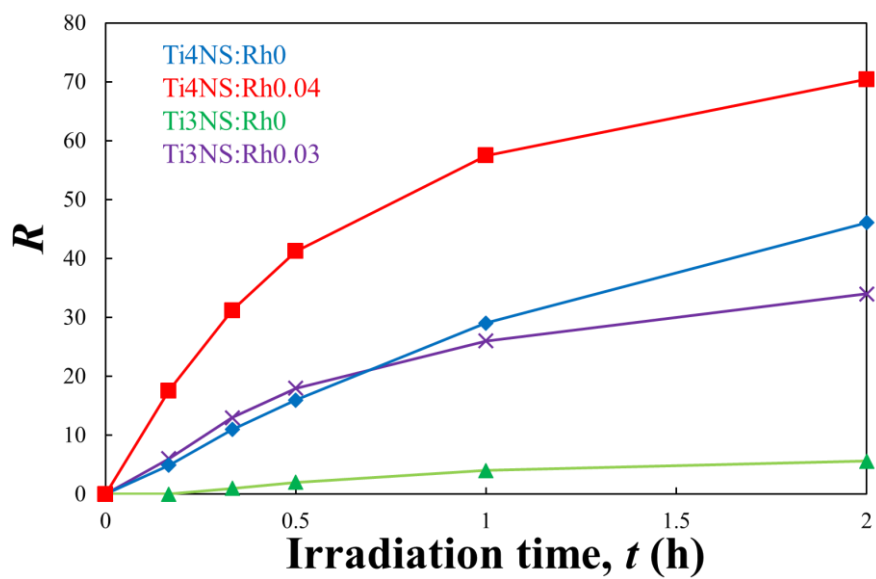


Figure 6.14 The photocatalytic decomposition rate of MB  $R$ , in the presence of the different samples after the UV light ( $\lambda = 254$  nm) irradiation over different irradiation times. The degradation amount was calculated from remained MB amount in filtrated solution. The extinction coefficient ( $\epsilon$ ) of the MB solution was  $5.2 \times 10^4$  dm<sup>3</sup>/mol·cm.

Table 6.4. Quantum yield ( $\phi_D$ ) of MB photodegradation.

Sample	$\phi_D$ (%)
Ti4NS:Rh0	0.27
Ti4NS:Rh0.04	0.96

## References

1. Kishore, B., G, V., & Munichandraiah, N. (2016). K<sub>2</sub>Ti<sub>4</sub>O<sub>9</sub>: A Promising Anode Material for Potassium Ion Batteries. *J. Electrochem. Soc.*, 163(13).
2. Bao, N., Feng, X., Shen, L., & Lu, X. (2002). Calcination Syntheses of a Series of Potassium Titanates and Their Morphologic Evolution. *Cryst. Growth Des.*, 2(5), 437-442.
3. Tournoux, M., Marchand, R., & Brohan, L. (1986). Layered K<sub>2</sub>Ti<sub>4</sub>O<sub>9</sub> and the open metastable TiO<sub>2</sub>(B) structure. *Prog. Solid State Chem.*, 17(1), 33-52.
4. Cao, Y., Zhu, K., Wu, Q., Gu, Q., & Qiu, J. (2014). Hydrothermally synthesized barium titanate nanostructures from K<sub>2</sub>Ti<sub>4</sub>O<sub>9</sub> precursors: Morphology evolution and its growth mechanism. *Mater. Res. Bull.*, 57, 162-169.
5. Kikkawa, S., Yasuda, F., & Koizumi, M. (1985). Ionic conductivities of Na<sub>2</sub>Ti<sub>3</sub>O<sub>7</sub>, K<sub>2</sub>Ti<sub>4</sub>O<sub>9</sub> and their related materials. *Mater. Res. Bull.*, 20(10), 1221-1227.
6. Wang, J., Yin, S., & Sato, T. (2006). Characterization of H<sub>2</sub>Ti<sub>4</sub>O<sub>9</sub> with high specific surface area prepared by a delamination/reassembling process. *Mater. Sci. Eng., B*, 126(1), 53-58.
7. Izawa, H., Kikkawa, S., & Koizumi, M. (1982). Ion exchange and dehydration of layered [sodium and potassium] titanates, Na<sub>2</sub>Ti<sub>3</sub>O<sub>7</sub> and K<sub>2</sub>Ti<sub>4</sub>O<sub>9</sub>. *J. Phys. Chem.*, 86(25), 5023-5026.
8. Miyamoto, N., Kuroda, K., & Ogawa, M. (2004). Exfoliation and film preparation of a layered titanate, Na<sub>2</sub>Ti<sub>3</sub>O<sub>7</sub>, and intercalation of pseudoisocyanine dye. *J. Mater. Chem.*, 14(2), 165.
9. Sasaki, T., Watanabe, M., Hashizume, H., Yamada, H., & Nakazawa, H. (1996). Macromolecule-like Aspects for a Colloidal Suspension of an Exfoliated Titanate. Pairwise Association of Nanosheets and Dynamic Reassembling Process Initiated from It. *J. Am. Chem. Soc.*, 118(35), 8329-8335.
10. Ogawa, M., & Takizawa, Y. (1999). Intercalation of Alkylammonium Cations into a Layered Titanate in the Presence of Macrocyclic Compounds. *Chem. Mater.*, 11(1), 30-32.
11. Airoidi, C., Nunes, L. M., & Farias, R. F. (2000). The intercalation of n-alkyldiamines into crystalline layered titanate. *Mater. Res. Bull.*, 35(13), 2081-2090.
12. Tamura, H., Nakamura, K., Kikkawa, S. (2007). Cation exchange properties of tetratitanic acid with interlayer protons and of titania with surface hydroxyl protons. *Croatica. Chemica. Acta.*, 80(3-4), 351-356.
13. Yanagisawa, M., Uchida, S., Yin, S., & Sato, T. (2001). Synthesis of Titania-Pillared Hydrogen Tetratitanate Nanocomposites and Control of Slit Width. *Chem. Mater.*, 13(1), 174-178.
14. Bao, N., Feng, X., Shen, L., & Lu, X. (2002). Calcination Syntheses of a Series of Potassium Titanates and Their Morphologic Evolution. *Cryst. Growth Des.*, 2(5), 437-442.
15. Ikeda, S., Hara, M., Kondo, J. N., Domen, K., Takahashi, H., Okubo, T., &

- Kakihana, M. (1998). Preparation of  $K_2La_2Ti_3O_{10}$  by Polymerized Complex Method and Photocatalytic Decomposition of Water. *Chem. Mater.*, *10*(1), 72-77.
16. Maeda, K., Eguchi, M., Youngblood, W. J., & Mallouk, T. E. (2009). Calcium Niobate Nanosheets Prepared by the Polymerized Complex Method as Catalytic Materials for Photochemical Hydrogen Evolution. *Chem. Mater.*, *21*(15), 3611-3617.
  17. Sasaki, T., Ebina, Y., Watanabe, M., Decher, G. (2000). Multilayer ultrathin films of molecular titania nanosheets showing highly efficient UV-light absorption. *Chem. Commun.*, (21), 2163-2164.
  18. Sasaki, T., Ebina, Y., Kitami, Y., Watanabe, M., Oikawa, T. (2001). Two-Dimensional Diffraction of Molecular Nanosheet Crystallites of Titanium Oxide. *J. Phys. Chem. B*, *105*(26), 6116-6121.
  19. Sasaki, T., Ebina, Y., Fukuda, K., Tanaka, T., Harada, M., & Watanabe, M. (2002). Titania Nanostructured Films Derived from a Titania Nanosheet/Polycation Multilayer Assembly via Heat Treatment and UV Irradiation. *Chem. Mater.*, *14*(8), 3524-3530.
  20. Kuo, W., & Ho, P. (2006). Solar photocatalytic decolorization of dyes in solution with  $TiO_2$  film. *Dyes Pigm.*, *71*(3), 212-217.
  21. Dariani, R., Esmaeili, A., Mortezaali, A., & Dehghanpour, S. (2016). Photocatalytic reaction and degradation of methylene blue on  $TiO_2$  nano-sized particles. *Optik*, *127*(18), 7143-7154.
  22. Xu, C., Rangaiah, G. P., & Zhao, X. S. (2014). Photocatalytic Degradation of Methylene Blue by Titanium Dioxide: Experimental and Modeling Study. *Ind. Eng. Chem. Res.*, *53*(38), 14641-14649.
  23. Osada, M., & Sasaki, T. (2012). 2D Inorganic Nanosheets: Two-Dimensional Dielectric Nanosheets: Novel Nanoelectronics From Nanocrystal Building Blocks. *Adv. Mater.*, *24*(2), 209-209.
  24. Giles, C. H., Mehta, H. V., Rahman, S. M., & Stewart, C. E. (1959). Adsorption at inorganic surfaces. V. Adsorption of sulphonated dyes the anodic film on aluminium. *J. Biochem. Toxicol.*, *9*(9), 457-466.
  25. Kawasaki, S., Akagi, K., Nakatsuji, K., Yamamoto, S., Matsuda, I., Harada, Y., Yoshinobu, H., Komori, F., Takahashi, R., Lippmaa, M., Sakai, C., Niwa, H., Oshima, M., Iwashina, K., and Kudo, A. (2012). Elucidation of Rh-Induced In-Gap States of Rh:  $SrTiO_3$  Visible-Light-Driven Photocatalyst by Soft X-ray Spectroscopy and First-Principles Calculations. *J. Phys. Chem. C*, *116*(46), 24445-24448.
  26. Yoshida, H., Shimura, K. (2012). XAFS Study of Rhodium Cocatalyst Loaded on  $K_2Ti_6O_{13}$  Photocatalyst. *Photon Factory Activity Report 2011*, *29*, 40.
  27. Shimura, K., Kawai, H., Yoshida, T., & Yoshida, H. (2012). Bifunctional Rhodium Cocatalysts for Photocatalytic Steam Reforming of Methane over Alkaline Titanate. *ACS Catal.*, *2*(10), 2126-2134.

# Chapter 7

## Conclusion

### 7.1 Summary

In chapter 2, we were successful at synthesizing Rh-doped titanate nanosheets (Ti<sub>3</sub>NS:Rh<sub>x</sub>) with varied doped amount. The result of energy band structure showed that Rh-doping caused valence band level of Ti<sub>3</sub>NS narrower without directly affecting the conduction band. Moreover, we found that Rh can be doped in two states which are Rh<sup>3+</sup> and Rh<sup>4+</sup>. The adsorption of methylene blue (MB) dye by Ti<sub>3</sub>NS was affected by Rh being doped into the structure of Ti<sub>3</sub>NS. Nevertheless, Ti<sub>3</sub>NS:Rh<sub>x</sub> can slightly adsorb MB dye. Meanwhile, Ti<sub>3</sub>NS:Rh<sub>x</sub> cannot adsorb methylene orange (MO) dye due to both

are in the anionic state. Therefore, MO was pushed away by the surface charge at the surface of Ti3NS. The adsorption activity of Ti3NS:Rh<sub>x</sub> depends on the electrostatic interaction between sheet and target molecules. When photocatalytic activity of Ti3NS:Rh<sub>x</sub> was measured in the photocatalytic degradation reaction of MB and MO dye, we found that only MB was degraded by Ti3NS:Rh<sub>x</sub> under UV irradiation. This indicated that Ti3NS:Rh<sub>x</sub> can degrade MB dye by photogenerated hole in the valence band to oxidize MB dye. In addition, when Rh was doped into the structure of Ti3NS resulted in degradation efficiency increased. From this result, we can explain the existence of Rh<sup>4+</sup> functions as hole pool. When the doped amount increased the more Rh<sup>4+</sup> would increase. As a result, it accelerated the photocatalytic degradation of MB dye easier. This denotes the capability of Rh doping method that it enhances the photocatalyst ability for organic molecule degradation.

In chapter 4, we studied the properties of Ti3NS:Rh<sub>x</sub> as a photocatalyst for H<sub>2</sub> production. Photocatalytic H<sub>2</sub> production was observed under UV and visible light by triethylamine (TBA) as an electron donor in the system. The comparison study was done by using cocatalyst loading to compare with TBA. We used photodeposition by loading Rh<sub>2</sub>O<sub>3</sub> on the surface of Ti3NS with the ratio similar to Rh-doped amount. The result of H<sub>2</sub> production evidently exhibited the differences between Rh doping, and Rh<sub>2</sub>O<sub>3</sub> cocatalyst loading.<sup>1-5</sup> In the case of Rh doping, the amount of H<sub>2</sub> production was correlated with the amount of Rh doping, the ratio of Rh<sup>3+</sup> to Rh<sup>4+</sup>, and redox reaction of Rh<sup>3+</sup> and Rh<sup>4+</sup> under UV light irradiation.

When combining the result from previous chapter with this chapter, we found that the hole pool of Rh<sup>4+</sup> enhances the photocatalyst ability for photodegradation reaction, and Rh<sup>3+</sup> as an electron pool. This makes the photo reduction of water molecule occurs

efficiently. However, the ratio of  $\text{Rh}^{3+}$  to  $\text{Rh}^{4+}$  and redox reaction of  $\text{Rh}^{3+}$  and  $\text{Rh}^{4+}$  are also significant. Alternatively, visible light irradiated on  $\text{Ti3NS:Rh}_x$  revealed that  $\text{Ti3NS:Rh}_x$  did not respond to visible light as a photocatalyst for  $\text{H}_2$  production. Although, the energy band gap of  $\text{Ti3NS}$  was narrowed when  $\text{Rh}$  was doped but it did not activate  $\text{Ti3NS:Rh}_x$  under visible light.

In chapter 5, we used the concept of dye-sensitizer by combining  $\text{Ti3NS:Rh}_x$  with photosensitizer dye. This is to make the  $\text{Ti3NS:Rh}_x$  to respond to the visible light. Dyes which were used in the experiments are inorganic dye, and organic dye. Inorganic dye used in the research is  $\text{Ir}(\text{ppy})_2(\text{bpy})^+$ , and organic dye which is  $\text{TMPyP}$  porphyrin.  $\text{Ti3NS:Rh}_x$  could adsorb dye both dyes but the adsorption phenomenon was different.  $\text{Ir}(\text{ppy})_2(\text{bpy})^+$  was adsorbed at the surface of  $\text{Ti3NS:Rh}_x$  while  $\text{TMPyP}$  was intercalated into the interspacing of  $\text{Ti3NS:Rh}_x$  which restacked  $\text{Ti3NS:Rh}_x$  by  $\text{TMPyP}$  as a counter ion. Even though,  $\text{Ir}(\text{ppy})_2(\text{bpy})^+$  and  $\text{TMPyP}$  have LUMO level higher than  $\text{Ti3NS:Rh}_x$  but the measurement of  $\text{H}_2$  production under visible light irradiation ( $\lambda \geq 350 \text{ nm}$ ) showed that only  $\text{Ir}(\text{ppy})_2(\text{bpy})^+$  dye-sensitized  $\text{Ti3NS:Rh}_x$  can produce  $\text{H}_2$  by TEA as electron donor. From this, it states that electron injection between  $\text{TMPyP}$  and  $\text{Ti3NS:Rh}_x$  occurred inefficiently. The result of photoluminescence revealed that  $\text{TMPyP}$ -dye-sensitized  $\text{Ti3NS:Rh}_x$  showed fluorescence properties when it was irradiated at  $\lambda \geq 400 \text{ nm}$ . Electron injection did not progress proficiently despite  $\text{TMPyP}$  intercalated in the interlayer spacing of  $\text{Ti3NS:Rh}_x$ . In this chapter, we showed that the possibility on developing dye-sensitized photocatalyst under visible light irradiation without the help of cocatalyst. This is another step for improving photocatalyst material.

In chapter 6, we found that Ti<sub>3</sub>NS:Rh<sub>x</sub> can incompetently adsorb organic dye from chapter 3. Hence, Ti<sub>3</sub>NS:Rh<sub>x</sub> is still impractical for using as a photocatalyst for organic molecule degradation. Additionally, the synthesis of Rh-doped titanate compound by solid-state reaction that we presented in chapter 3 is hard to control the Rh doped amount. In this chapter, we tried using polymerized complex for synthesizing Rh doped potassium titanate and exfoliated to titanate nanosheet (Ti<sub>4</sub>NS:Rh<sub>x</sub>). The result denotes that we can control the Rh-doped amount using polymerized complex. The adsorption of MB dye presented that Ti<sub>4</sub>NS:Rh<sub>x</sub> showed adsorption capacity for MB dye relatively higher than Ti<sub>3</sub>NS:Rh<sub>x</sub>. This can be elucidated by the fact that the particle size of Ti<sub>4</sub>NS:Rh<sub>x</sub> is smaller than Ti<sub>3</sub>NS:Rh<sub>x</sub>, therefore, the adsorption surface area is higher than Ti<sub>3</sub>NS:Rh<sub>x</sub>. When adsorption increased causing the photocatalytic activity for MB degradation of Ti<sub>4</sub>NS:Rh<sub>x</sub> higher than Ti<sub>3</sub>NS:Rh<sub>x</sub>. Likewise, Rh doping also exhibited similar result as Ti<sub>3</sub>NS:Rh<sub>x</sub> where Rh enhances the photocatalyst ability of Ti<sub>4</sub>NS. The differences between them is that Rh<sup>4+</sup> was not found in Ti<sub>4</sub>NS:Rh<sub>x</sub> from the measurement of adsorption spectra of Ti<sub>4</sub>NS:Rh<sub>x</sub>. When Rh doped amount increased, the photocatalytic oxidation occurred progressively. This signifies that Rh is formerly Rh<sup>3+</sup> and is an electron pool in which it turns to Rh<sup>4+</sup> as a hole pool.<sup>6-10</sup> This improves the MB dye oxidize ability.

## **7.2 Conclusion**

This research focuses on the development and improvement of titanate nanosheet as a photocatalyst and sunlight energy exchange in the chemical reaction i.e. degradation of organic compound or H<sub>2</sub> production. In this research, we focus solely on the metal doping. According to previous research, they showed that metal doping such as Rh doping enhances the photocatalyst properties without using cocatalyst or aid in the

visible light adsorption. Our research used metal doping with titanate nanosheet in the hope that it will improve the photocatalyst properties along with increasing photoadsorption range of titanate nanosheet to visible light region. In spite of Rh doping, the enhancement of titanate nanosheet helps the photoadsorption due to the presence of  $\text{Rh}^{3+}$  and  $\text{Rh}^{4+}$ , however, Rh doped titanate nanosheets still did not active under visible light. Nonetheless, Rh doping effect on photocatalytic activity of titanate nanosheet is fascinating. Even though, it may not active under visible light but only under UV light irradiation. Rh doping plays a key role in dominating  $\text{Rh}^{3+}$  which helps in photo-reduction, while  $\text{Rh}^{4+}$  aids in photo-oxidation. Consequently,  $\text{Rh}^{3+}$  acts as electron pool along with  $\text{Rh}^{4+}$  as a hole pool, and we found the possible mechanism of  $\text{Rh}^{3+}$  and  $\text{Rh}^{4+}$  outcome on the improvement of photocatalytic activity of titanate nanosheets.

Besides the use of Rh doping, combining of titanate nanosheet with photosensitizer was used with the hope of titanate nanosheet can be active under visible light. Moreover, the combination of Rh doping with dye-sensitizer found to be a new promising development of photocatalyst material with high efficiency, and visible light respond.

## References

1. Kawasaki, S., Akagi, K., Nakatsuji, K., Yamamoto, S., Matsuda, I., Harada, Y., Yoshinobu, H., Komori, F., Takahashi, R., Lippmaa, M., Sakai, C., Niwa, H., Oshima, M., Iwashina, K., and Kudo, A. (2012). Elucidation of Rh-Induced In-Gap States of Rh:SrTiO<sub>3</sub> Visible-Light-Driven Photocatalyst by Soft X-ray Spectroscopy and First-Principles Calculations. *J. Phys. Chem. C*, 116(46), 24445-24448.
2. Yoshida, H., Shimura, K. (2012). XAFS Study of Rhodium Cocatalyst

Loaded on K<sub>2</sub>Ti<sub>6</sub>O<sub>13</sub> Photocatalyst. *Photon Factory Activity Report 2011*, 29, 40.

3. Shimura, K., Kawai, H., Yoshida, T., & Yoshida, H. (2012). Bifunctional Rhodium Cocatalysts for Photocatalytic Steam Reforming of Methane over Alkaline Titanate. *ACS Catal.*, 2(10), 2126-2134.
4. Kuncewicz, J., & Ohtani, B. (2015). Titania photocatalysis through two-photon band-gap excitation with built-in rhodium redox mediator. *Chem. Commun.*, 51(2), 298-301.
5. Maeda, K. (2014). Rhodium-Doped Barium Titanate Perovskite as a Stable p-Type Semiconductor Photocatalyst for Hydrogen Evolution under Visible Light. *ACS Appl. Mater. Interfaces*, 6(3), 2167-2173.
6. Okunaka, S., Tokudome, H., & Abe, R. (2015). Facile water-based preparation of Rh-doped SrTiO<sub>3</sub> nanoparticles for efficient photocatalytic H<sub>2</sub> evolution under visible light irradiation. *J. Mater. Chem. A*, 3(28), 14794-14800.
7. Yin, S., & Yu, F. T. (2000). *Photorefractive optics: materials, properties, and applications*. San Diego, CA: Academic.
8. Schneider, J., Bahnemann, D., Ye, J., Puma, G. L., & Dionysiou, D. D. (2016). *Photocatalysis: fundamentals and perspectives*. Cambridge: Royal Society of Chemistry.
9. Oropeza, F., & Egdell, R. (2011). Control of valence states in Rh-doped TiO<sub>2</sub> by Sb co-doping: A study by high resolution X-ray photoemission spectroscopy. *Chem. Phys. Lett.*, 515(4-6), 249-253.
10. Kučera, M., Kuneš, J., & Gerber, R. (1999). Magneto-optical effects of Rh<sup>3+</sup> and Rh<sup>4+</sup> doped yttrium iron garnet. *J. Appl. Phys.*, 85(8), 5986-5988.

## ACKNOWLEDGMENTS

I would like to express my deep gratitude to my supervisor, Associate Professor Ryo Sasai, who gave me a great support during the course of doing my PhD studies. His insight, constructive advices and encouragement have invaluablely helped me overcome a number of hurdles throughout the PhD project. I am grateful for all I have received during these years of my research journey. My sincere appreciation goes to my co-supervisor, Assistant professor Takuya Fujimura, for his patience, determined and continued kind support. His guidance and constructive ideas have given me a better understanding the research work and thus completing the thesis. I am thankful to all those who kindly supported me for the technical analysis. My special thanks go to Professor Usami Hisanao at Shinshu university for photoelectrochemical measurement, Professor Wataru Norimatsu at Nagoya university for Scanning Probe Microscope (SPM) measurement, Dr. Yusuke Date at Yonago National College of Technology for Scanning Electron Microscope (SEM) measurement, and Professor Toshio Sato, faculty of life and environmental science for ICP measurement.

I would like to express my deepest gratitude toward MEXT (Ministry of Education, Culture, Sports, Science and Technology) for giving me a scholarship to support me through my studies year from Master degree to Doctoral degree. I would not be able to complete this journey without MEXT support. I promise to contribute what I have gained to the society

Finally, I would like to express my greatest appreciation to my beloved parents and my sister for their unconditional love, care, inspiration and support. Moreover, I would like to thank my girlfriend, Sunisa Meanchaipiboon for her continual support during my studies.



Wasusate SOONTORNCHAIYAKUL